ON THE GASIFICATION OF WET BIOMASS IN SUPERCRITICAL WATER

Over de vergassing van natte biomassa in superkritiek water

J.A.M. Withag

On the gasification of wet biomass in supercritical water: over de vergassing van natte biomassa in superkritiek water.
Withag, J.A.M.

PhD thesis, University of Twente, Enschede, The Netherlands, April 2013

ISBN 978-94-6191-724-9

This research was funded by the EOS-LT program of Senter Novem (EOS-LT 05020).
Printed by: Ipskamp Drukkers

ON THE GASIFICATION OF WET BIOMASS IN SUPERCRITICAL WATER

OVER DE VERGASSING VAN NATTE BIOMASSA IN SUPERKRITIEK WATER

PROEFSCHRIFT

ter verkrijging van
de graad van doctor aan de Universiteit Twente,
op gezag van de rector magnificus,
prof.dr. H. Brinksma
volgens besluit van het College voor Promoties
in het openbaar te verdedigen
op donderdag 23 mei 2013 om 12.45 uur

door

Johannes Antonius Maria Withag
geboren op 14 september 1981
te Hengelo

Dit proefschrift is goedgekeurd door de promotor
Prof. dr. ir. G. Brem

De promotiecommissie:

Voorzitter:	
Prof. dr. F. Eising	Universiteit Twente
Promotor:	
Prof. dr. ir. G. Brem	Universiteit Twente
Leden:	
Prof. dr. ir. T. H. van der Meer	Universiteit Twente
Prof. dr. ir. H. W. M. Hoeijmakers	Universiteit Twente
Dr. ir. D.W.F. Brilman	Universiteit Twente
Prof. dr. ir. L. Lefferts	Universiteit Twente
Prof. dr. L. P. H. de Goey	Technische Universiteit Eindhoven
Prof. dr. ir. B. J. Boersma	Technische Universiteit Delft

Voor
Tonnie, Gerda
en Hester

Voorwoord

Dit proefschrift is tot stand gekomen met de ondersteuning van een groot aantal mensen. Allereerst wil ik Gerrit, Eddy en Theo bedanken voor het bieden van de mogelijkheid om deze promotie aan de Universiteit Twente te mogen doen. Het is voor mij een zeer uitdagende en leerzame periode geweest. De vele discussies die ik met elk van jullie drie heb mogen voeren beschouw ik als een grote meerwaarde. Ook van de niet werk gerelateerde discussies over BWO - de Tukkers, FC Twente, wielrennen, reizen en politiek heb ik zeer genoten.

Ik wil graag Ilori, Jules, Nick, Beinte en Joost bedanken voor de belangrijke bijdrage die zij aan dit onderzoek hebben geleverd. Daarnaast Robert en Henk Jan, jullie waren een onmisbare factor in het lab, bedankt voor de goede hulp bij het ontwerpen en opbouwen van de experimentele opstellingen. Sally mag ik hierbij niet vergeten, bedankt voor het bijspringen bij zaken die niet direct met het onderzoek te maken hadden.

Mijn mede-promovendi wil ik bedanken voor de vele interessante discussies die we hebben gehad over het werk, sport en cultuur. In het bijzonder Marc, Uros, Timo, Maarten, Lixian en Artur wil ik bedanken voor hun humor en bereidheid om te allen tijde bij te springen wanneer ik met werkgerelateerde vragen zat. Het werk was natuurlijk ook leuk door alle medewerkers, AIO's en studenten van de ThW-groep. De koffie- en lunchpauzes, het voetballen, de borrels en het koken bij Theo in de tuin.

Ik wil al mijn vrienden en familie bedanken voor de steun en aanmoediging! In het bijzonder wil ik mijn ouders bedanken voor alle gezelligheid, goede hulp en hun onvoorwaardelijke vertrouwen. Pa en Ma, bedankt voor alles wat jullie voor mij gedaan hebben.

De belangrijkste die ik wil bedanken is Hester! Het laatste anderhalf jaar heb je me veel tijd gegund om de promotie tijdens weekenden en avonden af te ronden, dit was niet altijd gemakkelijk. De afgelopen jaren ben je een rots in de branding geweest. Bedankt voor al je vertrouwen, steun en liefde!

Summary

Supercritical water gasification (SCWG) is a challenging thermo-chemical conversion route for wet biomass and waste streams into hydrogen and/or methane. At temperatures and pressures above the critical point the physical properties of water differ strongly from liquid water or steam. Because of the physical properties of supercritical water, SCWG is considered to be a promising technology for the thermo chemical conversion of wet biomass. Anticipated applications for supercritical gasification of wet biomass are for example:

- The on-site production of a fuel gas in industry, vehicles, buildings.
- The production of pure hydrogen for the process industry.
- The production of a hydrogen or methane rich gas from manure or sewage sludge.
- The production of syngas, mainly consisting of CO and H_2, at high pressure.

Although the results on a laboratory scale show that SCWG is a very promising technique, the process is still in an early stage of development. A lot of work remains to be done to get a full understanding of the complex process and to bridge the gap between small-scale testing in laboratories to demonstration on full-scale. For this purpose, adequate design rules for SCWG need to be developed.

The primary objective of this thesis is to study the mechanisms and key parameters of SCWG and to develop design rules for adequate reactor and process design. The following approach is chosen to meet these objectives:

1. Investigation of the influence of key process parameters on the thermal efficiency of supercritical gasification of wet biomass.
2. The development of heat transfer models for water at supercritical pressures.
3. The development of a new high throughput batch reactor for conversion rate measurements of supercritical gasification of wet biomass.
4. The evaluation and experimental validation of sorption enhanced supercritical gasification of wet biomass.

1. Investigation of the influence of key process parameters on the thermal efficiency of supercritical gasification of wet biomass.

A system model for the process of gasification of biomass model compounds in supercritical water is developed. The thermodynamic model is generated in ASPEN 12.1 under the assumption of chemical equilibrium and using model compounds to represent the organics in the wet biomass. The first part of the research focuses on predicting the influence of process parameters on the thermal efficiency of the overall process. The parameters under investigation are the heat exchanger effectiveness, the possibility of tailoring the product gases and in-situ CO_2 capturing using water.

The results obtained with the developed thermodynamic model show that the composition of the product gases can be tailored to a desired product gas composition by changing the process parameters such as the reactor temperature, pressure or the concentration of organic material in the feed. Furthermore it is shown that the overall thermal efficiency is very sensitive for the heat exchanger effectiveness.This is mainly caused by the high heat capacity of water and the high water content of the feed stream. The possibility of in-situ CO_2 capturing produced during supercritical gasification is also investigated using the thermodynamic model. A large part of the CO_2 present in the product gases can be captured using the water present in the system. The process water can be recycled to absorb more CO_2, but this comes at the expense of the thermal efficiency. A feed with 5 wt% of methanol shows a decrease of 20% in thermal efficiency when the CO_2 capture efficiency is improved with 20%, this is due to an increase in dissolved H_2 and CH_4. The CO_2 can be captured at 100 bar so no extra compression step is necessary before transportation.

2. The development of heat transfer models for water at supercritical pressures.

For the design of efficient heat exchangers more knowledge is required on heat transfer in supercritical water. Therefore numerical models have been developed. A 1D plug flow model has been developed in order to predict the bulk-fluid temperature in a tubular flow. Nusselt correlations for the heat transfer coefficient are required to close the set of equations. The experimental validation for three different cases shows that the 1D-model is able to accurately predict the bulk temperature based on the Nusselt correlation that was valid for that specific case. However, the different Nusselt correlations are limited to the specific conditions on which they were based. These limitations lead to the conclusion that it is important to consider boiling effects that occur when a critical heat flux is reached. The right choice of the Nusselt correlation for the simulated case is crucial for the quality of the results of the 1D-model.

To get a better insight the heat transfer is also investigated using a two-dimensional modeling approach. The two-dimensional model is based on low-Reynolds k-ϵ turbulence model, and the IAPWS-IF97 formulation to describe the properties of water at different process conditions. The accuracy of the model is validated using an experimental setup at supercritical pressures. The comparison of the measured and calculated temperature shows a good agreement. The 2D-model results have also been compared with the results from the 1D-model using several Nusselt correlations from literature. Each individual Nusselt correlation shows an incapability to predict the heat transfer coefficient accurately over the entire pipe length. Therefore it can be concluded that 1D-models should not be used to simulate the heat transfer to supercritical water in long or complex pipe configurations. For both the 1D-model and the 2D-model the effect of the methanol decomposition reaction on the heat transfer has been investigated. Due to the plug flow assumption of the 1D-model, the model is not capable of capturing the high temperature gradients in radial direction, which leads to an underestimation of the conversion rate. The 2D-model is more suitable for predicting chemically reacting flow. From the 2D-model results it can be seen that the heat transfer to a reacting flow is larger than heat transfer to a non-reacting flow.

3. The development of a new high throughput batch reactor for conversion rate measurements of supercritical gasification of wet biomass.

A new high throughput batch reactor is developed for conversion rate measurements of supercritical water gasification of wet biomass. In the standard autoclave reactor a mixture of biomass and water is injected and heated up to supercritical conditions. During the heating-up sub-critical reactions may take place resulting in other conversion rates and product gases. In the present study an autoclave reactor is extended with a high pressure injection system which allows the injection of both liquid and solid particles into the reactor under supercritical conditions. The high throughput batch reactor is tested with the gasification of methanol and algae in supercritical water. For both feedstocks the hydrogen yield and the conversion degree increased with a higher process temperature. Due to the newly developed injection system the time of the heating up trajectory is significantly decreased from 10 minutes to 20 seconds and this results in a higher conversion rate.

4. The evaluation and experimental validation of sorption enhanced supercritical gasification of wet biomass.

Finally the possibility of in-situ CO_2-capture in the gasification process is investigated. The so called ’sorption enhanced supercritical water gasification’ (SE-SCWG) of wet biomass is evaluated and compared to conventional supercritical reforming. CaO, NaOH and hydrotalcite are tested as possible sorbents for sorption enhanced supercritical gasification. The evaluation is performed by both equilibrium calculations and experimental research.

Thermodynamic calculations were done to model the process of sorption enhanced gasification in supercritical water. A large increase in H_2 production can be seen for both CaO or NaOH as CO_2-acceptor. The calculations show that the WGS reaction is strongly shifted in the direction of H_2 in the product gases for the case of SE-SCWG of methanol. Sorption enhanced gasification of both methanol and micro-algae in supercritical water are experimentally tested in the high-throughput batch reactor. Hydrotalcite and NaOH were tested with methanol as a biomass model compound and micro-algae as a real biomass source. Especially the results for NaOH were promising with a high production of H_2 and a large reduction in both conversion time and CO_2 in the dry product gases. Also for the algae case a large reduction in CO_2 production is shown in the experimental results. Even though algae are a difficult compound to convert completely into dry product gases, the conversion was more than doubled when NaOH was added to the process.

Samenvatting

Vergassing van natte biomassa in superkritiek water is een uitdagende conversie route om biomassa om te zetten in waterstof en/of methaan. Op temperaturen en drukken boven het kritieke punt verschillen de fysische eigenschappen van water sterk van die van vloeibaar water of stoom. Met dank aan de fysische eigenschappen van water, wordt vergassing in superkritiek water gezien als een veelbelovende technologie voor de thermo-chemische omzetting van natte biomassa. Verwachte applicaties voor de superkritieke vergassing van natte biomassa zijn bijvoorbeeld:

- Het op locatie produceren van brandstof voor industrie, voertuigen of gebouwen.
- Productie van pure waterstof voor de proces-industrie.
- Het omzetten van mest of zuiveringsslib in een gas, rijk aan waterstof of methaan.
- Productie van synthese gas op hoge druk.

Vergassing in superkritiek water is nog in de beginfase van de ontwikkeling, er moet veel werk worden verzet om het complexe proces volledig te doorgronden. Daarnaast is er een groot gat tussen de huidige experimentele opstellingen op laboratorium schaal en een toekomstige demonstratie van het proces op industriële schaal. Met dit in het achterhoofd is het belangrijk dat er goede ontwerpregels worden ontwikkeld voor het proces van vergassing in superkritiek water.

Het voornaamste doel van dit proefschrift is het onderzoeken van de mechanismen en sleutelparameters voor het proces van superkritieke vergassing van natte biomassa. Hieruit volgen ontwerp regels voor een gedegen reactor en proces ontwerp, de volgende aanpak is gekozen om dit doel te bereiken:

- Een studie naar de invloed van procesparameters op de thermische vergassing van natte biomassa in superkritiek water.
- De ontwikkeling van warmte overdracht modellen voor water op superkritieke druk.
- De ontwikkeling van een nieuwe batch reactor waarmee de conversie snelheid van superkritiek vergassen van natte biomassa gemeten kan worden.
- De evaluatie en experimentele validatie van sorptie ondersteunde vergassing van natte biomassa.

1. Een studie naar de invloed van procesparameters op de thermische vergassing van natte biomassa in superkritiek water.
De vergassing van natte biomassa in superkritiek water is gemodelleerd door middel van een thermodynamisch systeemmodel gegenereerd in ASPEN 12.1. De modellering is gedaan onder de aanname van chemisch evenwicht en met behulp van modelstoffen voor het organisch materiaal in de biomassa. Dit model is allereerst ingezet om de invloed van de procesparameters op de thermische efficiëntie van het proces te bepalen.

De resultaten die zijn verkregen met het thermodynamische model laten zien dat de gascompositie in een gewenste richting kan worden gestuurd door procesparameters aan te passen. Wanneer de proces temperatuur, procesdruk of het gewichtspercentage van het organisch materiaal in de voedingsstroom worden aangepast heeft dit een groot effect op de samenstelling van de productgassen. Daarnaast is aangetoond dat de thermische efficiëntie van het gehele proces sterk afhankelijk is van de effectiviteit van de warmtewisselaar. Dit wordt voornamelijk veroorzaakt door de hoge warmtecapaciteit van water en de grote hoeveelheid water in de voedingsstroom.

De mogelijkheid om in-situ CO_2 af te vangen tijdens de superkritieke vergassing is onderzocht aan de hand van het thermodynamisch model. Wanneer gebruik wordt gemaakt van het al aanwezige water in het proces kan een groot deel van het CO_2 in de productgassen worden afgevangen. Wanneer het proceswater wordt gerecycled bestaat de mogelijkheid om een nog grotere hoeveelheid CO_2 af te vangen, deze strategie gaat wel ten koste van de thermische efficiëntie.

2. De ontwikkeling van warmte overdracht modellen voor water op superkritieke druk.
Voor de ontwikkeling van een efficiënte warmtewisselaar is het zaak dat er meer kennis beschikbaar komt op het gebied van warmte overdracht in superkritiek water. Binnen dit onderzoek zijn hiervoor twee numerieke modellen ontwikkeld. Allereerst een 1D plug flow model waarmee de bulk stroom temperatuur kan worden bepaald van water op superkritieke druk in een buisstroming. De set van vergelijkingen voor dit numerieke stromings-probleem wordt gesloten door middel van een warmteoverdrachtscoëfficiënt, de warmteoverdrachtscoëfficiënt wordt bepaald door middel van een Nusselt correlatie. De juiste keuze van de Nusselt correlatie is bepalend voor de kwaliteit van het 1D model.

De warmte overdracht is tevens bestudeerd aan de hand van een 2D model, waarbij de turbulentie wordt gemodelleerd doormiddel van het low-Reynolds k-ϵ model en de fysische eigenschappen van water doormiddel van de IAPWS-IF97 formulering. Dit model is gevalideerd met behulp van een experimentele opstelling, deze validatie liet een goede overeenkomst zien tussen het model en het experiment. De resultaten van het 2D model zijn vergeleken met de resultaten van het 1D model waarbij diverse Nusselt correlaties uit de literatuur zijn gebruikt. Elk van de gebruikte Nusselt correlaties was niet in staat om de warmteoverdrachtscoëfficiënt over de volledige buislengte goed te bepalen. Hieruit kan geconcludeerd worden dat het 1D model niet moet worden gebruikt voor de simulatie van warmteoverdracht voor superkritiek water voor lange buizen of complexe configuraties.

Voor zowel het 1D als voor het 2D model is gekeken naar het effect van de methanol decompositie reactie op de warmteoverdracht. Het 1D model onderschat de conversiesnelheid van de methanol, dit wordt veroorzaakt door de aanname van plug flow waarbij het model niet in staat is om temperatuurgradiënten in radiale richting te voorspellen. Het 2D model is beter in staat om chemische reacties te simuleren, uit de resultaten blijkt dat de warmteoverdracht naar de reagerende stroming groter is dan de warmteoverdracht naar de niet-reagerende stroming.

3. De ontwikkeling van een nieuwe batch reactor waarmee de conversie snelheid van superkritiek vergassen van natte biomassa gemeten kan worden.
Voor het bepalen van de conversiesnelheid van de vergassing van natte biomassa in superkritiek water is een nieuwe batch reactor ontwikkeld. In een standaard batch reactor wordt voorafgaand aan het proces een mengsel van biomassa en water geïnjecteerd waarna het vervolgens wordt opgewarmd tot superkritieke condities. Tijdens het opwarmtraject vinden er allerlei subkritieke reacties plaats die resulteren in afwijkende conversiesnelheden en productgassen. In de huidige studie is de batch reactor uitgebreid met een injectiesysteem op hoge druk, met behulp van dit injectiesysteem kan de natte biomassa in de reactor worden geïnjecteerd wanneer deze al op superkritieke condities is. De nieuw ontwikkelde reactor is getest voor de superkritieke vergassing van zowel methanol als algen. In beide gevallen was de proces temperatuur van grote invloed op zowel de waterstof opbrengst als de mate van conversie. Door middel van het ontwikkelde injectiesysteem is de tijd van het opwarm traject drastisch afgenomen, dit heeft geresulteerd in een hogere mate van conversie.

4. De evaluatie en experimentele validatie van sorptie ondersteunde vergassing van natte biomassa in superkritiek water.
Tot slot is de mogelijkheid van het in-situ afvangen van CO_2 onderzocht binnen het proces van vergassing van natte biomassa in superkritiek water. Het zogenaamde 'sorptie ondersteund vergassen van natte biomassa' is onderzocht en vergeleken met het conventionele vergassen van natte biomassa in superkritiek water. CaO, NaOH en hydrotalciet zijn geselecteerd als sorbents voor deze evaluatie en worden onderzocht door middel van chemisch evenwicht berekeningen en experimenten.

De resultaten van de chemisch evenwicht berekeningen laten zien dat er een grote toename is in H_2-produktie wanneer CaO of NaOH als CO_2-sorbent worden gebruikt. De berekeningen laten zien dat de water gas shift reactie sterk in de richting van H_2 wordt gestuurd wanneer sorbents aan het proces worden toegevoegd. Hydrotalciet en NaOH zijn experimenteel getest voor het sorptie ondersteund superkritiek vergassen van zowel methanol als algen. Met name de experimenten waarbij NaOH werd gebruikt als sorbent resulteerden in een hoge productie van H_2 en een grote afname in zowel conversietijd als in hoeveelheid CO_2 in het productiegas.

Table of Contents

1

Introduction

1.1 Background

Towards an entirely new national energy system based on renewable sources, the Dutch government currently aims at 16% renewable energy in 2020. The goal for 2050 is a Dutch energy system completely based on renewable energy sources. Biomass will play an important role in this transition. Worldwide biomass is one of the most plentiful and well-utilized sources of renewable energy. Biomass can be used for the production of electricity, heat, fuels and chemicals and is considered to be CO_2 neutral.

Wet biomass is a renewable resource that currently is difficult to use in an efficient way. The high water content in feedstocks such as food waste, sewage sludge, manure, rice husk or algae hinders the use of thermo-chemical conversion processes such as pyrolysis or gasification. The required energy to evaporate the water before converting the organics into useful products makes these

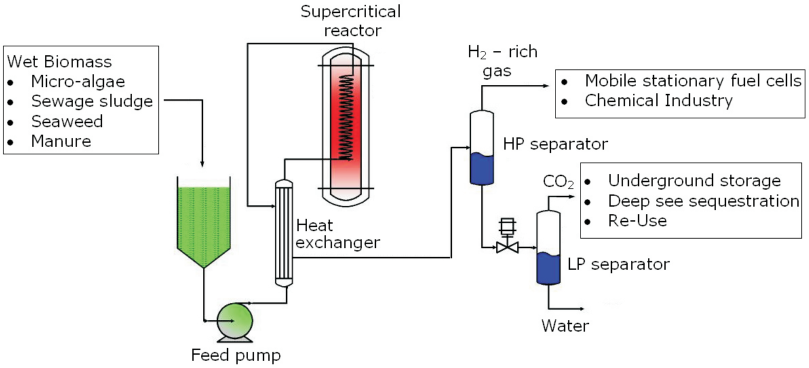

Figure 1.1: *Scheme of the full chain of biomass gasification in supercritical water.*

processes economically not feasible. Gasification in supercritical water could be an interesting alternative for these wet biomass streams. Above the critical pressure (221 bar) and a temperature larger than 374°C, the biomass slurry changes from the liquid phase directly to the supercritical phase. An advantage of using supercritical conditions is that organic material is completely miscible with supercritical water, resulting in a homogeneous reaction phase. Because of the homogeneous reaction phase the mass transfer barriers between phases are eliminated and therefore the reaction rates are increased [60, 106, 124].

The properties of supercritical water, such as density, viscosity, dielectric constant, and hydrogen bonding are different from liquid water or steam. In the process of supercritical gasification of biomass, the supercritical water is multifunctional: it is a solvent, a catalyst and a reactant [59]. Applying gasification in supercritical water, the expensive conventional drying step for wet biomass is not required. Additional advantages of the process can be found in a compact reactor design because of the high density of supercritical water; Easy separation of CO_2 from the product gases due to the higher solubility of CO_2 in water at high pressure when compared to the other product gases; The possibility to control the selectivity of the process by changing the process conditions; And the opportunity to use the heat from the reactor effluent to heat up wet biomass before it enters the reactor. The produced gas is available at high pressures and this is interesting for downstream applications such as: gas turbines and refineries.

Anticipated applications for supercritical gasification of biomass are for example:

- The on-site production of a fuel gas in industry, vehicles, buildings.
- The production of pure hydrogen for the process industry.
- The production of a hydrogen or methane-rich gas from manure or sewage sludge.
- The production of syngas, mainly consisting of CO and H_2, at high pressure.

Fig. 1.1 shows a schematic of a continuous SCWG reactor. The set up consists of a feed storage for the wet biomass, a pump for pumping the slurry at supercritical pressure, the SCWG reactor and a heat exchanger to heat the reactants and cool the hot product gases. After the heat exchanger the hot product gases are cooled further using a cooling system and then the two phase product stream is separated using a high pressure and low pressure separator.

At present two SCWG pilot plants are being operated in the world. With a throughput of 100 l/h the VERENA test facility at the Forschungszentrum Karlsruhe (FzK) is the largest pilot plant existing so far [24]. The plant was built to demonstrate supercritical gasification of wet residues from wine production, and it was designed for a process temperature of 700°C and a maximum pressure of 350 bar. Various types of biomass have been successfully converted to gas in the VERENA plant [60]. The second pilot plant is a process development unit (PDU) built by BTG, with a maximum throughput of 30 l/h [94, 112]. The PDU was first tested with components like ethanol and glycerol. Later trials are intended for more difficult feedstock types like starch, and eventually, real biomass [80]. Both pilot plants were built to demonstrate SCWG, but they were not optimized in terms of energy consumption.

SCWG is a technology in the early stages of its development. In this thesis emphasis is given on developing design rules for an adequate reactor and process design for supercritical gasification of wet biomass.

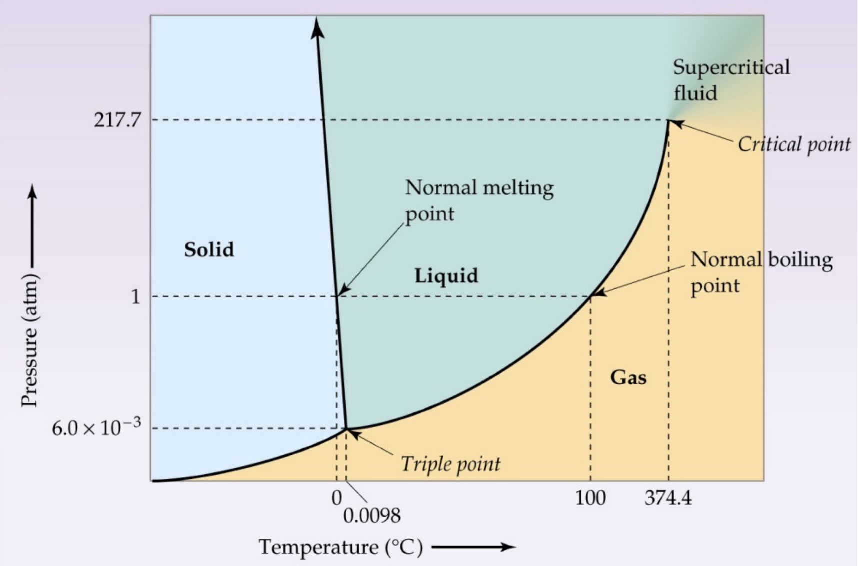

Figure 1.2: *Pressure-Temperature diagram for water.*

1.2 Supercritical water

A fluid is called supercritical when both the pressure and the temperature are above their critical value. This point is indicated by the so called critical point (C), as can be seen in the phase diagram of water (Fig. 1.2) the critical point is located at the position where the vapor line ends.

The line that connects the triple point with the critical point indicates the boiling point for the intermediate pressures. The boiling point increases with pressure until the critical pressure is reached. At the critical point (374°C, 221 bar) and beyond, the distinction between the two phases is disappeared so that the fluid is in a single, supercritical phase.

Although the transition from liquid water to supercritical water is strictly speaking not a phase change, strong property variations are observed within a very limited temperature range. The gradients are largest near the critical point, where the transition still resembles that of sub-critical water, and become lower at higher pressures. Fig. 1.3 shows the density, isobaric heat capacity, conductivity and viscosity of water as a function of temperature at different pressures. The isobars plotted in the figure show the variation of the several properties of water at constant pressure, where the solid line indicates the variation at supercritical pressure.

In general, the properties of supercritical water are in between those of liquid water and steam. An increase of fluid temperature is accompanied by a continuous decline in density, conductivity and viscosity (Figs. 1.3(a), 1.3(b) and 1.3(d)). The location of the peak in the graph of the specific heat capacity at constant pressure is a good indicator for the critical temperature, this is clearly

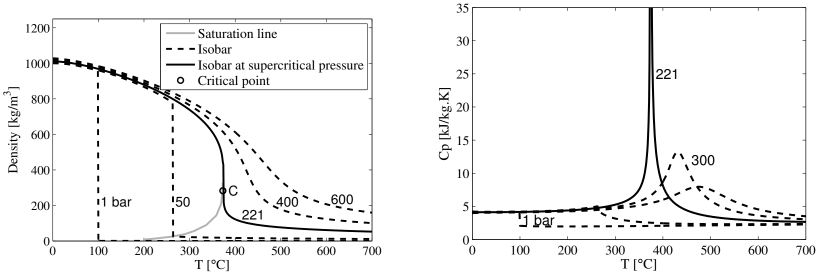

(a) Density.

(b) Specific heat capacity at constant pressure.

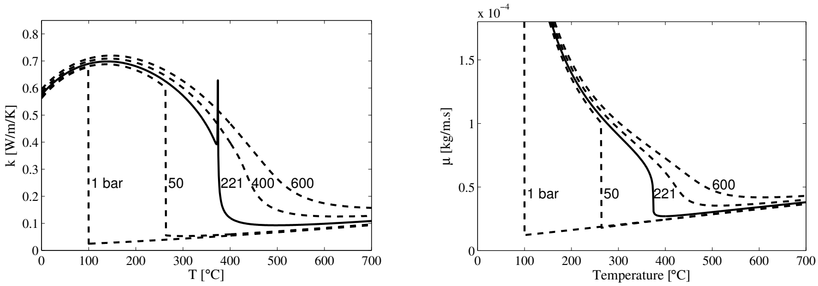

(c) Conductivity.

(d) Viscosity.

Figure 1.3: *Properties of supercritical water.*

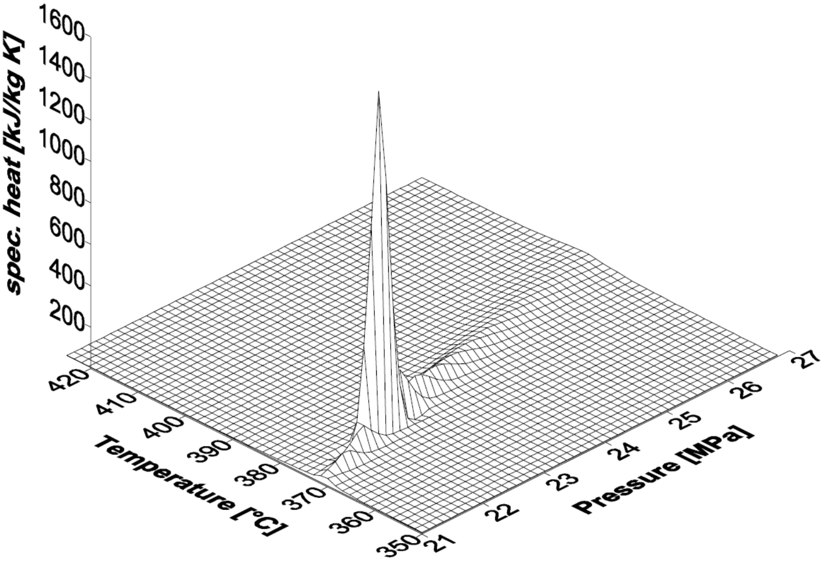

Figure 1.4: *Specific heat of water.*

shown in Figs. 1.3(b) and 1.4. The peak in C_p is highest at the critical pressure, but is also present at higher pressures where it indicates the pseudo-critical point.

A drastic reduction in density causes a significant decrease in the static dielectric constant, resulting in an improved solubility of organic substances and permanent gases like H_2, CH_4 and CO_2. The behavior of supercritical water as a solvent for intermediates and product gases enables single-phase gasification and possibly opens the door to an effective thermo-chemical conversion route for wet biomass.

1.3 Supercritical water gasification

Supercritical water gasification (SCWG) is an interesting route to convert wet biomass into hydrogen or methane. When compared to other hydrogen production methods, SCWG is the most promising technology for the thermo-chemical conversion of wet biomass as no pre-drying step is required.

In SCWG, supercritical water has the following roles:

1. An excellent solvent for intermediates and product gases, resulting in single phase reactions. Single phase reactions eliminate mass transfer barriers between phases and therefore increases reaction rates [60, 106, 124]. In parallel with the increasing reaction rate the solvation capabilities of supercritical water result in a suppression of tar and coke formation.

2. A reactant which promotes the water gas shift reaction and the hydrolysis reaction [64, 106].

3. A source of hydrogen, due to weak hydrogen bonding of water at high temperatures and pressures. Supercritical water has a high hydrogen-releasing ability [106].

From these points it can be concluded that supercritical water fulfills every possible role it is able to fulfill: solvent, catalyst, and reactant [59]. Where each separate role results in different advantages of the SCWG process.

Additional advantages of the process can be found in a compact reactor design because of the high density of supercritical water. Easy separation of CO_2 from the product gases due to the higher solubility of CO_2 in water at high pressure when compared to the other product gases. The possibility to control the selectivity of the process by changing the process conditions. And the opportunity to use the heat from the reactor effluent to heat up wet biomass before it enters the reactor.

SCWG is a challenging solution for the thermo-chemical conversion of wet biomass. Even though the process is under development since the late seventies several hurdles have to be taken in order to demonstrate the technology in practice. One important challenge is the design of the heat exchanger, as the heat exchange plays a very important role in the energy efficiency of the complete process. Another challenge for commercial applications is the corrosive behavior of water as a reaction medium. Corrosion of the reactor material was observed during several experiments done for SCWG. Taking into account corrosion, combined with the required high temperatures and pressures it is clear that the choice of materials for the reactor is of key interest. Furthermore due to the non-polar solvent behavior of water at supercritical conditions the solubility of salts is greatly reduced, this could therefore lead to wall deposits and plugging of the reactor by salts. For a succesful implementation of the SCWG process it is necessary that these challenges are dealt with.

1.4 Scope and objectives of the study

Results on a laboratory scale show that SCWG is a very promising process, but still in an early stage of development. A lot of work remains to be done to understand the process completely and to bridge the gap between small-scale testing in laboratories to demonstration in practice. In order to do this effectively, adequate design rules for SCWG need to be developed.

The primary objective of this thesis is to gain deeper insights in the mechanisms of the heat transfer, conversion rate, product gas composition and thermal efficiency of SCWG in order to improve the reactor and system design. In order to achieve this objective the following questions need to be answered:

1. Can gasification of wet biomass in supercritical water be designed as a thermally efficient process?
2. What is the influence of the large property variations of water, in the transition from sub- to supercritical water, on the heat transfer in the SCWG process?
3. Is it possible to gasify wet biomass such as algae in supercritical water?
4. Does the SCWG process allow for in-situ capturing of CO_2 during the process?

1.5 Thesis outline

The following approach is chosen to answer the questions posed in the previous section:

- Investigation of the influence of key process parameters on the thermal efficiency of supercritical gasification of wet biomass.
- The development of heat transfer models for water at supercritical pressures.
- The development of a new high throughput batch reactor for conversion rate measurements of supercritical gasification of wet biomass.
- The evaluation and experimental validation of sorption enhanced supercritical gasification of wet biomass.

Chapter 2 presents a system model for the process of gasification of biomass model compounds in supercritical water. The chapter focuses on predicting the influence of several process parameters on the thermal efficiency of the overall process. Three important parameters under investigation are the heat exchanger effectiveness, the possibility of tailoring the product gases and insitu CO_2 capturing using water present in the wet biomass.

Heat transfer in water at supercritical pressures has been investigated numerically using a one-dimensional modeling approach in Chapter 3. A 1D plug flow model has been developed to predict the bulk-fluid temperature in a tubular flow.

Chapter 4 numerically investigates heat transfer using a two-dimensional modeling approach. The two-dimensional is based on the low-Reynolds k-ϵ turbulence model, and the IAPWS-IF97 formulation to describe the properties of water at different process conditions. The accuracy of the model is validated using an experimental setup at supercritical pressures.

A description of the development and first experimental work on a new high throughput batch reactor concept for conversion rate and product gas composition of supercritical water gasification of wet biomass is given in Chapter 5. In a standard autoclave reactor a mixture of biomass and water is injected and heated up to supercritical conditions. During the heating-up sub-critical reactions may take place resulting in other conversion rates and product gases. In the present study an autoclave reactor is extended with a high pressure injection system which allows the injection of both liquid and solid particles into the reactor under supercritical conditions. The high throughput batch reactor is tested with the gasification of methanol and algae in supercritical water.

Finally Chapter 6 investigates the possibility of in-situ CO_2-capture in the gasification process. The so called 'sorption enhanced supercritical water gasification' (SE-SCWG) of wet biomass is evaluated and compared to conventional supercritical reforming. CaO, NaOH and hydrotalcite are tested as possible sorbents for sorption enhanced supercritical gasification. The evaluation is performed by both equilibrium calculations and experimental research.

2

System model for gasification of wet biomass in supercritical water

This chapter presents a system model for the process of gasification of biomass model compounds in supercritical water. Supercritical water gasification of wet biomass (water content of 70wt% or more) has as a main advantage that conversion may take place without the costly drying step. The thermodynamic model is generated in ASPEN 12.1 under the assumption of chemical equilibrium and using model compounds to represent the organics in the wet biomass. The research focuses on predicting the influence of several parameters on the thermal efficiency of the process. One of the important parameters under investigation is the heat exchanger effectiveness. The possibility of tailoring the product gases and in-situ CO_2 *capturing using water are also modeled and described.*

The work in this chapter has been published in revised form as:
J.A.M. Withag, J.R. Smeets, E.A. Bramer and G. Brem, System model for gasification of biomass model compounds in supercritical water - A thermodynamic analysis, The Journal of Supercritical Fluids, Elsevier **61** *(2012).*[127]

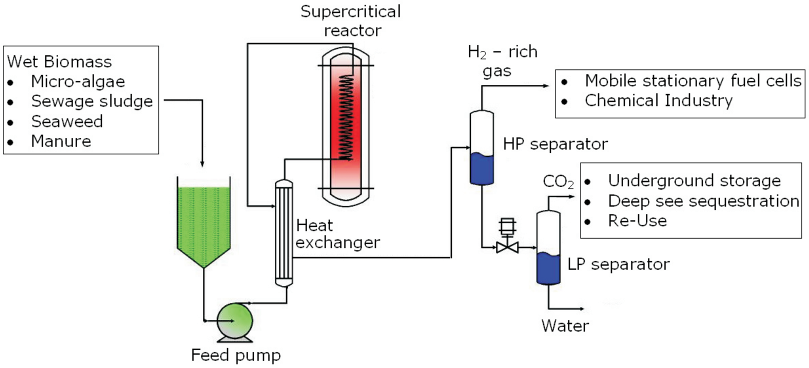

Figure 2.1: *Scheme of the full chain of biomass gasification in supercritical water.*

2.1 Introduction

Biomass is one of the most plentiful and well-utilized sources of renewable energy in the world. Biomass can be used for the production of electricity and heat, but also for the production of liquid or gaseous fuels. However, without pre-treatment, biomass with a moisture content of more than 70% is not suitable for combustion, gasification or pyrolysis processes and therefore other conversion processes have to be developed. With the advantage of avoiding the costly drying process, gasification in supercritical water is a promising technique to convert wet biomass into a hydrogen- or methane-rich gas at high pressure that can be used for a wide range of applications.

Supercritical water gasification (SCWG) is a challenging thermo-chemical conversion route for wet biomass and waste streams into a medium calorific gas. At temperatures and pressures above the critical point of water (Fig. 1.2) there is no distinction between the gas and liquid phase. The physical properties of supercritical water strongly differ from liquid water or steam. There is a large decrease in dielectric constant, viscosity, thermal conductivity and in the vicinity of the critical point a large peak in the specific heat capacity can be detected [59, 80]. Anticipated applications for supercritical gasification of wet biomass are for example:

- The on-site production of hydrogen in industry, vehicles, buildings.

- The production of renewable hydrogen as a clean fossil fuel.
- The production of a methane-rich gas.
- The production of syngas, mainly consisting of CO and H_2.

SCWG is a technology in the early stages of technical development. A better understanding of the fundamental phenomena is essential for an adequate SCWG reactor- and process design. In order to maximize conversion and to optimize the gas yield and composition, research on the key parameters influencing the overall process efficiency is of great importance.

Fig. 2.1 shows a schematic of a continuous SCWG reactor. The set up consists of a feed storage for the wet biomass, a pump for pumping the slurry at supercritical pressure, the SCWG reactor and a heat exchanger to heat the reactants and cool the hot product gases. After the heat exchanger the hot product gases are cooled further using a cooling system and then the two phase product stream is separated using a high pressure and low pressure separator.

The economic feasibility of gasification in supercritical water strongly depends on the thermal efficiency of the process: is it possible to convert a highly diluted organic compound into a useful product gas in an energetically efficient manner? Biomass is a complicated and inhomogeneous substance and therefore difficult to model in a flowsheet. In the present study the wet biomass is modeled by different biomass model compounds, i.e. methanol, glucose and cellulose. The second assumption is that chemical equilibrium is reached under the investigated process conditions. This is a common approach when the reaction mechanism and the kinetics are not yet well understood. Of course this will result in an overprediction of reaction products that are rate limited. In this study the equilibrium approximation is followed and this will give a good indication of the thermal efficiency of process. The process flowsheet software Aspen Plus 12.1 is used to model the different steps needed in the overall chain.

The first thermodynamic model for supercritical water gasification was developed by Antal [7] to model the reforming of cellulose in an excess of water. Since then several other groups have conducted research in thermodynamic modeling of SCWG systems [75, 109, 134, 138]. Although these models did not exactly provide the same results the following trends can be recognized:

- The CO content of the produced gas is very low.

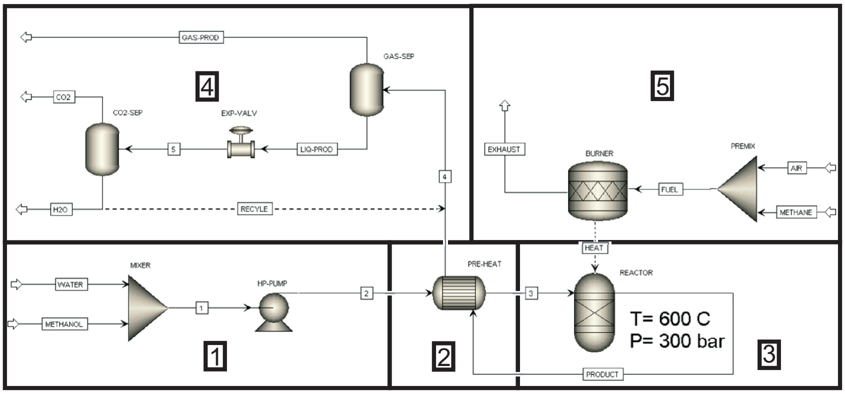

Figure 2.2: *System model with different sub models.*

- The hydrogen yield increases with temperature. Especially above 600°C hydrogen is the dominating product. The methane yield increases at lower temperatures (< 600°C).
- With an increasing biomass concentration in the feed, the hydrogen yield decreases while the methane yield increases.
- Pressure does not have a significant influence on the overall process.

The goal of the present study is to gain more insight in the effect of the process parameters on the thermal efficiency of the process. In Section 2.2 the process flowsheet which is used to predict the overall efficiency for the supercritical water gasification process is described. Section 2.3 explains the theory and the assumptions of the chemical equilibrium reactor. In Section 2.4.1 a description of the dependency of the product gases on the process conditions such as temperature, pressure, and weight percentage of organics is given. Section 2.4.2 shows the results of a sensitivity analysis for the thermal efficiency when the heat exchanger effectiveness is changed. In Section 2.4.3 an optimalisation towards the production of a methane rich gas is investigated. Finally, an evaluation on the possibility of capturing carbon dioxide using the water available in the feed as a solvent is given in Section 2.5.

2.2 Process flowsheet of the system model

In Fig. 2.2, a flowsheet of the SCWG system is shown. Here a mixture of water and methanol as a biomass model compound is used to mimic wet biomass. It is also possible to use other model compounds like glucose or cellulose. The flowsheet is divided in the five most important sections:

1. The low temperature mixing and pressurization of the feed.
2. The heat exchange between the product gas and the feedstream.
3. The supercritical gasification reactor.
4. The separation of the product gas, and water recycle for CO_2 capture.
5. The heat supply for the endothermic conversion reactions in the reactor.

The mixing step is implemented to mix the biomass with a certain amount of water. After the mixing step the feed stream is pressurized (>> 221 bar) using a high pressure pump. A heat exchanger is used to preheat the mixture to supercritical temperature (>> 374°C), the heat of the product gases of the supercritical reactor is used to preheat the feed mixture. The supercritical mixture enters the reactor and is further heated to reactor conditions (600°C). The extra required heat in the reactor is delivered by a methane burner.

The heat from the product gases is used to preheat the mixture. Then the product gases are further cooled below the critical point in a separate heat exchanger to separate the permanent gases from the liquid water with dissolved CO_2 in a high pressure phase separator. The high pressure liquid is further expanded to atmospheric pressure to release the stored CO_2 in the low pressure separator. The product gas can be stored or upgraded while it is at high pressure or used directly in a gas turbine. The important parts of the flowsheet will be described in more detail in the next sections. The following section describes the selection of a suitable property method for the equilibrium calculation at supercritical conditions.

2.3 Chemical equilibrium reactor for SCWG

Although several experimental investigations have been conducted on supercritical water gasification of biomass model compounds and real biomass [12, 38, 64, 76, 100, 137, 138], no mechanistic reaction path with kinetical constants has been accepted at the moment for the reactions taking place with supercritical gasification. For this reason and because the goal is to study the thermal efficiency of the system, use has been made of chemical equilibrium modeling to calculate the composition of the product gas.

2.3.1 Gibbs energy of reaction

When a multicomponent mixture reaches chemical equilibrium the Gibbs free energy is at a minimum. The minimum in Gibbs energy is at the same point where the Gibbs energy of reaction ($\Delta_r G$) reaches zero. The Gibbs energy of reaction is defined as the change in Gibbs energy with respect to the extent of the reaction.

$$\Delta_r G = \frac{\partial G}{\partial \xi} \tag{2.1}$$

where ξ is the extent of the reaction. The Gibbs energy of reaction not being zero indicates that there must be a point of lower Gibbs energy (G). In this case the multicomponent mixture will move to a state where the Gibbs energy is at a minimum. The change in Gibbs energy for a reaction is the difference between the sums of the chemical potentials of the reactants and the products.

$$\Delta_r G = \sum_{j=1}^{n} \mu_j n_j \tag{2.2}$$

In Eq. 2.2 n_j and μ_j are the molar number and the chemical potential of component j. The equation for conservation of elements can be written as:

$$\sum_{j=1}^{n} a_{ij} n_j - b_i^0 = 0, \quad i = 1, \ldots, l \tag{2.3}$$

where a_{ij} is the molar number of element i in compound j, and b_i^0 is the molar number of element i in the initial reactant. The Gibbs free energy is at a minimum when a multicomponent system reaches chemical equilibrium. Minimizing the Gibbs free energy of a system, with fixed T and P, is a simple constrained optimization problem. The constraints can be removed using the method of Langrange multipliers. Eq. 2.4 is used to determine the chemical potential of component μ_i.

$$\mu_i(T,P)=\mu_i^0(T)+RT\ln f_i \tag{2.4}$$

where $\mu_i^0(T)$ is the chemical potential of component i in standard state, R is the ideal gas constant, and f_i is the partial fugacity of component i. The partial fugacity can be calculated using an equation of state, the equation of state used in this research is discussed in the following paragraph.

2.3.2 Choice of property method

A property method is used to calculate the thermodynamic and transport properties of a chemical system. The partial pressures of the different components in a system are strongly influenced by the property method used in the calculation, therefore the choice of a property method is of great importance.

There are two main methods of calculating thermodynamic and transport properties: the activity coefficient method for the fluid phase and the equation-of-state (EOS) method for all phases. The main advantage of using an EOS method is the wide range of temperatures and pressures for which it can be used. EOS methods also give reasonable results for both sub-critical and supercritical conditions. The advantage of the activity coefficient method is the capability to predict the behavior of strong polar components such as water-alcohol mixtures. A drawback for the activity coefficient models is that they can be used up to a maximum pressure of approximately 10 bar. This limits the possible application of these methods for the present study on SCWG.

The important steps in the present process are the gasification in the reactor and the high pressure product separation. In case of the high pressure product separation the pressure is too high for the use of activity coefficient methods. Therefore, the main focus of this section will be on determining the most suitable EOS method. An overview of the available property methods in combination with mixing rules and α functions is given in Table 2.1.

Fig. 2.3 shows the hydrogen produced at increasing reactor temperature when using several EOS methods. All temperature predictions using different property methods show the same trend. As shown in the literature [59, 76, 109, 134] the equilibrium shifts to the production of hydrogen at higher temperatures since the hydrogen forming reactions are endothermic. But the amount of hydrogen differs as much as 12% at 600°C, as can be seen in the figure.

The property method Ideal is based on the ideal gas law. The main advantage of this property method is its simplicity. On the other hand the Ideal EOS has difficulties when calculating vapor-liquid equilibrium. This can be seen clearly in Fig. 2.3 when looking at temperatures in the vicinity of the critical temperature (374°C). This property method predicts the highest hydrogen production since it does not consider interaction between the molecules or the volume of the molecules.

The Peng-Robinson (PR) [92] and the Redlich-Kwong (RK) [97] property methods are both extensions of the ideal gas law. Although both property methods account for the molecule volume and the interaction between molecules they are not capable of accurately predicting the fluid behavior at the high pressures

Table 2.1: *Available property methods and alpha functions in Aspen Plus [1].*

Property method	EOS	Mixing rule or α-function
IDEAL	Ideal gas law	-
PENG-ROB	PR	-
PR-BM	PR	BM
PRMHV2	PR	MHV2
PRWS	PR	WS
RK-Soave	SRK	-
RKS-BM	SRK	BM
RKSMHV2	SRK	MHV2
RKSWS	SRK	WS
PSRK	SRK	Gmehling

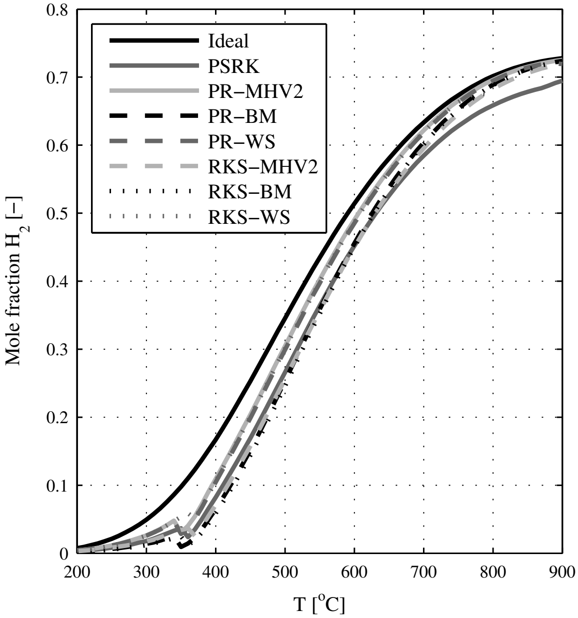

Figure 2.3: *Comparison of equilibrium H_2 temperature dependence for different property methods, for 10 wt% MeOH, 300 bar.*

present in this system. Both property methods are most accurate for systems at low to moderate pressures for which vapor-phase non-ideality is low.

The thermodynamic properties of a pure substance can be calculated using an EOS, but how these properties relate to a mixture with possible interactions between different components requires the use of a mixing rule. The modified Huron-Vidal (MHV2) and the Wong-Sandler (WS) mixing rules increase the accuracy of predicting the thermodynamic properties for polar mixtures. Both mixing rules are tested during this investigation.

The interaction between molecules can effect the predicted equilibrium composition and partial pressures in a chemical system. Especially for mixtures with polar and non-polar molecules or with molecules of different sizes the ability to handle deviations from ideal behavior is significant. A lot of research is done on the improvement of the modeling of attractive forces between molecules, the most successful of these alpha functions are implemented in Aspen Plus. In this research Soave's addition to the RK EOS, the Boston-Mathias (BM), and the Twu and Twu generalized alpha functions [88] are evaluated for the supercritical gasification case. It was found that the different alpha functions are comparable and the results for the hydrogen production differ less than 2% for all alpha funtions at the temperatures considered for supercritical water gasification. Therefore, it is decided to only consider Soave's addition to the RK EOS and the BM alpha function for the present study (RKS-BM in Fig. 2.3).

In this study the temperatures of interest lie between the critical temperature of water (i.e. 373°C) and 650°C. At pressures above the critical pressure the temperature of 650°C is close to the maximum temperature from an engineering point of view, due to material limitations. Looking at the temperature range of interest, in Fig. 2.3, it can be seen that the Ideal equation of state has the largest difference in H_2 production when compared to the seven other property methods especially in the vicinity of the critical point. The property methods based on the Peng-Robinson and Soave Redlich-Kwong equations of state all give a prediction of the H_2 mole fraction within a bandwidth of 3.5%.

Any of these property methods is suitable for use in the supercritical region, here the Soave Redlich-Kwong property method with modified Huron-Vidal mixing rule (SRKMHV2) is chosen because this method is already used and tested with similar chemical systems at supercritical conditions [15, 31, 71, 75]. More detailed information about property methods can be found in [111].

2.4 Results of the system model

In this paragraph the effect of the key process parameters (i.e. temperature, pressure, and the composition of the feed) on the composition of the product gas is discussed. The product gas composition is required for the calculation of the overall thermal efficiency of the process that will be discussed in Section 2.4.2. Section 2.4.3 gives an overview on what will happen when the scope of the SCWG process is changed from H_2 production to CH_4 production.

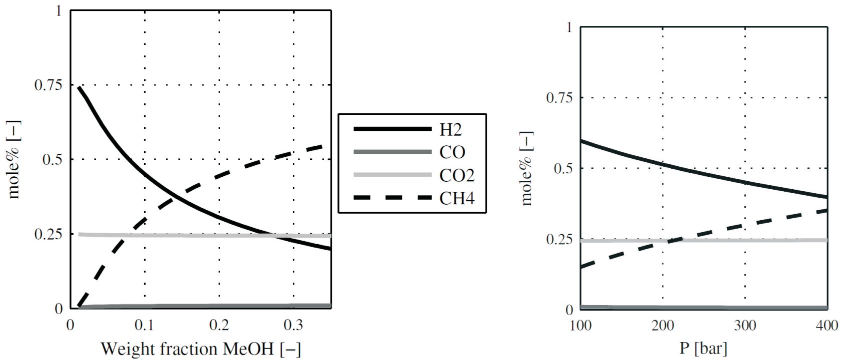

(a) Change of methanol concentration.

(b) Change of reactor pressure.

Figure 2.4: *Equilibrium product gas composition for different methanol concentrations and pressures, at 600° C and respectively 300 bar and 10 wt% of MeOH.*

2.4.1 Product gas composition

In order to explain the effects of the process conditions on the product gas produced, a similar approach is used as in Kruse [59] for the glucose case. Complete conversions to H_2 and CH_4 are assumed to be the limiting states, for which the following stoichiometric equations apply. The endothermic formation of hydrogen where the amount of molecules double is given by:

$$CH_3OH + H_2O \rightarrow CO_2 + 3H_2. \tag{2.5}$$

The exothermic formation of methane with a 50% increase of the amount of molecules is given by:

$$4CH_3OH \rightarrow CO_2 + 2H_2O + 3CH_4. \tag{2.6}$$

Effect of feed composition

Looking at Eqs. 2.5 and 2.6, it can be seen that the forming of H_2 needs water while the formation of CH_4 produces water. Hence, a higher concentration of

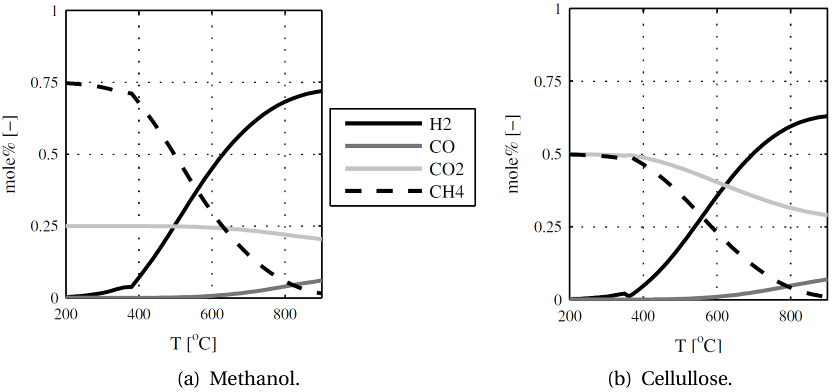

(a) Methanol.

(b) Cellullose.

Figure 2.5: *Equilibrium product gas composition for different reactor operating temperatures, at 300 bar and for both 10 wt% MeOH and 10 wt% cellullose.*

biomass, which means a lower concentration of water, favors the formation of CH_4. This is confirmed by the equilibrium calculation results as given in Fig. 2.4(a). The results show an increase in CH_4 yield and a reduction in H_2 yield when the methanol weight fraction in the reactant stream is increased.

Effect of reactor pressure

The effect of the reactor pressure on the equilibrium product composition is shown in Fig. 2.4(b). An increase in total pressure results in an increase of the several partial pressures of the components and the equilibrium shifts to the side with the smaller volume increase. An increase in pressure results in a decrease in the yield of H_2 and a decrease in pressure results in an increase in CH_4.

Effect of reactor temperature

The third important process parameter besides the methanol content of the feed stream and the reactor pressure is the operating temperature of the reactor. At higher temperatures endothermic reactions are favored while at lower temperatures the equilibrium shifts to exothermic reactions. For methanol this is clearly shown in Fig. 2.5(a) where at high temperatures the formation of H_2 is more dominant than the formation of CH_4.

Fig. 2.5(b) shows the result when cellulose is added to the supercritical reactor. It can be seen that the same trends are followed for the predicted product gas composition. Methanol has a hydrogen to carbon ratio of four while cellulose has hydrogen to carbon ratio of 10/6. This can also be seen in Fig. 2.5, where in the case of cellulose more CO_2 is formed per mole of cellulose compared to the methanol case. For cellulose this reduces the production of methane in the low temperature part of the plot and reduces the production of H_2 for the high temperature part of the plot compared to methanol.

2.4.2 Process efficiency

The thermal efficiency is a critical factor that determines the economic feasibility of gasification of the biomass model compounds in supercritical water. In this section the thermal efficiency of the process is studied while several operating parameters of the process are varied. The thermal efficiency of the process is defined as the energy present in the produced gases minus the energy of the methane required for combustion to heat the reactor, and the work done by the pump, divided by the energy present in the feedstream [77].

$$\eta_{\text{(th)}} = \frac{\dot{m}_{(H_2,prod)} * LHV_{H_2} + \dot{m}_{(CH_4,netto)} * LHV_{CH_4} - P}{\dot{m}_{(feed)} \quad * \quad LHV_{(feed)}}. \tag{2.7}$$

$$\dot{m}_{(CH_4,netto)} = [\dot{m}_{(CH_4,prod)} - \dot{m}_{(CH_4,comb)}]. \tag{2.8}$$

As can be seen in Eq. 2.7 the lower heating value (LHV) of the several species is multiplied with the massflow $\dot{m}$ of that specific species to calculate the energy present in the flow. For the data needed in the calculations use has been made of the extensive ASPEN 12.1 database [1]. The fuel for the burner can consist of the produced methane that is recycled back into the system or if necessary methane from an external source. The energy used by the pump (P) is also subtracted from the energy contained in the product gases while calculating the thermal efficiency.

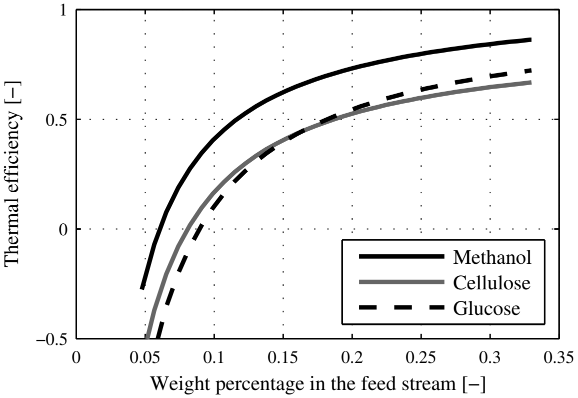

Figure 2.6: *Thermal efficiency at changing weight percentages for three model compounds of biomass. The calculations where done at a pressure of 300 bar, a temperature of 600° C, and a heat exchanger effectiveness of 75%.*

Weight percentage of the biomass model compound

The thermal efficiency of the gasification process depends strongly on the amount of biomass in the wet feed. The higher the biomass content (methanol, glucose or cellulose) in the feedstream, the higher the thermal efficiency. This is clearly shown in Fig. 2.6. The calculations presented in this paragraph where done at a pressure of 300 bar, a temperature of 600°C, and a heat exchanger effectiveness of 75%.

Fig. 2.6 shows that for a weight percentage of methanol lower than 6% the thermal efficiency is less than zero. This means that more methane is required for the combustor than available in the produced gases. For both cellulose and glucose the point of zero thermal efficiency lies at an higher weight percentage, because more CO_2 is being formed when both glucose and cellulose are being gasified. Compared to the methanol calculation for the cellulose and glucose case per kJ of energy put into the system in the form of organics less energy in the form of CH_4 and H_2 is formed. It also costs more energy to keep the supercritical reactor at a temperature of 600°C in the case of glucose and cellulose, as it costs more energy to crack the bigger molecules.

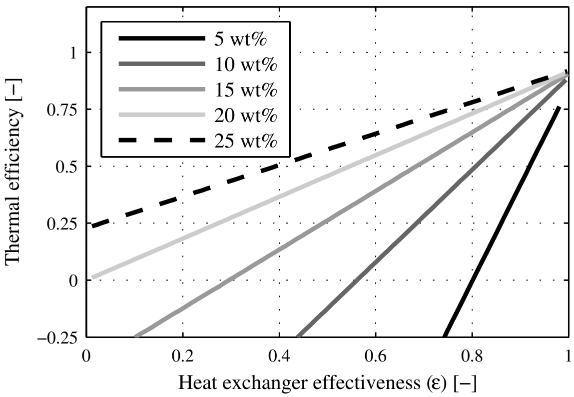

Figure 2.7: *Effect of the heat exchanger effectiveness (ϵ) on the thermal efficiency of the system for different methanol concentrations in the feed. The calculations where done at a pressure of 300 bar and a temperature of 600° C.*

The thermal efficiency rises rapidly with an increase of the methanol content, reaching to a maximum efficiency of 92.5% for 35 wt% methanol. For a thermal efficiency of 50% a feed with a minimum methanol weight percentage of 12% is required. For both glucose and cellulose this point lies around a weight percentage of 18%.

Heat exchanger effectiveness

The high water content of the feed stream combined with the high heat capacity of water results in a strong effect of the heat exchanger effectiveness on the overall thermal efficiency. The definition of the heat exchanger effectiveness is the ratio of the actual heat transferred by the heat exchanger and the maximum heat that could possibly be transferred from one stream to the other:

$$\epsilon = \frac{H_{(\text{cold, out})} - H_{(\text{cold, in})}}{H_{(\text{hot, in})} - H_{(\text{cold, in})}} \tag{2.9}$$

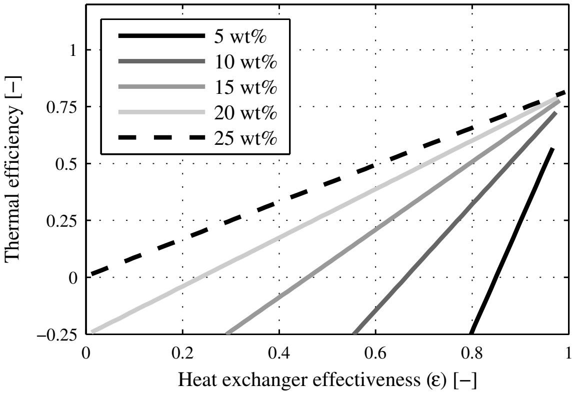

Figure 2.8: *Effect of the heat exchanger effectiveness (ϵ) on the thermal system efficiency for different cellulose concentrations. The calculations where done at a pressure of 300 bar and a temperature of 600° C*

The heat exchanger effectiveness has a large influence on the thermal efficiency of the overall system and especially when the feed stream has a low concentration of organics (see Fig. 2.7). For a methanol concentration of 5% or less a heat exchanger effectiveness of 80% is required for an adiabatic situation (i.e. no external heat source is required). In case of 5% of cellullose a heat exchanger effectiveness of 86% is required for adiabatic purposes, as can be seen in Fig. 2.8. In practice a heat exchanger of 80% is realistic in practice, a higher effectiveness is possible but this is not always justified economically.

In order to achieve an overall thermal efficiency of 70% and a heat exchanger effectiveness of at least 80% the weight percentage of methanol and cellulose in the feed should be at least 20% and 25%, respectively.

2.4.3 Process optimization for methane production

Changing the scope of the process from a hydrogen producing reactor to a methane producing reactor could have an important impact on the thermal efficiency of the gasification of biomass model compounds in supercritical wa-

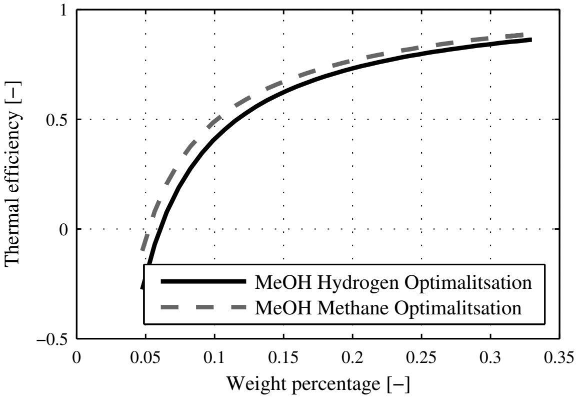

Figure 2.9: *Thermal efficiency at changing weight percentages for both the hydrogen optimized case and the methane optimized case. The hydrogen calculations where done at a pressure of 300 bar, a temperature of 600° C, and a heat exchanger effectiveness of 75%. The methane calculations where done at a pressure of 400 bar, a temperature of 400° C, and a heat exchanger effectiveness of 75%.*

ter. The two main advantages of producing methane in a supercritical gasifier are that at a relatively low temperature of 400°C methane is the favored product gas and methane is formed by an exothermic reaction. However, at these low temperatures the carbon efficiency for SCWG is very low [37, 40]. Using a catalyst can increase the carbon efficiency to the range of 94-98% at 400°C [94].

The model is adjusted to test the case of supercritical gasification of methanol at conditions where methane production is favored. This was done at a pressure of 400 bar and a temperature of 400°C, the burner is now fed with hydrogen instead of methane to keep the reactor at process temperature.

The results are shown in Fig. 2.9, it can be seen that the case optimized for methane production has a higher thermal efficiency on the complete range of methanol weight percentages in the reactant feed. The thermal efficiency for a methane system is 48.5% (40% for a H_2-system) for a weight percentage of 10%. For a weight percentage of 30% the thermal efficiencies for methane and hydrogen are 87% and 84%, respectively.

From these calculations it can be concluded that for an improvement in thermal efficiency it is better to optimize the process for methane. However, it is noted that for a methane process catalysts are required in a severe atmosphere of supercritical water.

2.4.4 Discussion

As explained in Section 2.3 chemical equilibrium has been assumed for the reactor. In order to show the validity of these calculations the numerical results are compared with experimental data presented in the work of Boukis et al. [23]. The experimental results were achieved in an inconel 625 reactor at a residence time of 45 [s] [23]. Taylor et al. [110] proposes three important reactions for the supercritical water reforming of methanol.

$$CH_3OH \Rightarrow CO + 2H_2 \tag{2.10}$$

$$CO + H_2O \Leftrightarrow CO_2 + H_2 \tag{2.11}$$

$$CO + 3H_2 \Rightarrow CH_4 + H_2O \tag{2.12}$$

First methanol decomposition into hydrogen and carbon monoxide, secondly carbon dioxide and methane are formed via the water gas shift reaction and finally the methanation reaction. Taylor et al. [110] indicates that inconel 625 works as catalysator of the water gas shift reactor (Eq. 2.11), it also suppresses the methanation reaction (Eq. 2.12). It is known that the methanation reaction is a very slow step in the process of supercritical methanol reforming [109]. Therefore, the reactor material in combination with a residence time of 45 [s] [23] causes the experimental results to form almost no methane. If we choose to neglect methane production in the numerical equilibrium model we see in Fig. 2.10 that the model fits the data of Boukis et al. [23] quite well. Hence, within an inconel reactor the assumption of restricted chemical equilibrium seems to be realistic. However, for other reactor materials the slow methanation reaction could play a significant role. So the preferred product gas is very much dependent on the material choice of the reactor. If we compare

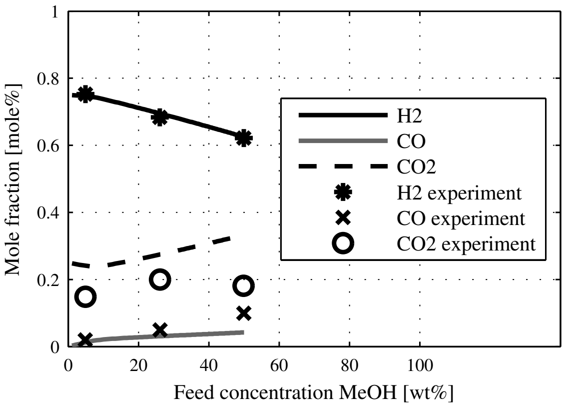

Figure 2.10: *Supercritical water reforming of methanol: comparison of experimental data [23]. Results for different methanol feed concentrations, at 280 bar and 600°C.*

some of the work done on supercritical gasification of glucose we can see that a stainless steel reactor [46] gives a completely different product gas composition when compared to an inconel 625 [138], Hastelloy [68] or a quartz glass reactor [58]. This comparison is thoroughly described in the work of Kersten et al. [58].

As mentioned in Section 2.1 methanol, cellulose and glucose are used as biomass model compounds. Biomass itself is a complicated mixture of organic and inorganic components. Therefore, a real biomass is very difficult to incorporate in a flowsheet, with the help of model compounds that have the same functional groups as contained in biomass the effect of process relevant parameters on the thermal efficiency can be studied. Methanol is a compound easy to use both in experiment and in numerical model but it is clear that it is far from a real biomass. Both cellulose and glucose are incorporated in this research to make a first step to simulate a real biomass. Glucose serves as a model compound which mimics the reaction chemistry of the many carbohydrates that (together with lignine) compose biomass [138]. Using a real biomass in the supercritical reformer major differences in the product gases compared to the present results can be expected. These differences are mainly determined by the presence of alkali salts which have a catalytic effect on the different reactions [123] and the presence of lignin causing a decrease in gas production [59, 136]. However, in this analysis the main focus is on the thermal efficiency of the system and the gas composition has only a limited influence on this efficiency.

The thermal efficiency, especially for lower methanol concentrations, is mainly determined by the performance of the heat exchanger. Another way to improve the thermal efficiency is using, e.g. the heat of the combustion gases that heat the reactor. This heat could be used, e.g. for preheating the combustion air or for preheating the water present in the feedstream. It is expected that preheating the water present in the feedstream will have the largest effect on the thermal efficiency. This effect is therefore tested for a case of 10 wt% of methanol and a process temperature for the supercritical reformer of 600°C. If all the heat present in the combustion flue gases is available for preheating the water present in the feedstream an increase can be seen of 4.3% in the thermal efficiency. Use of the heat in the flue gases turns out to be a good opportunity for further improvement of the thermal efficiency but not as crucial as for example the heat exchanger effectiveness.

2.5 In-situ carbon dioxide capture

Gasification of biomass model compounds in supercritical water allows for a low cost CO_2 capturing technique. Due to the high pressure of the process CO_2 can be captured in-situ by dissolution and separation via the water phase. This is done without adding any solvent except for the water already present in the feedstream stream. The possibilities of separating CO_2 from the product gas are discussed in this section.

2.5.1 Carbon dioxide solubility

Henry's law is used to approximate the amount of gas dissolved in the fluid. The amount of dissolved gas is proportional to the partial pressure of that particular gas above the fluid:

$$c = k_H \cdot p. \tag{2.13}$$

where p is the partial pressure of the component, k_H is the temperature dependent Henry's constant for this gas and c is the matching concentration in the solvent. The temperature dependence of k_H [73] is given by Eq. 2.14:

$$k_H(T) = k_H^\circ \cdot exp\left(\frac{d(\ln k_H)}{d(1/T)}\left(\frac{1}{T} - \frac{1}{298.15\mathrm{K}}\right)\right) \tag{2.14}$$

The Henry's constant at atmospheric temperature is given by k_H° and T is the real temperature of the mixture. Eq. 2.14 shows that the solubility improves at lower temperature. Table 2.2 gives the used Henry's constants and temperature dependence constants [73].

The difference in temperature dependency of the Henry's constants for the different components result in a change in relative solubility for the components at different temperatures. At low temperatures CO_2 has the highest solubility, but it also has the highest decrease in solubility with rising temperature. The solubility of CO_2 in the water is normalized and is plotted in Fig. 2.11 together with the solubility of the other gasification products.

The goal is to maximize the CO_2 separation from the product gas, while keeping the hydrogen and methane in the vapor phase. This is done in the high pressure separator shown in Fig. 2.2. Fig. 2.11 shows that the most efficient separation occurs at low temperature. Fig. 2.12 shows that the amount of methanol in the feed stream has a negative influence on the efficiency of CO_2 separation, due to a lower amount of water in the stream and a higher CO_2 production. The initial partial pressure of CO_2 remains reasonably constant while the methanol content is increased. This results in an increase in the

Table 2.2: *Henry's constants for the produced gases and the resulting solubilities [73].*

	Henry's constant at 298.15 K: (k_H°) [mole/kg·bar]	Temperature constant: $\left(\frac{d(\ln k_H)}{d(1/T)}\right)$ [K]	Solubility: k_H (303.15 K) [mole/kg·bar]	Amount dissolved [mole/kg H_2O]
H_2	0.00078	500	0.000759	0.092
CO	0.00099	1300	0.000921	0.002
CO_2	0.035	2400	0.030648	2.246
CH_4	0.0014	1600	0.001281	0.132

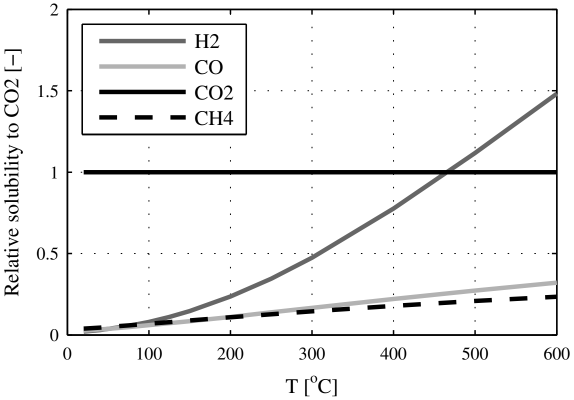

Figure 2.11: *Solubility of the different reaction products in water at different temperatures, relative to the solubility of CO_2.*

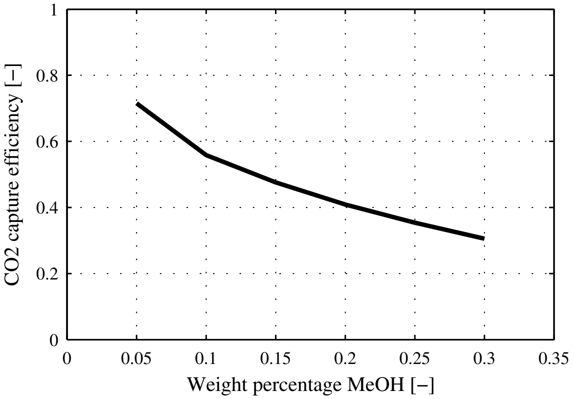

Figure 2.12: *Ideal CO_2 capture efficiency for different methanol concentrations.*

amount of CO_2 to be dissolved. The product separation occurs at a pressure of 300 bar and at this high pressure the assumptions made for the ideal gas law are no longer valid. The effective pressure of the CO_2 is lower, resulting in a lower amount of CO_2 dissolved in the water. This effect is implemented by

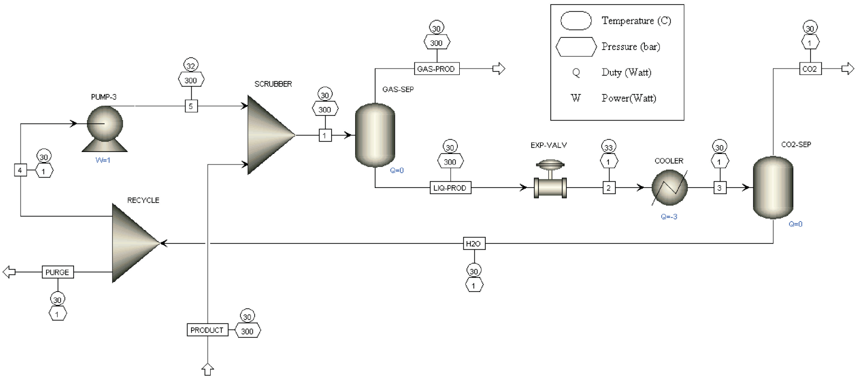

Figure 2.13: *Part of the process flowsheet with H_2O recycle stream to increase CO_2 capture efficiency.*

using the UNIFAC property method in combination with Redlich-Kwong EOS and Henry's Law as the calculation method for both the gas-liquid separator blocks. Light gases, i.e. H_2, CO, CO_2 and CH_4, are treated like Henry components. After this first separation the high pressure water with dissolved gases is expanded to atmospheric pressure, this is done in the low pressure separator releasing most of the dissolved gases.

2.5.2 Water recycling

The amount of CO_2 captured during the gasification process can be increased in three ways. First the solubility of CO_2 in water can be improved by lowering the temperature at which the first product separation takes place. A lower temperature gives a higher temperature constant (Eq. 2.15) resulting in a better gas solubility.

$$\text{Temperature constant} = \left(\frac{d(\ln k_H)}{d(1/T)} \right) \tag{2.15}$$

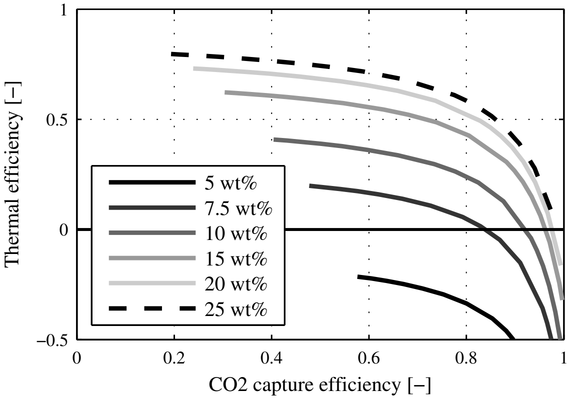

Figure 2.14: *Effect of increasing CO_2 capture efficiency by water recycling on the overall thermal efficiency of the conversion process, defined in Eq. 2.7. The lines are plotted for different weight percentages of methanol in the feedstream. The calculations where done at a pressure of 300 bar, a temperature of 600°C, and a heat exchanger effectiveness of 75%.*

This strategy has a drawback because cooling the product stream further would not be economically viable and the temperature of the water should not be reduced below the freezing point of water.

Secondly the amount of methanol in the feed stream can be kept very low, allowing for a high CO_2 capture efficiency. Section 2.4.2 already showed that this will result in a low thermal efficiency for the process.

The third option is to recycle a part of the water stream. The more water that is recycled, the more CO_2 can be dissolved. This option has the drawback that useful product gases such as H_2 and CH_4 are also dissolved in larger quantities. The process flowsheet is extended to implement this recycling of water and investigate the effect on the amount of CO_2 and other gases dissolved.

Fig. 2.13 shows the extended gas separation part of the flowsheet, the product stream coming is the cooled product gas coming from the reactor. When a water recycle is added the CO_2 capture shows a large increase, this comes at cost that there is also an increase in dissolved H_2 and CH_4. The extra pump needed to pressurize the recycled water to 300 bar is only a small parasitic loss, but the amounts of H_2 and CH_4 dissolved increase rapidly with a higher recycle ratio, this could result in a decrease of the thermal efficiency. Fig. 2.14 shows the consideration that has to be made between CO_2 capture and the thermal efficiency of the process. It shows that for high methanol concentrations recycling part of the process water can double the amount of CO_2 captured for only a small loss of thermal efficiency.

2.6 Conclusions

The gasification of biomass model compounds in supercritical water has the possibility to be a thermal efficient conversion process. The results obtained with this thermodynamic model show that the composition of the product gases can be tailored to a desired product composition by changing the process parameters such as the reactor temperature, pressure or the concentration of organic material in the feed. High temperature, low pressure and a low methanol concentration result in a product gas consisting mainly of hydrogen. A concentrated methanol feed at high pressure and low temperature is converted mainly to methane. The higher the concentration of organics in the stream the higher the thermal efficiency, until it stabilizes at concentrations above 40 wt%.

The efficiency of the heat exchanger has a strong effect on the thermal efficiency of the process. Mainly because of the high heat capacity of water and the high water content of the feed stream. In this research it is shown that a small increase in the heat exchanger effectiveness already has a strong impact on the overall thermal efficiency.

To achieve a thermal efficiency of 60% using a heat exchanger with a heat exchanger effectiveness of 75% a minimum organic content in the feestream is required of 14.5% or 25% for respectively methanol and cellulose.

When the scope of the process is changed to a methane producing gasifier an increase in the thermal efficiency is observed. From the comparison between the process optimized for hydrogen production and the process optimized for methane production it can be concluded that from an energy perspective it is better to optimize the process for methane. It must be taken into account that the process optimized for methane needs a catalysts for a good carbon efficiency.

The supercritical gasification process has the possibility of in-situ capturing CO_2 in the water phase. For a case of 10wt% of methanol in water at 600°C and 300 bar, 40% of the CO_2 present in the product gases can be captured using the water present in the system. The process water can be recycled to absorb more CO_2, but this comes at the expense of the thermal efficiency. A feed with 5 wt% of methanol shows a decrease of 20% in thermal efficiency when the CO_2 capture efficiency is improved with 20%, this is due to an increase in dissolved H_2 and CH_4.

3

Heat transfer characteristics of supercritical water

Heat transfer in water at supercritical conditions has been investigated numerically using a one-dimensional modeling approach. The set of equations is closed using Nusselt correlations found in literature and solved using an explicit Euler scheme to simulate heat transfer in a supercritical water flow. Results for three different cases show that the 1D-model is able to accurately predict the bulk temperature based on heat transfer rates provided by a suitable Nusselt correlation. However, there is also reason to assume that these correlations are very specific for the flow conditions, since boiling effects occurring at certain conditions can highly influence the heat transfer rate. As a consequence, the model may be unable to describe supercritical heat transfer over a broad range of configurations when only using one correlation.

The work in this chapter has been published in revised form as:
J.L.H.P. Sallevelt, J.A.M. Withag, E.A. Bramer, D.W.F. Brilman, G. Brem, One-dimensional model for heat transfer to a supercritical water flow in a tube, The Journal of Supercritical Fluids, Elsevier **68** *(2012).*[99]

3.1 Theory of reacting flows in supercritical water

This chapter is a general description of a chemically reacting flow of water at supercritical conditions. Section 3.1.1 deals with the equations that describe the flow field, heat transfer and chemical reactions. Next, Section 3.1.2 elaborates on the formulation that is used to calculate the relevant thermodynamic and tranport properties of water. Section 3.1.3 gives a more qualitative description of the characteristics of the flow on basis of information found in literature. The mathematics behind reacting flows and supercritical water presented in this chapter will form the basis for the 1D- and 2D-models that are used for simulating the continuous flow reactor.

3.1.1 Governing equations

The equations that describe reacting flows follow from the laws of conservation of mass, momentum, energy and species [21]. Starting with mass, the conservation principle is mathematically described by:

$$\frac{\partial \rho}{\partial t} + \vec{\nabla}\cdot(\rho\vec{u}) = 0, \tag{3.1}$$

where ρ is the mass density and $\vec{u} = (u, v, w)^T$ the velocity of the mixture. Conservation of momentum can be stated as the following vector equation, also referred to as the Navier-Stokes equations:

$$\frac{\partial(\rho\vec{u})}{\partial t} + \vec{\nabla}\cdot(\rho\vec{u}\vec{u}) = -\vec{\nabla}p - \vec{\nabla}\cdot\vec{\vec{\tau}} + \rho\vec{f}, \tag{3.2}$$

where $\vec{\vec{\tau}}$ is the viscous stress tensor and $\vec{f}$ is the volumetric force vector. For a Newtonian fluid like water, the viscous stresses are described by Newton's law of viscosity, which reads in general form:

$$\vec{\vec{\tau}} = -\mu\left(\vec{\nabla}\vec{u} + (\vec{\nabla}\vec{u})^T\right) + \left(\frac{2}{3}\mu - \kappa\right)\left(\vec{\nabla}\cdot\vec{u}\right)\vec{\vec{\delta}}, \tag{3.3}$$

where μ is the dynamic viscosity, κ is the dilatational viscosity and $\vec{\vec{\delta}}$ is the unity tensor.

Conservation of energy, in terms of total energy, is given by:

$$\frac{\partial\left(\rho E\right)}{\partial t}+\vec{\nabla}\cdot(\rho E\vec{u})=\rho\left(\vec{f}\cdot\vec{u}\right)-\vec{\nabla}\cdot(p\vec{u})-\vec{\nabla}\cdot(\vec{\vec{\tau}}\cdot\vec{u})+\dot{Q}+\vec{\nabla}\cdot\vec{q}. \tag{3.4}$$

Here $\dot{Q}$ is the volumetric heat source term and $\vec{q}$ is the heat flux vector. The heat flux vector is described by [57]:

$$\vec{q}=-k\vec{\nabla}T+\sum_{i=1}^{N}\vec{j}_i h_i-\sum_{i=1}^{N}\frac{RT}{M_i x_i}D_i^T\vec{d}_i \tag{3.5}$$

In this equation the first term on the right-hand side represents thermal conduction, where k is the thermal conductivity of the fluid. The second term describes heat transport by each of the diffusing species, where $\vec{j_i}$ is the diffusive mass flux vector and h_i is the specific enthalpy of species i. The third term stands for the diffusion-thermo effect, also known as the Dufour effect, containing the species molecular weights M_i, mole fractions x_i, thermal diffusion coefficients D_i^T and the diffusion driving forces $\vec{d}_i$. The vectors j_i and d_i are discussed here in more detail.

Conservation of the individual chemical species can be written in terms of mass fractions as follows:

$$\frac{\partial\left(\rho y_i\right)}{\partial t}+\nabla\cdot(\rho\vec{u}y_i)=\vec{\nabla}\cdot j_i+r_i. \tag{3.6}$$

where y_i is the mass fraction and r_i is the chemical source term of species i. By definition, the mass fractions of all species must sum to unity:

$$\sum_{i=1}^{N}Y_i=1. \tag{3.7}$$

The diffusive mass flux vector for a multicomponent mixture are described by the generalized Fick equations [57]:

$$\vec{j_i}=\rho\frac{M_i}{M^2}\sum_{j\neq 1}^{N}M_j D_{ij}\vec{d}_j-D_i^T\frac{1}{T}\vec{\nabla}T \tag{3.8}$$

Here the first term on the right-hand side accounts for concentration diffusion, pressure diffusion and forced diffusion. M is the mean molecular weight and D_{ij} denotes the ordinary multicomponent diffusion coefficients. The diffusion driving force in general form is given by:

$$\vec{d_j} = \frac{1}{cRT}\left[\vec{\nabla} p_j - y_j \vec{\nabla} p - \rho_j \vec{g_j} + \sum_{k=1}^{N} \rho_k \vec{g_k}\right] \tag{3.9}$$

where c is the total molar concentration, p_j is the species partial pressure and $\vec{g_j}$ is any (external) force per unit mass acting on species j. The second term on the right-hand side of Eq. 3.8 represents thermal diffusion, also known as the Soret effect.

The chemical source term in Eq. 3.6 can be expressed as [120]:

$$\vec{r_i} = M_i \sum_{j=1}^{R} \left(\nu''_{ij} - \nu'_{ij}\right) \left[k_{f,j} \prod_{l=1}^{N} c_l^{\nu'_{ij}} - k_{b,j} \prod_{l=1}^{N} c_l^{\nu''_{ij}}\right] \tag{3.10}$$

In this relation c_l denote concentrations of the N different species l, $k_{f,j}$ and $k_{b,j}$ are the forward and backward reaction rate constants for reaction j, and ν'_{ij} and ν''_{ij} are the stoichiometric coefficients of reactants and products. The reaction rate constants are determined using the Arrhenius equation:

$$k = Ae^{\frac{-Ea}{RT}}, \tag{3.11}$$

where A is the pre-exponential factor, E_a is the activation energy and R is the universal gas constant.

3.1.2 Thermophysical properties of supercritical water

The properties of water at different conditions are obtained using the Industrial Formulation 1997 [115] adopted by the International Association for the Properties of Water and Steam (IAPWS). The industrial formulation, abbreviated to IAPWS-IF97, was designed to closely approximate the values from the state of the art, high accuracy formulation IAPWS-95 [118] over a limited range of conditions.

In contrast to the single-equation IAPWS-95 standard, the IF97 formulation consists of a set of equations for five different regions [116] (see Fig. 3.1). For each region a basic equation was developed from which thermo-physical properties such as specific volume, enthalpy and heat capacity can be derived. Regions 1, 2 and 5 are each covered by a fundamental equation for the specific Gibbs free energy g(p, T), region 3 by a fundamental equation for the specific Helmholtz free energy f(ρ, T). The advantage of using the Gibbs energy is that this equation has the pressure as an input quantity so that iterations are not necessary for given p,T values (W. Wagner, personal communication, May 28, 2011). However, this equation cannot be used for the entire thermodynamic surface since the pressure is the same at the bubble and dew line for given temperatures at the phase boundary. Therefore, different equations are needed for region 1 and 2. The reason why using the Helmholtz equation for region 3, which also contains the critical region, is that the Gibbs equation is unsuitable for representing the large changes in thermodynamic properties in this rather complex region. A Helmholtz equation is able to represent this region more accurately and with a shorter expression because the ρ, T surface is not as complicated as the p, T surface.

In addition, so-called backward equations were developed to efficiently calculate the state properties when using other input variables than needed for the basic equations. High numerical consistency across the region boundaries is achieved to ensure a smooth transition between the different sets of equations.

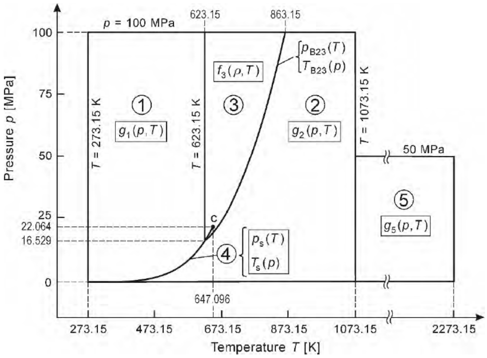

Figure 3.1: *The IAPWS-IF97 regions [116]*

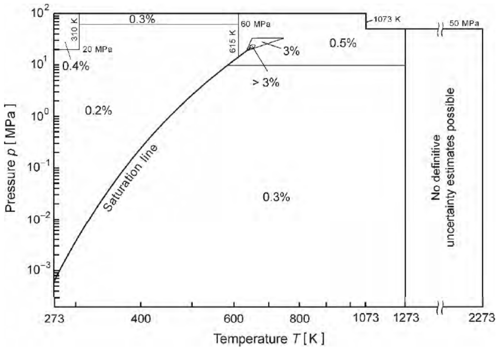

Figure 3.2: *Percentage uncertainties in specific isobaric heat capacity estimated for regions 1 to 3 and 5 [116].*

Transport properties, in this study the thermal conductivity and viscosity, are calculated from supplementary equations provided by IAPWS.

The industrial standard offers easier numerical implementation and higher computational speed compared to the high accuracy standard, while the differences between the two formulations are small for most purposes. The estimated uncertainties in the industrial standard are the result of two contributions: uncertainties of the IAPWS-95 formulation, which was used for developing the IAPWS-IF97 basic equations, and deviations of IAPWS-IF97 from IAPWS-95. Considering the range where calculations are performed in this study (240 < p < 300 bar, 573 < T < 873 K), the combined uncertainty in specific volume is estimated to be less than 0.3%. Uncertainty percentages for the isobaric heat capacity are generally within 0.5%, but rise to 3% in the critical region and even more very near to the critical point (Fig. 3.2). Uncertainties in thermal conductivity and viscosity are given in terms of tolerances in tables with a uniform p-T grid. From these datapoints, it appears that k and μ are generally calculated with an accuracy well within 5% [43, 101]. This percentage is only exceeded in a small region around the critical point (200 < p < 250 bar, 350 < T < 400 °C), where the estimated uncertainty is around 10%.

The accuracy of the IAPWS-IF97 formulation is considered sufficient for the simulations to be performed in this study. Detailed information on the basic equations covering the regions shown in Fig. 3.1 follows in the description of the mathematical background below. All basic equations are expressed in dimensionless form by using dimensionless state variables according to the following definitions:

$$\begin{gathered}
\frac{p}{p^*} \equiv \pi \qquad \frac{T}{T^*} \equiv \theta \qquad \frac{T^*}{T} \equiv \tau \qquad \frac{\rho}{\rho^*} \equiv \delta \\
\frac{g(p,T)}{R_s T} \equiv \gamma(\pi,\tau) \qquad \frac{f(\rho,T)}{R_s T} \equiv \phi(\delta,\tau) \\
\frac{k(\rho,T)}{k^*} \equiv \kappa(\delta,\theta) \qquad \frac{\mu(\rho,T)}{\mu^*} \equiv \Psi(\delta,\theta)
\end{gathered} \tag{3.12}$$

where the quantities marked with an asterisk (*) are specific for the different regions. Since the calculations in this study only involve properties in regions 1 to 3, a discussion of regions 4 and 5 is omitted. Also the backward equations are not described in this thesis.

Region 1

In terms of the dimensionless variables shown in Eq. 3.12, the equation for the specific Gibbs free energy that covers region 1 reads:

$$\gamma(\pi,\tau) = \sum_{i=1}^{34} n_i (7.1 - \pi)^{I_i} (\tau - 1.222)^{J_i} \tag{3.13}$$

where $p^* = 16.53$ MPa and $T^* = 1386$ K. The specific gas constant of ordinary water $R_s = 0.461526$ kJ/kgK. Coefficients n_i and exponents I_i and J_i are listed in a table found in Wagner and Kretzschmar (2008) [116]. Thermodynamic properties can be derived from Eq. 3.13 by using appropriate combinations of the dimensionless Gibbs free energy γ and its derivatives. The specific volume v, specific enthalpy h, specific isobaric heat capacity C_p and isobaric cubic expansion coefficient β are given by:

$$v = \left(\frac{\partial g}{\partial p}\right)_T \qquad h = g - T\left(\frac{\partial g}{\partial T}\right)_p \qquad C_p = \left(\frac{\partial h}{\partial T}\right)_p \qquad \beta = \frac{1}{v}\left(\frac{\partial v}{\partial T}\right)_p \tag{3.14}$$

which yields the following relations of v, C_p and β to the dimensionless Gibbs free energy γ:

$$v(\pi,T)\frac{p}{R_s T}=\pi\gamma_\pi \qquad \frac{C_p(\pi,T)}{R_s}=-\tau^2\gamma_{\tau\tau} \qquad \beta(\pi,T)T=1-\frac{\tau\gamma_{\pi\tau}}{\gamma_\pi} \tag{3.15}$$

where the subscripts of γ denote partial derivatives.

Region 2

In the basic equation for region 2, the dimensionless form of the specific Gibbs free energy is separated into an ideal-gas part γ^0 and a residual part γ^r, so that:

$$\gamma(\pi,\tau)=\gamma^0(\pi,\tau)+\gamma^r(\pi,\tau) \tag{3.16}$$

where $p^*=1$ MPa and $T^*=540$ K. The equation for the dimensionless ideal-gas part is given by:

$$\gamma^0(\pi,\tau)=\ln\pi+\sum_{i=1}^{9} n_i^0\tau^{J_i^0} \tag{3.17}$$

while the residual part reads:

$$\gamma^r(\pi,\tau)=\sum_{i=1}^{43} n_i\pi^{I_i}(\tau-0.5)^{J_i} \tag{3.18}$$

According to the definitions stated in Eq. 3.14, v, C_p and β are now calculated as follows:

$$v(\pi,\tau)\frac{p}{R_s T}=\pi(\gamma_\pi^0+\gamma_\pi^r) \qquad \frac{C_p(\pi,\tau)}{R_s}=-\tau^2(\gamma_{\tau\tau}^0+\gamma_{\tau\tau}^r)$$

$$\beta(\pi,\tau)T=\frac{1+\pi\gamma_\pi^r-\tau\pi\gamma_{\pi\tau}^r}{1+\pi\gamma_\pi^r} \tag{3.19}$$

A supplementary equation for the metastable-vapor region is provided for pressures below 10 MPa. For the metastable region, the ideal gas part γ^0 is identical to Eq. 3.17 except for the coefficients n_1^0 and n_2^0, and the residual part is given by:

$$\gamma^r(\pi,\tau)=\sum_{i=1}^{13} n_i \pi^{I_i}(\tau-0.5)^{J_i}. \tag{3.20}$$

Region 3

For region 3, the basic equation is a fundamental equation for the specific Helmholtz free energy:

$$\phi(\delta,\tau)=n_1 \ln\delta+\sum_{i=2}^{40} n_i \delta^{I_i}\tau^{J_i} \tag{3.21}$$

where $\rho^*=\rho_c=322$ kg/m^3 and $T^*=T_c=647.096$ K. The pressure, specific enthalpy, specific isobaric heat capacity and expansion coefficient are now calculated according to:

$$\begin{gathered} p=\rho^2\left(\frac{\partial f}{\partial \rho}\right)_T \quad h=f-T\left(\frac{\partial f}{\partial T}\right)_\rho+\rho\left(\frac{\partial f}{\partial \rho}\right)_T \\ C_p=\left(\frac{\partial h}{\partial T}\right)_p \quad \beta=\frac{1}{v}\left(\frac{\partial v}{\partial T}\right)_p \end{gathered} \tag{3.22}$$

which give the relations:

$$\begin{gathered} \frac{p(\delta,\tau)}{\rho R_s T}=\delta\phi_\delta \qquad \frac{h(\delta,\tau)}{R_s T}=\tau\phi_\tau+\delta\phi_\delta \\ \frac{C_p(\delta,\tau)}{R_s T}=\tau^2\phi_{\tau\tau}+\frac{(\delta\phi_\delta-\delta\tau\phi_{\delta\tau})^2}{2\delta\phi_\delta+\delta^2\phi_{\delta\delta}} \qquad \beta(\delta,\tau)T=\frac{\phi_\delta-\tau\phi_{\delta\tau}}{2\phi_\delta+\delta\phi_{\delta\delta}}, \end{gathered} \tag{3.23}$$

The boundary between regions 1 and 2 is considered to belong to region 1, which means properties along this boundary are determined from Eq. 3.13.

The boundary between regions 2 and 3 is considered to belong to region 2 and is defined by the following quadratic pressure-temperature relation:

$$\frac{p_{B23}(T)}{p^*} = \pi(\theta) = n_1 + n_2\theta + n_3\theta^2 \tag{3.24}$$

where $p^* = 1$ MPa and $T^* = 1$ K. This equation can also be expressed explicitly as a function of pressure.

The correlation equation for the thermal conductivity for industrial use is based on the revised IAPWS formulation 1985 for the thermal conductivity of ordinary water substance [43]. In this formulation, the equation for the thermal conductivity is given in dimensionless form as follows:

$$\kappa(\delta,\theta) = \kappa_0(\theta) + \kappa_1(\delta) + \kappa_2(\delta,\theta) \tag{3.25}$$

where $k^* = 1$[W/mK], $\rho^* = 317.7$ kg/m^3 and $T^* =$647.26 K. The function $\kappa_0(\theta)$ represents the thermal conductivity in the ideal gas limit and has the form:

$$\kappa_0(\theta) = \theta^{0.5} \sum_{i=1}^{4} n_i^0 \theta^{i-1} \tag{3.26}$$

The correlation for $\kappa_1(\delta)$ in 3.25 reads:

$$\kappa_1(\delta) = n_1 + n_2\delta + n_3 \exp\left[n_4(\delta + n_5)^2\right] \tag{3.27}$$

The function $\kappa_2(\delta,\theta)$ is defined by:

$$\begin{aligned}\kappa_2(\delta,\theta) \quad = \quad & \left(n_1\theta^{-10} + n_2\right)\delta^{1.8} \exp\left[n_3\left(1 - \delta^{2.8}\right)\right] \\ & + n_4 A \delta^B \exp\left[\left(\frac{B}{1+B}\right)\left(1 - \delta^{1+B}\right)\right] \\ & + n_5 \exp\left[n_6\theta^{1.5} + n_7\delta^{-5}\right]\end{aligned} \tag{3.28}$$

with A and B according to:

$$A(\theta)=2+n_8(\Delta\theta)^{-0.6}$$

$$B(\theta)=\begin{cases}(\Delta\theta)^{-1} & \text{for } \theta\geq 1\\ n_9(\Delta\theta)^{-0.6} & \text{for } \theta<1\end{cases}$$

$$\Delta\theta=|\theta-1|+n_{10} \tag{3.29}$$

The viscosity is calculated using revised equations of the IAPWS formulation 1985 for the viscosity of ordinary water substance [101]. In dimensionless form, the viscosity is given by:

$$\Psi(\delta,\theta)=\Psi_0(\theta)\cdot\Psi_1(\delta,\theta)\cdot\Psi_2(\delta,\theta) \tag{3.30}$$

where $\mu^*=55.071.10^{-6}$ Pa.s, $\rho^*=317.763$ kg/m^3 and T^*=647.226 K. The first function on the right-hand side represents the viscosity in the ideal gas limit and has the form:

$$\Psi_0(\theta)=\theta^{0.5}\left[\sum_{i=0}^{3}H_i\theta^{-i}\right]^{-1} \tag{3.31}$$

with coefficients H_i listed in a table. The equation for the second function of Eq. 3.30 reads:

$$\Psi_1(\delta,\theta)=\exp\left[\delta\sum_{i=0}^{5}\sum_{j=0}^{6}H_{ij}(\theta^{-1}-1)^i(\delta-1)^j\right] \tag{3.32}$$

with coefficients H_{ij} given in a table [116]. For industrial use, Ψ_2 in Eq. 3.30, may be set to unity. This so-called critical enhancement is only significant in a very small region around the critical point (the oval area around the critical point in Fig. 3.2).

3.1.3 Characteristics of heat transfer to supercritical fluids

Prior to a discussion of the models and their results, it is useful to investigate the phenomena related to heat transfer to fluids at supercritical conditions. The main driving force for research activities in this field has been the development of nuclear power plants using SCW as the working fluid in order to improve thermal efficiency relative to existing nuclear plant designs [83]. Although the flow conditions around are not necessarily equal to those in a reactor for SCW gasification, the two research topics are essentially very similar. Thanks to the work done on heat transfer to supercritical water in flow channels for new power plant designs, quite some information is available which can be built on. An overview of the most important and relevant phenomena, characteristics and expressions for heated fluid flows at supercritical pressures are given below.

In literature dealing with heat transfer to pipe flows at supercritical pressures, it is generally agreed that deviations from 'normal' heat transfer are observed [30]. Normal heat transfer here refers to single-phase heat transfer at subcritical pressures described by the well-known Dittus-Boelter correlation [36]:

$$\mathrm{Nu} = 0.023\mathrm{Re}^{0.8}\mathrm{Pr}^{0.4} \tag{3.33}$$

where Nu, Re and Pr are the Nusselt, Reynolds and Prandtl numbers. Measurements show that deviations from normal heat transfer particularly occur when the wall temperature is higher than the pseudo-critical temperature, while the bulk temperature is below the pseudo-critical temperature ($T_w > T_{pc} > T_b$). In this situation, large thermo-physical property variations in the near-wall region can greatly affect heat transfer. Depending on the flow conditions, the variations in fluid properties can result in enhancement, impairment or deterioration of heat transfer. These observations may be explained by considering two boiling phenomena that possibly take place along the heated surface [19].

Boiling phenomena

One of these two boiling phenomena is pseudo-boiling [104]. Similar to nucleate boiling at subcritical pressures, low-density bubbles are formed at the hot wall where the fluid locally exceeds the pseudocritical temperature, while

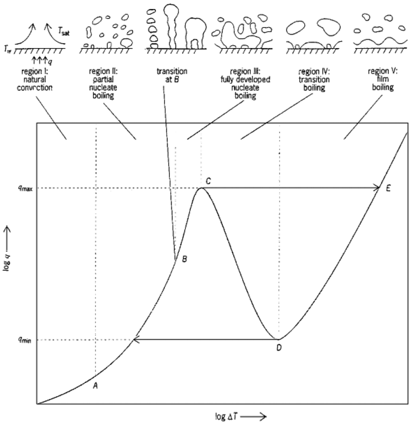

Figure 3.3: *Typical boiling curve, showing qualitatively the dependence of the wall heat flux, q, on the wall superheat, Δ T, defined as the difference between the wall temperature and the saturation temperature of the liquid [32].*

the bulk fluid is below the pseudocritical temperature. At some point the bubbles break loose from the heating surface and are carried into the bulk fluid, thereby transferring heat from the surface to the fluid stream quite effectively. Together with the agitation caused by the rising bubbles, this phenomenon results in enhancement of the heat transfer rate.

When the temperature is raised further, the heat transfer rate increases until the heat flux reaches a critical value. At this point, the rate of vaporization is such that dry patches occur over the heating surface, causing the rate of heat transfer to drop rapidly. At sufficiently high temperature differences, the entire surface is blanketed with a gas layer that prevents the liquid water from contacting the wall. Heat transfer then relies on the mechanism of conduction through the gaseous water film and radiation. This phenomenon is called pseudo-film boiling and is considered responsible for deterioration of the heat transfer rate. The effect of pseudo boiling and pseudo-film boiling on the heat flux is schematically shown in Fig. 3.3.

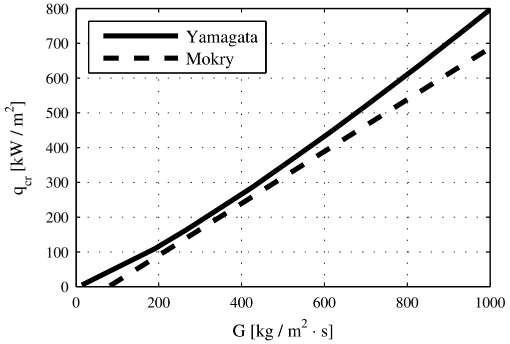

Figure 3.4: *Prediction of the critical heat flux as function of the mass flux using the correlations of Yamagata et al. (1972) [133] and Mokry et al. (2011) [83].*

Critical heat flux

Studies on the heat flux at which pseudo-film boiling can occur, called the critical heat flux, has led to several correlations predicting the onset of heat transfer deterioration [29]. Large deviations are observed between the different correlations cited by Cheng et al. [29], but it is well agreed that the critical heat flux depends on the mass flux. Jackson and Hall [52] have suggested a correlation based on theoretical analysis of the effect of buoyancy on the shear stress. Two other theoretical models have been derived by Ogata and Sato [89] and Petuhkov and Kurganov [93]. These three semi-empirical correlations give much higher values for the critical heat flux than the empirical correlations. Possible reasons for the deviations can be found in the fact that Jackson and Hall noticed that the validity of their equation was not properly investigated, and that the other two correlations have been derived for fluids other than water.

The most relevant correlations for this study have been proposed bij Yamagata et al. [133] and Mokry et al. [83] on basis of experimental data from supercritical water in a 10 mm pipe. Yamagata et al. [133] derived a power law to correlate the critical heat flux q_{cr} to the mass flux G:

$$q_{cr} = 0.2 \cdot G^{1.2} \tag{3.34}$$

while Mokry et al. [83] found a linear relation between these parameters:

$$q_{cr} = -58.97 + 0.745 \cdot G \tag{3.35}$$

The critical heat flux as predicted by Eqs. 3.34 and 3.35 are plotted as a function of the mass flux in Fig. 3.4.

Buoyancy effects

Next to the boiling phenomena described above, literature points out that the accelerating low-density layer near the wall has considerable influence on the heat transfer rate as well [5, 27, 72]. Due to the buoyancy forces resulting from variations in density, the heat transfer mechanism can be a combination of forced and natural convection. In case the fluid is heated with upward flow or cooled down with downward flow, buoyancy effects aid forced convection since velocities due to natural and forced convection are in the same direction. This situation is called aiding flow, which shows very different heat transfer behavior from opposing flow, where the driving forces or natural and forced convection are in opposite direction.

The contribution of natural convection in relation to forced convective heat transfer depends on many conditions such as flow velocity, wall temperature and flow direction (aiding versus opposing flow). Aicher and Martin [5] proposed the following criterium to compare the driving forces of the two types of convective heat transfer in turbulent flow in case of constant wall temperature:

$$\frac{Ra^{0.333}}{Re^{0.8} Pr^{0.4}} \tag{3.36}$$

In this criterium, the Rayleigh number Ra characterizes the strength of the buoyancy forces. It is defined as the product of the Grashof number, which describes the relationship between buoyancy and viscosity, and the Prandtl

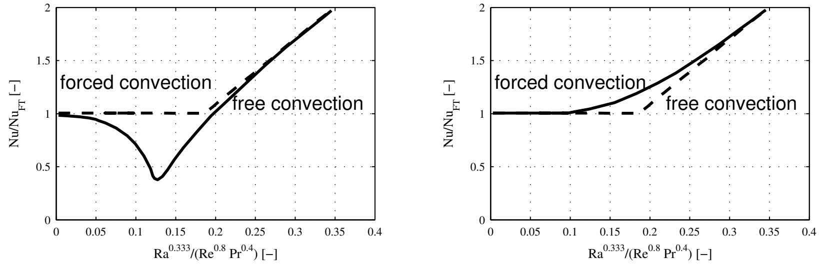

(a) Aiding flow.

(b) Opposing flow.

Figure 3.5: *Schematic view of the influence of buoyancy forces on heat transfer [5].*

number, which is the ratio of momentum diffusivity to thermal diffusivity:

$$\begin{aligned} Ra &= Gr \cdot Pr \\ &= \frac{g\beta(T_w - T_b)D^3}{\nu^2} \cdot \frac{\nu}{\alpha} \\ &= \frac{g\beta}{\nu\alpha}(T_w - T_b)D^3 \end{aligned} \tag{3.37}$$

where g is the gravitational acceleration, β is the cubic expansion coefficient, ν is the kinematic viscosity and α is the thermal diffusivity. The Reynolds number Re in Eq. 3.36 compares the dynamic pressure to the shear stress acting on the fluid:

$$Re = \frac{\rho u D}{\mu}. \tag{3.38}$$

For aiding flow, natural convection is the dominant heat transfer mechanism if the parameter of Aicher and Martin exceeds 0.2. If less than 0.05, forced convection is dominating. The range in between indicates the mixed convection regime. The influence of buoyancy forces on heat transfer is schematically shown in Fig. 3.5. Here, the ratio between Nu and Nu_{FT} is plotted against the parameter of Eq. 3.36. Nu_{FT} is defined as the Nusselt number for 'normal' forced convection and is described by the Dittus-Boelter equation, Eq. 3.33.

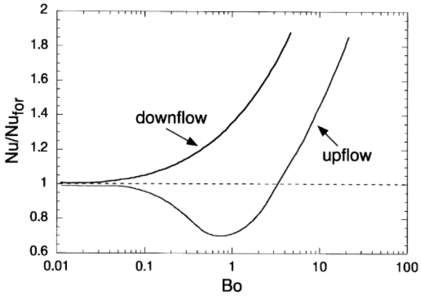

Figure 3.6: *Schematic view of heat transfer for aiding and opposing mixed convection [27].*

A similar criterium, defined as the buoyancy parameter Bo, was more recently presented for constant wall heat flux by Celata et al. [27], although originally developed by Jackson and Hall [52]:

$$Bo = 8 \cdot 10^4 \frac{Gr_q}{Re^{3.425} Pr^{0.8}}. \tag{3.39}$$

In this expression, fluid properties are evaluated at film temperature and the Grashof number, Gr_q, is based on the wall heat flux. Comparing Fig. 3.5 with the graph in Fig. 3.6, where the buoyancy parameter Bo is on the horizontal axis, the same behaviour of the normalized Nusselt number is observed. Celata et al. [27] showed experimentally that the mixed convection region corresponds with values of Bo between 0.03 and 3.

The effect of buoyancy forces on the rate of heat transfer may be explained by considering the turbulence production between the viscous layer and the bulk flow [27, 72]. In aiding flow, the fluid layer adjacent to the heated wall is subject to a buoyancy force which acts in the same flow direction. Therefore, buoyancy forces tend to reduce the shear stress in the layer, reducing turbulent diffusion of heat and thus causing deteriorated heat transfer. As the temperature of the fluid in the near-wall region increases further, density differences cause the low-density fluid to outrun the bulk flow. This restores the turbulence production and hence heat transfer, as is seen in Fig. 3.5 and Fig. 3.6. Typical examples of velocity profiles and shear stress distributions are shown in Fig.

3.7 [108]. With increasing Buoyancy effects from profile A to F, shear stress is first decreased, but eventually reintroduced in opposite direction when the velocity of the low-density fluid is higher than the bulk velocity.

The different heat transfer regimes that can be discerned due to the phenomena discussed above have been illustrated by Licht et al. [72]. A schematic visualization of each regime and the effect on the heat transfer compared to normal heat transfer (with no property variations) is given in Fig. 3.8.

On basis of the information given in this section, the cases that have been considered in this study can be properly classified. By using terminology, expressions and criteria in agreement with existing literature on this topic, interpretation of the simulation results and comparisons with earlier work is facilitated. Two different heated upflow cases are chosen for analysis. The first and main case is representative for supercritical gasification of biomass on pilot plant scale. The simulations on the pilot plant case cover both heat transfer and chemistry. The second case, which is on lab scale, is only intended for validation of the 2D-simulation results using experimental data from a test setup in the laboratory. The specifications of these two cases are listed in Table 3.1.

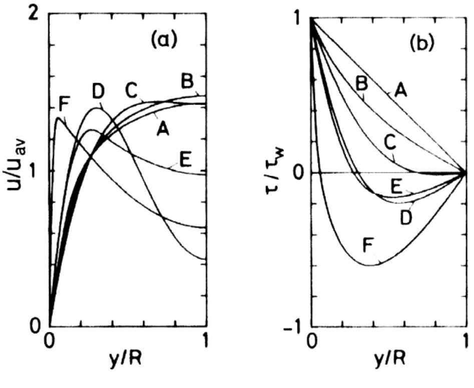

(a) Velocity.

(b) Shear stress.

Figure 3.7: *Distributions at various Grashof numbers at a constant Re = 3000. A, Gr = 2.1.10*^{3}*, turbulent; B, Gr = 6.1.10*^{4}*, turbulent; C, Gr = 8.8.10*^{4}*, laminar; D, Gr = 2.7.10*^{5}*, laminar; E, Gr = 3.3.10*^{5}*, turbulent; F, Gr = 9.2.10*^{6}*, turbulent [108].*

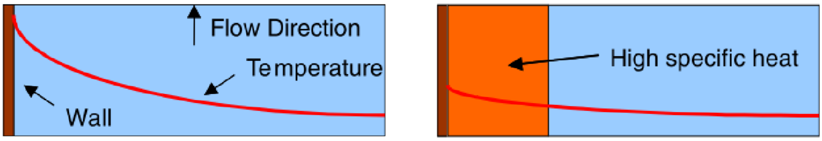

(a) Normal heat transfer. (b) Enhancement.

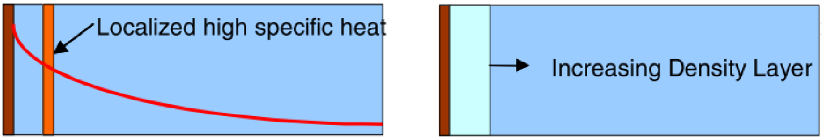

(c) Impairment of enhanced heat transfer. (d) Deterioration.

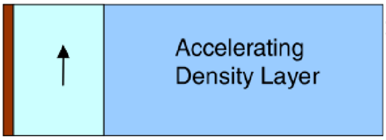

(e) Recovery.

Figure 3.8: *Illustration of the different heat transfer regimes [72].*

Additional to the case specified in Table 3.1, heat transfer was simulated for a lower inlet temperature, lower mass flux and shorter pipe with the intention to validate the 2D-model using experimental data from a test setup in the laboratory. The experimental efforts and 2D-simulations for validation of the numerical model are discussed in Section 4.8.

3.2 1D heat transfer model of a flow reactor with supercritical water

The governing equations described in Section 3.1.3 are being simplified by using a 1D-modeling approach, in order to develop a fast simulation tool with reasonable accuracy. With this aim in mind, the reactor is described using a plug flow reactor model [14]. By disregarding all variations in radial direction, the dimensions of the computational domain are reduced to only one coordinate. Moreover, all terms having no major contribution to the solution are neglected, which results in a set of equations that can be solved efficiently. The results are compared to the more advanced 2D-simulations and experimental data in Chapter 4 to assess the accuracy of this model.

This section contains a detailed description of the simplification procedure. In addition, three Nusselt correlations are selected from literature to close the set of simplified equations. The accuracy of the new model is assessed in Section 3.3 by comparing the calculation results to experimental data found in Mokry et al. [84].

3.2.1 Physical and computational domain

Due to the plug flow assumption only variations in axial direction are considered, so that the radial coordinate is of no importance in the calculations. However, there still needs to be a temperature difference across the radius in order to describe heat transfer through the pipe wall. Since it is impossible to physically describe the heated pipe flow using only one spatial dimension, a distinction is made between the physical and computational domain to give more insight into the modeling approach. The physical domain is represented by a 2D fluid domain that is bounded by an infinitely thin pipe wall as shown in Fig. 3.9.

The schematic temperature and velocity profiles $T'(r,z)$ and $u'(r,z)$ shown in the figure become radial averaged quantities $T(z)$ and $u(z)$ in the compu-

Table 3.1: *Specification of the cases that are considered in this study.*

Parameters	Symbol	Unit	Case 1	Case 2	Case 3
Inlet mass flux	G	[kg/m^{2}s]	1000	500	200
Pressure	p	[bar]	241	241	241
Inner Diameter	D	[mm]	10	10	10
L to D ratio	L/D	[-]	400	400	400
Inlet temperature	T_{in}	[°C]	350	350	350

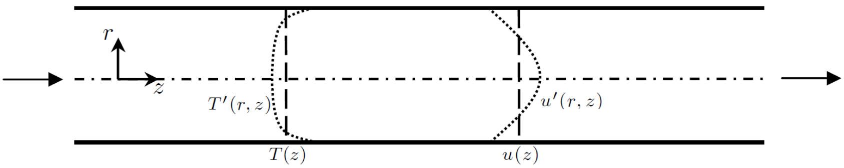

Figure 3.9: *Physical domain for the 1D-model.*

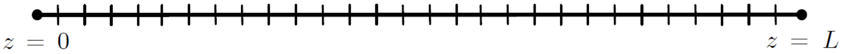

Figure 3.10: *Computational domain for the 1D-model.*

tational domain. The relation between the 2D temperature profile and the radial-averaged profile is given by:

$$T(z) = \frac{1}{r_0}\int_0^{r_0} T'(r,z)\,dr. \tag{3.40}$$

Since the model equations will be independent of the radial coordinate, the physical domain can be reduced to a line in the computational domain (Fig. 3.10).

On basis of a mesh convergence analysis using the bulk temperature as the indicative variable, the domain has been divided into 750 elements for the simulations. The results of the convergence analysis using the conditions of Cases 1 and 2, defined in Table 3.1, are plotted in Fig. 3.11, showing an estimated accuracy of within 1 K for this mesh. The chosen mesh size leads to CPU-times of a couple of seconds on a single-core laptop for a tube length of 4.0 m.

In the one-dimensional computational domain, the heat source term $\dot{Q}$ in Eq. 3.41 can be used to account for the heat that is transferred from the pipe wall to the fluid by convection [50]. The heat addition per unit time in an infinitesimal control volume dV is:

$$\dot{Q}\,dV = -(\vec{q}\cdot\vec{n}_w)\,dS_w \tag{3.41}$$

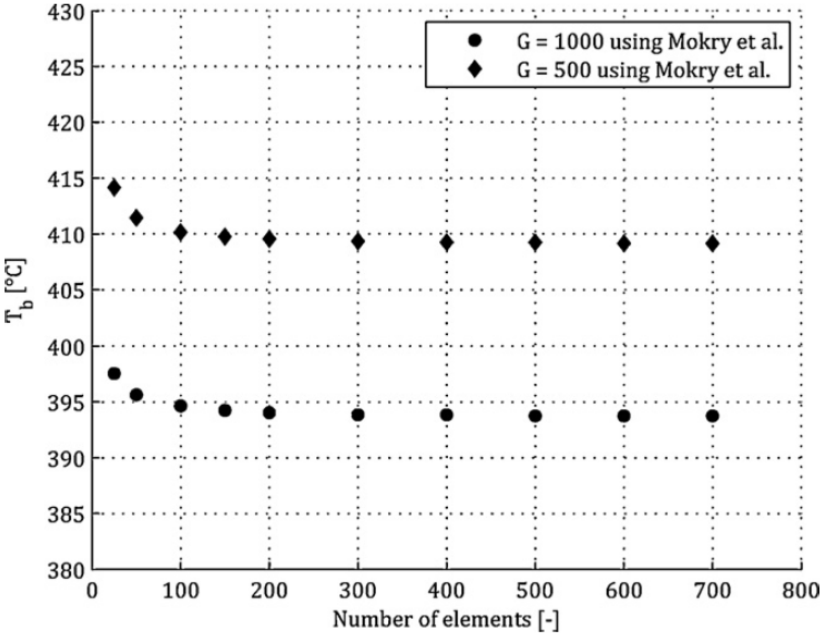

Figure 3.11: *Mesh convergence analysis for the 1D-model using the Nusselt correlation of Mokry et al. [84].*

where $\vec{n}_w$ is the outward-pointing normal unit vector on the wall of the fluid domain and dS_w the surface area of the outer pipe wall surrounding the control volume. The convective heat flux is modeled by Newton's law of cooling:

$$-\vec{q}\cdot\vec{n}_w \equiv q_w = h(T_w - T) \tag{3.42}$$

where the heat transfer coefficient h follows from a Nusselt correlation found in literature. A discussion of available Nusselt correlations for supercritical water flows is found in Section 3.2.3. Combining Eqs. 3.41 and 3.42 gives:

$$\dot{Q} = \frac{4}{D}h(T_w - T) \tag{3.43}$$

3.2.2 1D-model equations

This section describes the steps taken to derive the 1D-model equations from the governing equations given in Section 3.1.1. The simplification starts by writing the equations in one-dimensional form and by assuming a system operating in steady state. The mass conservation equation, Eq. 3.1, then becomes:

$$\frac{d}{dz}(\rho u) = 0. \tag{3.44}$$

Eq. 3.44 shows that the mass flux ρu is constant. Although this quantity is exactly equal to G, defined in Section 3.1.3, the mass flux will be written as $(\rho u)_0$ in the conservation equations for clarity.

In the momentum equation, Eq. 3.2 the z-component of the volumetric force vector is equal to the gravitational acceleration:

$$f_z = -g. \tag{3.45}$$

The dilatational viscosity κ in Eq. 3.3 is usually neglected for practical purposes because the availability of these data is very limited. It is only important to model effects when fluid compressibility is essential, in case of shock waves and sound propagation, therefore it can be omitted in this study. The divergence of the viscous stress tensor for a one-dimensional plug flow then reduces to:

$$\vec{\nabla} \cdot \vec{\vec{\tau}} = -\frac{4}{3}\mu \frac{d^2 u}{dz^2}, \tag{3.46}$$

where μ is the dynamic viscosity of the fluid. After substitution of Eqs. 3.45 and 3.46 and subtraction of Eq. 3.44, the equation for momentum conservation given by Eq. 3.2 becomes:

$$\rho u \frac{du}{dz} = -\frac{dp}{dz} + \frac{4}{3}\mu \frac{d^2 u}{dz^2} - \rho g. \tag{3.47}$$

When the kinetic energy in the fluid is assumed to be negligible in comparison with the internal energy, a simplified form of the energy equation can be used in which the temperature appears [21]. This equation can be derived from the total energy equation by assuming that the mechanical energy is negligible. The procedure starts by writing the energy equation in terms of internal energy. The internal energy is by definition related to the total energy by:

$$E \equiv e + \frac{1}{2}|\vec{u}|^2. \tag{3.48}$$

Substitution of Eq. 3.48 into Eq. 3.4 results in:

$$\begin{aligned} \frac{\partial\left(\rho e + \frac{1}{2}\rho|\vec{u}|^2\right)}{\partial t} &= -\vec{\nabla}\cdot\left(\left(\frac{1}{2}\rho|\vec{u}|^2 + \rho e\right)\vec{u}\right) + \rho\left(\vec{f}\cdot\vec{u}\right) - \vec{\nabla}\cdot(p\vec{u}) \\ &\quad -\vec{\nabla}\cdot(\vec{\vec{\tau}}\cdot\vec{u}) + \dot{Q} - \vec{\nabla}\cdot\vec{q}. \end{aligned} \tag{3.49}$$

An expression for the mechanical energy is obtained by taking the dot product of $\vec{u}$ with the momentum equation. Multiplication of Eq. 3.2 by $\vec{u}$ yields:

$$\begin{aligned} \frac{\partial}{\partial t}\left(\frac{1}{2}\rho|\vec{u}|^2\right) &= -\vec{\nabla}\cdot\left(\frac{1}{2}\rho|\vec{u}|^2\vec{u}\right) + \rho\left(\vec{f}\cdot\vec{u}\right) - \vec{\nabla}\cdot(p\vec{u}) - p\left(-\vec{\nabla}\cdot\vec{u}\right) \\ &\quad -\vec{\nabla}\cdot(\vec{\vec{\tau}}\cdot\vec{u}) - \left(-\vec{\vec{\tau}}:\vec{\nabla}\vec{u}\right). \end{aligned} \tag{3.50}$$

Subtracting Eq. 3.50 from Eq. 3.49 yields the equation of change for internal energy:

$$\frac{\partial}{\partial t}(\rho e) = -\vec{\nabla}\cdot(\rho e\vec{u}) - p\left(\vec{\nabla}\cdot\vec{u}\right) - \left(\vec{\vec{\tau}}:\vec{\nabla}\vec{u}\right) + \dot{Q} - \vec{\nabla}\cdot\vec{q}. \tag{3.51}$$

Eq. 3.51 can be written somewhat more compactly by using the material derivative and the definition of enthalpy $h \equiv e + (p/\rho)$:

$$\rho\frac{Dh}{Dt} = \frac{Dp}{Dt} - \left(\vec{\vec{\tau}}:\vec{\nabla}\vec{u}\right) + \dot{Q} - \vec{\nabla}\cdot\vec{q}. \tag{3.52}$$

The term on the left-hand side is evaluated in order to obtain an equation in terms of temperature:

$$\begin{aligned}
\rho \frac{Dh}{Dt} &= \rho \left(\frac{\partial h}{\partial T}\right)_p \frac{DT}{Dt} + \left(\frac{\partial h}{\partial p}\right)_T \frac{Dp}{Dt} \\
&= \rho C_p \frac{DT}{Dt} + \rho \left[\frac{1}{\rho} - T\left(\frac{\partial(1/\rho)}{\partial T}\right)_p\right] \frac{Dp}{Dt} \\
&= \rho C_p \frac{DT}{Dt} + \left[1 + \frac{T}{\rho}\left(\frac{\partial \rho}{\partial T}\right)_p\right] \frac{Dp}{Dt}.
\end{aligned} \tag{3.53}$$

Substitution into Eq. 3.52 gives the equation of change for temperature:

$$\rho C_p \frac{DT}{Dt} = -\frac{T}{\rho}\left(\frac{\partial \rho}{\partial T}\right)_p \frac{Dp}{Dt} - \left(\vec{\vec{\tau}} : \vec{\nabla}\vec{u}\right) + \dot{Q} - \vec{\nabla}\cdot\vec{q} \tag{3.54}$$

Eq. 3.5 describing the local heat flux $\vec{q}$ can be simplified by neglecting energy transport due to mass diffusion and dropping the Duffour term, resulting in Fourier's law of heat conduction:

$$\vec{q} = -k\vec{\nabla}T. \tag{3.55}$$

where k is the thermal conductivity of the fluid. The second term on the right-hand side of Eq. 3.54 describes viscous dissipation heating. For Newtonian fluids, this quantity is always positive and can be written in the form of a viscous dissipation function ϕ_v:

$$-\left(\vec{\vec{\tau}} : \vec{\nabla}\vec{u}\right) = \mu\phi_v. \tag{3.56}$$

Substitution of Eqs. 3.55 and 3.56 into Eq. 3.54 and replacing the heat source term by Eq. 3.43 yields:

$$\rho C_p \frac{DT}{Dt} = -\frac{T}{\rho}\left(\frac{\partial \rho}{\partial T}\right)_p \frac{Dp}{Dt} + \mu\phi_v + \frac{4}{D}h(T_w - T) + \vec{\nabla}\cdot\left(k\vec{\nabla}T\right). \tag{3.57}$$

For one-dimensional flow in steady state this becomes:

$$\begin{aligned}\rho C_p u \frac{dT}{dz} &= -\frac{T}{\rho}\left(\frac{\partial \rho}{\partial T}\right)_p u \frac{dp}{dz} + \frac{4}{3}\mu \left(\frac{du}{dz}\right)^2 + \frac{4}{D} h (T_w - T) \\ &\quad + \frac{d}{dz}\left(k \frac{dT}{dz}\right). \end{aligned} \tag{3.58}$$

The momentum and energy Eqs. 3.47 and 3.58 can be simplified further by neglecting all terms that have a negligible influence on the exact solution. These terms may be identified if the equations are rewritten in dimensionless form [21]. Evaluation of the resulting dimensionless groups and comparing their order of magnitude provides information on the relative importance of the different terms.

In the following procedure, fluid properties are assumed constant. Density, conductivity and viscosity are taken as the linear average of the minimum and maximum values that are to be expected in the system, which are listed in Table 3.2.

The extrema shown are derived from the properties of water in the range between the inlet temperature and wall temperature. The mean velocity can be derived from Eq. 3.44 using the mean density. A representative mean value for the heat capacity at isobaric conditions is given by:

Table 3.2: *System range for several quantities.*

Parameter	**Symbol**	**Unit**	**Minimum**	**Maximum**
Longitudinal coordinate	z	[m]	0	4.0
Temperature	T	[°C]	350	500
Density	ρ	[kg/m^3]	85	620
Isobaric heat capacity	C_p	[J/kg.K]	3	103
Thermal conductivity	k	[W/m.K]	0.1	0.4
Dynamic viscosity	μ	[kg/m.s]	3.10^{-5}	8.10^{-5}

$$\begin{aligned}\bar{C}_p &= \frac{1}{T_w - T_{in}} \int_{T_{in}}^{T_w} C_p \, dT \\ &= \frac{h_w - h_{in}}{T_w - T_{in}}\end{aligned} \tag{3.59}$$

where h_w and h_{in} are the specific enthalpy of the fluid at wall and inlet temperature. The dimensionless variables used for the scaling procedure are:

$$\breve{z} = \frac{z}{l} \qquad \breve{u} = \frac{u}{\bar{u}} \qquad \breve{T} = \frac{T - T_{in}}{T_w - T_{in}} \qquad \breve{\rho} = \frac{p - p_0}{\bar{\rho} g l} \tag{3.60}$$

where l is the length of the heated section of the pipe and a bar denotes a system-averaged quantity. Estimations for the contribution of gravity, flow velocity or viscosity on the relative pressure in the system clearly point out that the hydrostatic pressure will be dominant. For this reason, the hydrostatic pressure has been chosen for scaling the relative pressure.

Substitution of the dimensionless variables defined by Eq. 3.60 into Eq. 3.47 and Eq. 3.58 gives:

$$\breve{u} \frac{d\breve{u}}{d\breve{z}} = -\frac{gl}{\bar{u}^2} \frac{d\breve{p}}{d\breve{z}} + \frac{\bar{\mu}}{\bar{\rho} \bar{u} l} \frac{4}{3} \frac{d^2 \breve{u}}{d\breve{z}^2} - \frac{gl}{\bar{u}^2} \tag{3.61}$$

$$\begin{aligned}\breve{u} \frac{d\breve{T}}{d\breve{z}} &= -\frac{gl}{\bar{C}_p \Delta T} \frac{T}{\rho} \left(\frac{\partial \rho}{\partial T} \right)_p \breve{u} \frac{d\breve{p}}{d\breve{z}} + \frac{\bar{\mu} \bar{u}}{\bar{\rho} \bar{C}_p \Delta T l} \frac{4}{3} \left(\frac{d\breve{u}}{d\breve{z}} \right)^2 \\ &\quad + \frac{hl}{\bar{\rho} \bar{C}_p \bar{u} D} 4 \left(1 - \breve{T} \right) + \frac{\bar{k}}{\bar{\rho} \bar{C}_p \bar{u} l} \frac{d^2 \breve{T}}{d\breve{z}^2}\end{aligned} \tag{3.62}$$

where $\Delta T \equiv T_w - T_{in}$. Using a more compact notation for the dimensionless groups:

$$\breve{u} \frac{d\breve{u}}{d\breve{z}} = -\frac{1}{Fr} \frac{d\breve{p}}{d\breve{z}} + \frac{1}{Re} \frac{4}{3} \frac{d^2 \breve{u}}{d\breve{z}^2} - \frac{1}{Fr} \tag{3.63}$$

Table 3.3: *Estimations of the dimensionless groups based on mean parameter values.*

Group	Case 1	Case 2	Case 3
$\frac{1}{\mathrm{Fr}}$	5.10^{0}	2.10^{1}	1.10^{2}
$\frac{1}{\mathrm{Re}}$	1.10^{-8}	3.10^{-8}	7.10^{-8}
$\frac{\mathrm{Br}}{\mathrm{FrPr}}$	3.10^{-5}	3.10^{-5}	3.10^{-5}
$\frac{\mathrm{Br}}{\mathrm{Pe}}$	7.10^{-14}	4.10^{-14}	1.10^{-14}
$\frac{\mathrm{Nu}}{\mathrm{Pe}_D}$	6.10^{-1}	5.10^{-1}	6.10^{-1}
$\frac{1}{\mathrm{Pe}}$	6.10^{-9}	1.10^{-8}	3.10^{-8}

$$\begin{aligned} \breve{u}\frac{d\breve{T}}{d\breve{z}} &= -\frac{Br}{FrPr}\frac{T}{\rho}\left(\frac{\partial\rho}{\partial T}\right)_p \breve{u}\frac{d\breve{p}}{d\breve{z}} + \frac{Br}{Pe}\frac{4}{3}\left(\frac{d\breve{u}}{d\breve{z}}\right)^2 \\ &\quad + \frac{Nu}{Pe_D}4\left(1-\breve{T}\right) + \frac{1}{Pe}\frac{d^2\breve{T}}{d\breve{z}^2}. \end{aligned} \tag{3.64}$$

Since the dimensionless quantities are now scaled to values between 0 and O(10), the values of the dimensionless groups indicate which terms are negligible. For the three cases considered in this study, the following values have been calculated using the mean parameter values listed in Table 3.2:

Here the heat transfer coefficient in the Nusselt number is assumed to be 15,000 W/m^2·K in case 1, 6000W/m^2·K in case 2 and 3000W/m^2·K in case 3. These values are representative according to measurement data found in Mokry et al. [84] for the pipe diameter of 10 mm. Based on the estimations presented in Table 3.3, it can be concluded that viscous effects, internal conduction and enthalpy changes due to a pressure gradient may be neglected without losing much accuracy compared to the full 1D-model equations. This results in:

$$\frac{d}{dz}(\rho u)=0 \tag{3.65}$$

$$(\rho u)_0\frac{du}{dz}+\frac{dp}{dz}=-\rho g \tag{3.66}$$

$$\frac{dT}{dz}=\frac{4}{D}\frac{h}{(\rho u)_0 C_p}(T_w-T) \tag{3.67}$$

where the second fraction on the right-hand side of Eq. 3.67 is also known as the Stanton number:

$$St=\frac{h}{\rho u C_p} \tag{3.68}$$

For numerical implementation, it is convenient to write this system of equations into the form:

$$A(\vec{y},z)\frac{d\vec{y}}{dz}=\vec{F}(\vec{y},z) \tag{3.69}$$

where $\vec{y}$ is the vector of flow variables, $A(\vec{y},z)$ is a characteristic matrix and $F(\vec{y},z)$ is a vector of source terms. When p, u and T are chosen as the flow variables, the model equations are represented by:

$$\begin{bmatrix} 0 & \frac{1}{u} & 0 \\ 1 & (\rho u)_0 & 0 \\ 0 & 0 & 1 \end{bmatrix}\frac{d}{dz}\begin{Bmatrix} p \\ u \\ T \end{Bmatrix}=\begin{Bmatrix} -\frac{1}{\rho}\frac{d\rho}{dz} \\ -\rho g \\ \frac{4}{D}\mathrm{St}(T_w-T) \end{Bmatrix} \tag{3.70}$$

Dividing by matrix A yields:

$$\frac{d}{dz}\begin{Bmatrix} p \\ u \\ T \end{Bmatrix}=\begin{bmatrix} -u(\rho u)_0 & 1 & 0 \\ u & 0 & 0 \\ 0 & 0 & 1 \end{bmatrix}\begin{Bmatrix} -\frac{1}{\rho}\frac{d\rho}{dz} \\ -\rho g \\ \frac{4}{D}\mathrm{St}(T_w-T) \end{Bmatrix} \tag{3.71}$$

Table 3.4: *A selection of Nusselt correlations for heated, aiding pipe flow at supercritical pressures and their parameter ranges.*

Authors	**p** [MPa]	**G** [kg/m^{2}s]	**Q** [kW/m^2]	**D** [mm]	**T$_b$** [°C]
Swenson et al. [107]	23-41	542-2150	200-2000	9.4	75-576
Yamagata et al. [133]	23-29	310-1830	120-930	7.5, 10	230-540
Mokry et al. [83]	24	200-1500	$\leq$ 1250	10	320-406

This system of equations has been solved explicitly for the pressure, axial velocity and temperature using an Euler scheme.

3.2.3 Nusselt correlations

Quite a number of Nusselt correlations have been developed for supercritical heat transfer in pipe flows. Most of these empirical correlations have the general form of a modified Dittus-Boelter equation [139]:

$$Nu_x = C \cdot Re_x^n \cdot Pr_x^m \cdot F_c \tag{3.72}$$

where x is an indicator for the temperature which is used to calculate the fluid properties, C is a constant and F_c is a correction factor that accounts for property variations or entrance effects. A selection of Nusselt correlations found in literature that may be suitable for predicting the heat transfer coefficient in this study is given in Table 3.4.

Correlation of Swenson et al.

The correlation of Swenson et al. [107] has been derived from experimental data of upward supercritical water flows. It evaluates the majority of fluid properties at wall temperature:

$$Nu_w = 0.00459 \cdot Re_w^{0.923} \cdot Pr_w^{0.613} \left(\frac{\bar{C}_p}{C_{p,b}} \right)^{0.613} \left(\frac{\rho_w}{\rho_b} \right)^{0.231} \tag{3.73}$$

Correlation of Yamagata et al.

Yamagata et al. [133] conducted experiments on horizontal and vertical supercritical water flows. The most extensive data were obtained for the vertically upward flow in a 10 mm tube. After excluding the measurements obtained in the region of deteriorated heat transfer, mainly these data were used to derive the proposed correlation:

$$Nu_b = 0.0135 \cdot Re_b^{0.85} \cdot Pr_b^{0.8} \cdot F. \tag{3.74}$$

Here the definition of the correction factor F depends on the Eckert number E as follows:

$$F = \begin{cases} 1.0 & \text{for } E > 1 \\ 0.67 \cdot Pr_{pc}^{-0.05} \left(\frac{\bar{C}_p}{C_{p,b}} \right)^{n_1} & \text{for } 0 \le E \le 1 \\ \left(\frac{\bar{C}_p}{C_{p,b}} \right)^{n_2} & \text{for } E < 0 \end{cases} \tag{3.75}$$

with the Eckert number defined as:

$$E = \frac{T_{pc} - T_b}{T_w - T_b} \tag{3.76}$$

and the coefficients n_1 and n_2 given by:

$$n_1 = -0.77 \cdot \left(1 + \frac{1}{Pr_{pc}} \right) + 1.49 \qquad n_2 = 1.44 \cdot \left(1 + \frac{1}{Pr_{pc}} \right) - 0.53 \tag{3.77}$$

Mokry et al.

Mokry et al. [83] derived a correlation on basis of measurements conducted at the supercritical test facility of the Institute for Physics and Power Engineering in Obninsk, Russia. The experimental data were collected from supercritical water flows in 10 mm pipes and have led to the following expression for the Nusselt number:

$$Nu_b = 0.0061 \cdot Re_b^{0.904} \cdot \overline{Pr_b}^{0.684} \left(\frac{\rho_w}{\rho_b}\right)^{0.564} \tag{3.78}$$

where the average Prandtl number $\overline{Pr_b}$ is calculated using the mean isobaric heat capacity $\bar{C}_p$ as defined in Eq. 3.59.

3.2.4 Boundary conditions

The 1D heat transfer model requires inlet conditions to calculate further towards the end of the tube. In addition, the wall temperature is needed as a boundary condition. The inlet and boundary conditions are set as listed in Table 3.1. These conditions are in agreement with the conditions that were selected for measurements in supercritical water found in Mokry et al. [84], which enables validation of the simulation results. The experimental data includes measurements of the inner wall temperature for a heated upflow of water using uniform wall heat flux. The inner wall temperature data has been adopted as the wall condition for the simulations.

On basis of the validity ranges shown in Table 3.4, the Nusselt correlations of Swenson et al., Yamagata et al. and Mokry et al. have been selected to prescribe the local heat transfer from the wall to the fluid. These three correlations result in three temperature profiles for each of the considered mass fluxes.

Since the density gradient in the elements, $d\rho/dz$ in Eq. 3.71, is calculated using backward differences, this gradient is assumed to be zero for the first element to avoid numerical errors.

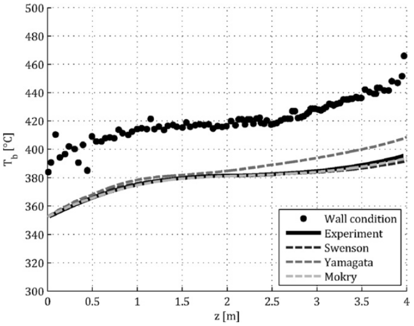

Figure 3.12: *Temperature as function of the tube height for G = 1000 kg/m^2 s using different Nusselt correlations.*

3.3 Results and validation

The 1D heat transfer model presented in this article has been used to predict the bulk-fluid temperature for the cases shown in Table 3.1. Temperature predictions using the correlations of Swenson et al., Yamagata et al. and Mokry et al. have been compared to experimental data found in Mokry et al. [84]. The experimental temperature profiles were constructed by measuring the bulk-fluid temperature at the inlet and outlet and then calculating the profiles using a simple heat balance (I.L. Pioro, personal communication, December 14, 2011).

The calculated fluid temperature profiles for a mass flux of 1000 kg/m^2 s are shown in Fig. 3.12 together with the experimental data. This case fits well within the ranges of validity listed in Table 3.4. The slope of the temperature profile decreases while approaching the pseudo-critical point at 381°C. The phase change requires a lot of energy due to the high heat capacity in the vicinity of this point, causing the temperature increase to slow down. Once the fluid temperature has passed the pseudo-critical point, the slope of the lines tends to restore. When the bulk temperature is raised further, the rate of heat transfer is expected to decline since the driving force will decrease. The decrease is not visible in the results, however, which indicates that the heat transfer may still be governed by other effects like for example boiling effects.

The best match with the measurements is obtained when using the correlation of Mokry et al. or Swenson et al. The excellent agreement in temperature profiles demonstrates that, in case a suitable Nusselt correlation is available, the model is capable of accurately calculating the fluid temperature from wall temperature data at supercritical conditions. The correlation of Yamagata results in a good match up to the region where the fluid reaches pseudocritical conditions. From this point, the rate of heat transfer and hence temperature is overpredicted. Apparently, the large hump in the heat flux around the pseudo critical point seen in Fig. 3.13 is not realistic for this case.

The graphs illustrate that not all correlations give similar results, despite of the fact that they should all be applicable for this case. Therefore, selecting the right correlation solely based on the parameters considered in Table 3.4 may not be adequate. In order to study the sensitivity of the selected Nusselt correlations to the mass flux, a second and third case have been simulated using a mass flux of 500 and 200 kg/m^{2}s, respectively. The results are shown in Fig. 3.14 and 3.15, together with the experimental data for this particular mass flux.

Figs. 3.14 and 3.15 show that the correlations of Mokry et al. and Swenson et al. give accurate predictions of the bulk temperature for these mass fluxes as

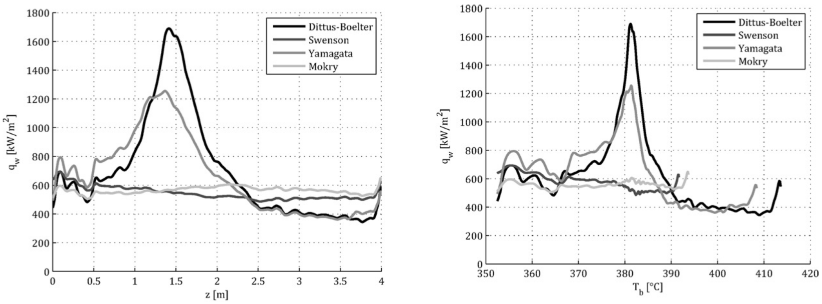

(a) Heat flux as a function of tube height.

(b) Heat flux as a function of bulk temperature.

Figure 3.13: *Wall heat flux as function of the tube height (a) and bulk temperature (b) for G = 1000 kg/m^{2}s using different Nusselt correlations.*

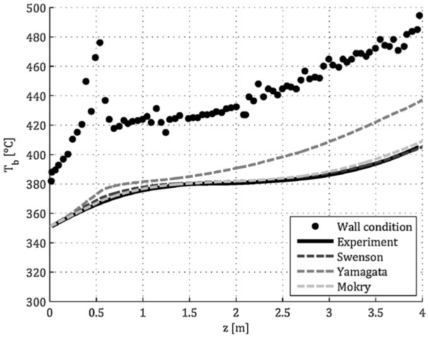

Figure 3.14: *Temperature as function of the tube height for G = 500 kg/m^2 s using different Nusselt correlations.*

well. The results based on the correlation of Yamagata et al. are however worse compared to the results in Fig. 3.12.

Fig. 3.16 points out that the heat flux for G = 200 kg/m^{2}s is again over predicted in a broad range around the pseudo critical temperature. The heat flux graphs for G = 500 kg/m^{2}s are similar, but have been omitted here to save space. Clearly, the correlation of Yamagata et al. is outperformed by the correlation of Swenson et al., even though the validity range of the latter does not

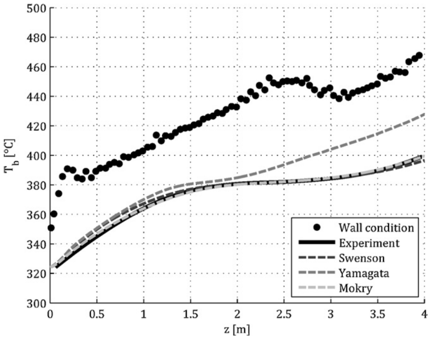

Figure 3.15: *Temperature as function of the tube height for G = 200 kg/m^2 s using different Nusselt correlations.*

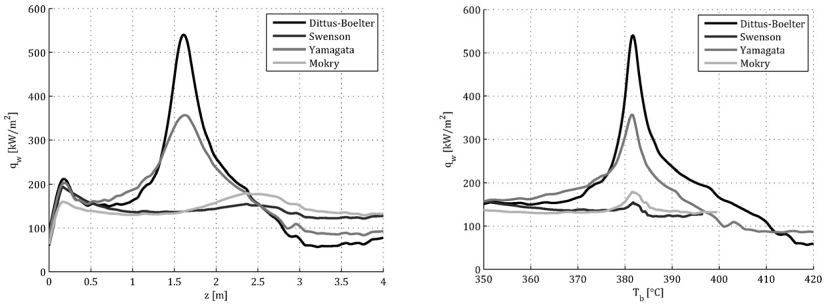

(a) Heat flux as a function of tube height.

(b) Heat flux as a function of bulk temperature.

Figure 3.16: *Wall heat flux as function of the tube height (a) and bulk temperature (b) for* $G = 200$ *kg/m*^{2}*s using different Nusselt correlations.*

include these low mass fluxes.

3.4 Extension to chemically reacting flow for qualitative analysis

The 1D-model discussed in Section 3.2 can be used to study heat transfer in supercritical water flows. In order to perform calculations on the reacting flow in a supercritical gasifier, the model has to be extended with equations and properties describing chemistry and mass transfer. This procedure is treated in the following sections.

The chemical reaction that is used to model the complex chemistry of biomass conversion is described in Section 3.4.1. The next sections deals with the extension of the conservation equations. Estimation of the thermo-physical properties of the reacting mixture and the diffusion coefficients are discussed in Section 3.4.3 and Section 3.4.4. The simulations of reacting flow are conducted with an initial mass fraction of 10 wt% methanol. The results of the reacting flow simulations are compared with the results for non-reacting flow in Section 3.4.5.

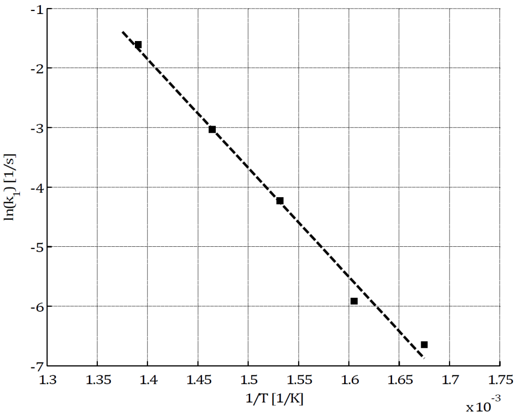

Figure 3.17: *Arrhenius plot for the methanol decomposition rate in supercritical water using the experimental data of Hack et al. [44].*

3.4.1 Modeling the chemistry of biomass conversion in supercritical water

Conversion of biomass in supercritical water is a rather complex chemical process involving a large number of intermediates and reaction steps. Since a detailed description of the chemistry would go beyond the scope of this study, methanol decomposition is chosen as a simple reaction that may be representative for the endothermic gasification process. Decomposition of methanol into carbon monoxide and hydrogen is described by the following reaction [22]:

$$CH_3OH \rightarrow CO + 2H_2 \tag{3.79}$$

where the enthalpy of reaction ΔH_r is reported to be 91.7 kJ/mol at 298 K.

The reaction rate as a function of temperature is described by the Arrhenius expression given by:

$$k = Ae^{\frac{-Ea}{RT}} \tag{3.80}$$

where A is the pre-exponential factor, E_a the activation energy and R the universal gas constant. The pre-exponential factor and activation energy characterizing the specific reaction shown above are difficult to find considering the fact that it is only one of the three independent overall reactions of methanol reforming in supercritical water. Methanol decomposition in supercritical water was studied in a Hastelloy tube flow reactor by Hack et al. [44] in the temperature range $597 < T < 797$ K at a pressure of 315 bar. Although the reaction mechanism is clearly not fully described by Eq. 3.79, the decomposition rate constants presented in the article are adopted for the simple reaction used in this study. The measured rate constants are plotted in an Arrhenius plot in Fig. 3.17, where $\ln(k_1)$ and $1/T$ are related according to the logarithm of the Arrhenius equation:

$$\ln(k_1)=\ln(A)-\frac{E_a}{R}\frac{1}{T}. \tag{3.81}$$

The linear fit with a slope of -18268 K/s and a y-intercept at 23.724 1/s implies the pre-exponential factor is $2.0 \cdot 10^{10}$ 1/s and the activation energy is 152 kJ/mol.

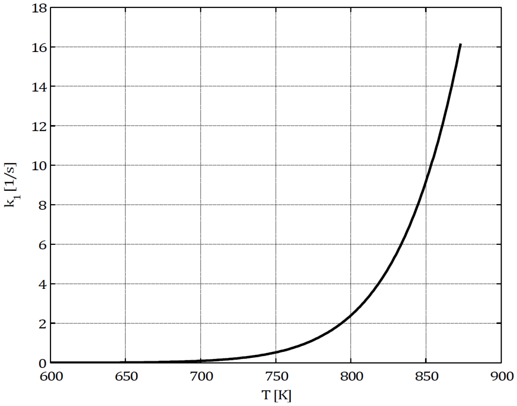

Figure 3.18: *Reaction rate as function of temperature for methanol decomposition, according to Hack et al. [44].*

The reaction rate for methanol decomposition is plotted against temperature in Fig. 3.18, showing that the reaction starts at approximately 700 K.

3.4.2 Extension of the 1D-model equations

The 1D-model equations must be extended with equations describing conservation of species and a heat sink term accounting for the heat that is consumed by the endothermic reaction. Adding the heat sink term to the heat equation, Eq. 3.58 becomes:

$$\frac{dT}{dz}=\frac{4}{D}\frac{h}{(\rho u)_0 C_p}(T_w-T)+\frac{\Delta H_r}{(\rho u)_0 C_p}\frac{r_{MeOH}}{M_{MeOH}} \tag{3.82}$$

where ΔH_r is the enthalpy of reaction and r_{MeOH} is the reaction rate for methanol, according to Eqs. 3.10 and 3.11:

$$r_{MeOH}=Ae^{\frac{Ea}{RT}}\cdot\rho\cdot y_{MeOH}. \tag{3.83}$$

The equation for conservation of species for the 1D-model is derived from Eq. 3.6 by neglecting the time dependent and diffusion term and therefore reads:

$$\frac{dy_i}{dz}=\frac{1}{(\rho u)_0}r_i \tag{3.84}$$

where r_i are the reaction rates for the different species. The reaction rate for methanol is given by Eq. 3.83 and the reaction rates for carbon monoxide and hydrogen easily calculated using:

$$r_{MeOH}=-r_{CO}=-2\cdot r_{H_2}. \tag{3.85}$$

3.4.3 Estimation of the mixture properties

With chemistry included in the model according to the sections above, the fluid inside the pipe is a mixture of water, methanol, carbon monoxide and hydrogen. The fluid is modeled as a single phase with mixture properties that have to be estimated based on the flow conditions and the local composition. This section deals with the estimation of the mixture properties that are inserted into the numerical models and the properties of the individual species that are used in the mixing rules.

The average molar mass of the mixture is determined from the individual mass factions and molar masses according to the following mixing rule:

$$M = \left[\sum_{i=1}^{N} \frac{y_i}{M_i} \right]^{-1} \tag{3.86}$$

Similarly, the density of the mixture is calculated using:

$$\rho = \left[\sum_{i=1}^{N} \frac{y_i}{\rho_i} \right]^{-1} \tag{3.87}$$

For water, the density is given by the IAPWS-IF97 formulation, described in Section 3.1.2. Density data for the other species at 300 bar has been obtained

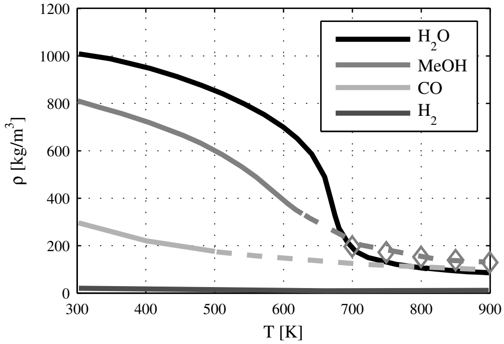

Figure 3.19: *Density data for the different species, where the solid lines represent database values and the intermittent lines represent estimated densities. The diamonds indicate calculated values using the Peng-Robinson equation of state.*

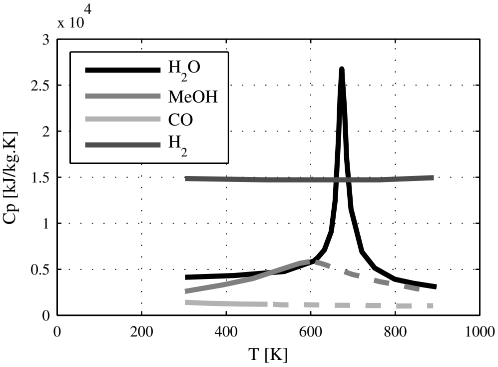

Figure 3.20: *Heat capacity data for the different species, where the solid lines represent database values and the intermittent lines represent estimated values.*

from the database of the National Institute of Standards and Technology [74]. The NIST database provides data for hydrogen at all required temperatures but is limited to 500 K for carbon monoxide and 620 K for methanol, which means that the density at higher temperatures must be estimated for these species.

As carbon monoxide at 620 K is far beyond its pseudo critical temperature, the density is estimated using extrapolation. This not the case for methanol, so additional data points at high temperatures are required to make a reasonable estimation. Since no information on the density at this pressure and temperature range was encountered in literature, the Peng-Robinson equation of state [92] has been used to provide the missing datapoints. The Peng-Robinson values are well described by an exponential curve that has been fitted such that it connects to the last datapoint of the NIST database.

The density profiles of all species are plotted in Fig. 3.19, where the solid lines represent data obtained from the IAPWS-IF97 formulation or NIST database and the intermittent lines represents estimated data. The triangles indicate the density values calculated using the Peng-Robinson equation of state.

The isobaric heat capacity of the mixture is estimated using the following mixing rule:

$$C_p = \sum_{i=1}^{N} y_i C_{p,i} \tag{3.88}$$

The heat capacities for the individual species are plotted as a function of temperature in Fig. 3.20. The solid lines represent data given by the IAPWS-IF97 formulation or found in the NIST database, the intermittent lines show extrapolated data. Heat capacity data for methanol is mirrored in the line T = 600 K, where the curve reaches its maximum value. This approach is believed to give a good approximation considering the symmetry in the heat capacity curves for supercritical methanol found in literature [4].

The mixture-averaged thermal conductivity is calculated from a relation presented in Warnatz et al. [120]:

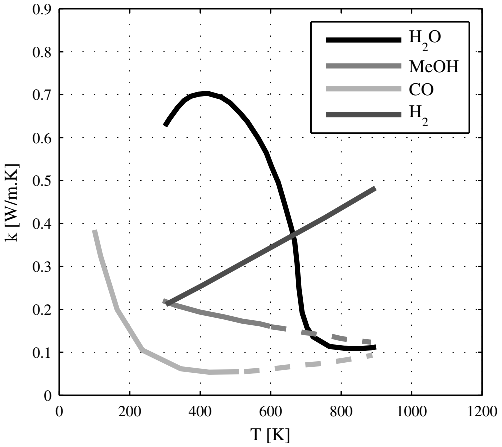

Figure 3.21: *Thermal conductivity of the different species, where the solid lines represent database values and the intermittent lines represent extrapolated values.*

$$k = \frac{1}{2}\left[\sum_{i=1}^{N} x_i k_i + \left(\sum_{i=1}^{N} \frac{x_i}{k_i}\right)^{-1}\right] \tag{3.89}$$

For gas mixtures this equation has an accuracy of some 10-20%, which is considered satisfactory for this study. The thermal conductivity for the different species is plotted in Fig. 3.21. The solid lines represent data given by the IAPWS-IF97 formulation or found in the NIST database, the intermittent lines show extrapolated data.

Estimation of the viscosity of a mixture is considered to be a challenge in literature. Viscosities are rarely additive, and the relation between viscosity and concentration can be very nonlinear [104]. Although some correlations for mixture viscosities are available, they are found to be quite specific and often too complex for fast implementation. First, there is a division of correlations for liquid mixtures and gas mixtures. For the gas mixture estimation methods, a subdivision into high-pressure and low-pressure mixtures is required to choose the correct correlation. Finally, there is a distinction between polar and non-polar mixtures. The fluid in the gasification reactor model will be a mixture of supercritical methanol gas and liquid water at the inlet, and a dense gas mixture at the outlet. A short discussion of some of the suggested correlations

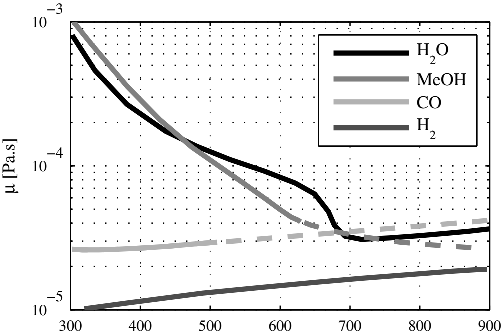

Figure 3.22: *Viscosity of the individual species at 300 bar. The dashed lines indicate estimated values.*

in literature is given below.

When the fluid temperature is between inlet temperature and the pseudo-critical temperature of water at 300 bar, it is in fact a solution of supercritical gases (mainly methanol) in liquid water. A practical mixing rule for the viscosity of a gas-liquid mixtures was not found in literature. According to Reid et al. [98], essentially all correlations for liquid mixture viscosity refer to solutions of liquids below or only slightly above their normal boiling points. More recent publications [114], present no useful correlation for a solution of gases in a liquid.

At temperatures above the pseudo-critical point of water, the fluid can be considered as a (dense) mixture of gases. For high-pressure gas mixtures, the estimation methods of Lucas or Chung et al. can be used [98]. These methods give estimations with an absolute average deviations of 8 to 9 percent for both polar and non-polar mixtures. Nevertheless, they consist of a sets of equations that are unattractive to use for a quick estimation. The much less complex semi-empirical method of Wilke, developed on basis of the kinetic theory approach, has been extensively tested and proved to be quite reliable, but is only valid for low-pressure gas mixtures. A somewhat less accurate, though even more practical method for low-pressures is provided by Herning and Zipperer [25]. In principle, the gaseous mixture viscosity at high pressure may be estimated by using one of these two low-pressure methods when compensated after wards for the pressure. The pressure correction factor can be obtained from a generalized graph used for pure substances based on the reduced temperature. In this case, however, it is not quite obvious that a calculation corrected with a pressure factor of an estimated low-pressure gas mixture viscosity yields more accurate values than a mixing rule that is analogous to Eq. 3.89:

$$\mu = \frac{1}{2}\left[\sum_{i=1}^{N} x_i \mu_i + \left(\sum_{i=1}^{N} \frac{x_i}{\mu_i}\right)^{-1}\right] \tag{3.90}$$

This equation can be used to estimate the mixture viscosity with an accuracy of around 10% [120].

In order to make an estimation using Eq. 3.90, it is required that the viscosities of the individual species are known. Viscosity data for a pressure of 300 bar

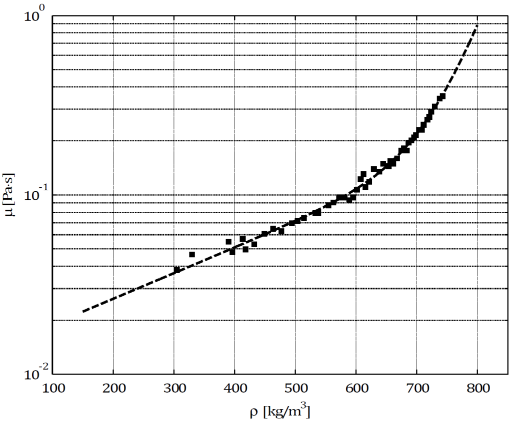

Figure 3.23: *Viscosity of methanol as function of density as found in Xiang et al. [128]. The line represents an exponential curve fit.*

and temperatures from 300 to 900 K is shown in Fig. 3.22.

Viscosity data for water is obtained from the IAPWS-IF97 formulation. The solid lines for hydrogen and carbon monoxide represent viscosity data from the NIST database. Extrapolation of viscosity data in the temperature range 300 to 500 K gives the dotted line for carbon monoxide. The viscosity line for methanol has been constructed using experimental data from Yergovich et al. [135] and Golubev and Likhachev [128]. These data was graphically presented as a function of density by Xiang et al. [128]. An exponential fitting curve is used to obtain an expression for the viscosity as function of the density, which is shown together with the experimental data in Fig. 3.23.

Combining the density-temperature relation plotted in Fig. 3.19 with the viscosity-density relation shown in Fig. 3.23 yields the viscosity curve for methanol in Fig. 3.22, where the dotted line section above 620 K indicates that the Peng-Robinson equation has been used to estimate the density.

3.4.4 Estimation of the diffusion coefficients

For a proper prediction of diffusive transport, it is important to make a good estimation of the diffusion coefficient. Since the required coefficients at supercritical conditions have not been found in literature, empirical correlations are employed to make a good guess. An estimation for the diffusion in the liquid phase can be obtained by using the Wilke-Chang method for binary liquid diffusion coefficients at infinite dilution [98]:

$$D^0_{AB} = \frac{7.4 \cdot 10^{-8} (\phi M_B)^{1/2} T}{\mu_B V_A^{0.6}} \tag{3.91}$$

where D^o_A B is the mutual diffusion coefficient of solute A at very low concentrations in solvent B, V_A is the molar volume of solute A at its normal boiling point temperature and ϕ is the association factor of solvent B, given as 2.6 for water. The molar volume of the four species in the reactor mixture can be found in Bretsznajder [25] and are listed in Table 3.5.

Table 3.5: *Molar volumes at the species normal boiling point.*

Component	**V_A [cm^3 / mol]**
H_2O	18.9
CH_3OH	42.5
CO	30.7
H_2	14.3

Eq. 3.91 is suitable for liquid-liquid systems with concentrations of A up to 5 and perhaps 10 mole percent. It is however assumed that the correlation also provides a representative diffusion coefficient for solutions of supercritical methanol in liquid water up to 10 mass percent.

At temperatures at the pseudo-critical point and higher, where water behaves more like a gas, the diffusion coefficient can be approximated using the correlation of Takahashi for estimating binary diffusion coefficients of gases at high pressures [98]:

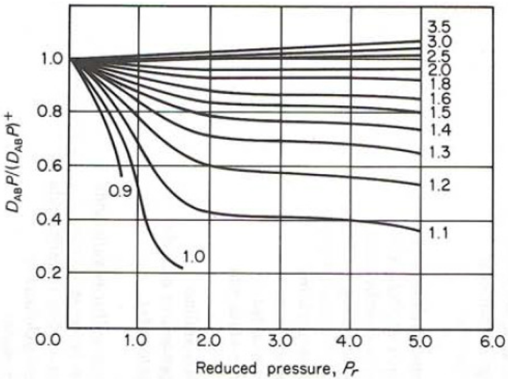

Figure 3.24: *Takahashi correlation for the effect of pressure and temperature on the binary diffusion coefficient of gases [98].*

$$\frac{pD_{AB}}{(pD_{AB})^+} = f(T_r, p_r) \tag{3.92}$$

Here D_{AB} is the mutual diffusion coefficient and $f(T_r, p_r)$ is a function of the reduced temperature and pressure, which are defined as follows:

$$T_r = \frac{T}{T_c} \tag{3.93}$$

$$T_c = x_A T_{c,A} + x_B T_{c,B} \tag{3.94}$$

$$p_r = \frac{p}{p_c} \tag{3.95}$$

$$p_c = x_A p_{c,A} + x_B p_{c,B}. \tag{3.96}$$

The function value at different reduced temperatures and pressures is then obtained from Fig. 3.24.

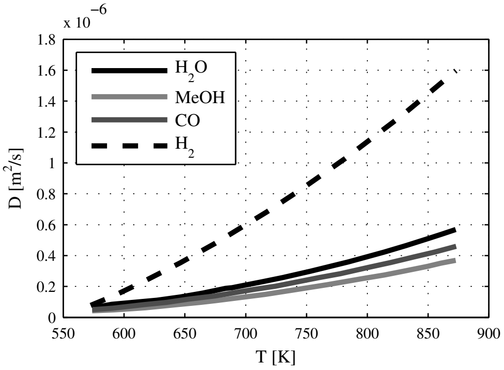

Figure 3.25: *Estimated mixture-averaged diffusion coefficients for the different species. The lines are quadratic polynomial curve fits.*

The superscript $^+$ indicates that low-pressure values are to be used. The low-pressure binary diffusion coefficient is calculated using the Fuller method [98]:

$$D_{AB} = \frac{0.00143\,T^{1.75}}{p M_{AB}^{1/2} \left[(\sum_v)_A^{1/3} + (\sum_v)_B^{1/3} \right]^2} \tag{3.97}$$

where $\sum_v$ is found for each component by summing the atomic diffusion volumes, and M_{AB} is defined as:

$$M_{AB} = 2[(1/M_A) + (1/M_B)]^{-1} \tag{3.98}$$

Table 3.6: *Sum of atomic diffusion volumes [98].*

Component	**Atomic diffusion volumes**
H_2O	13.1
CH_3OH	31.3
CO	18.0
H_2	6.12

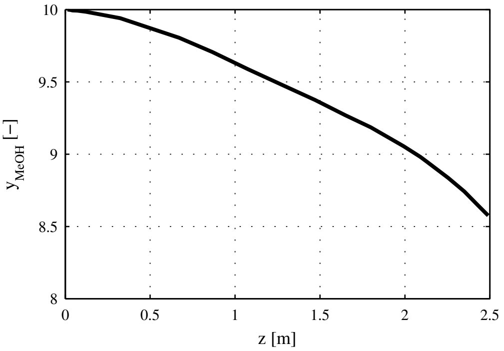

Figure 3.26: *Mass fraction of methanol as function of the pipe height using the Nusselt correlation of Mokry et al. [83].*

The sums for the components involved in the SCWG simulations are given in Table 3.6.

In the calculations p^+ is chosen to be 1 bar. When the effect of solute A on the critical temperature and pressure in Eqs. 3.94 and 3.96 are neglected and pure water is assumed as the solvent B, the coefficients for binary and self-diffusion are as shown in Fig. 3.25. The solid lines are quadratic polynomial curves that are fitted to the estimated diffusivities at inlet temperature (573 K), pseudocritical temperature (675 K) and wall temperature (873 K).

3.4.5 1D simulation results

Fig. 3.26 shows the mass fraction of methanol as calculated with the 1D-model. The initial concentration is set to 10 wt% and the heat transfer coefficient is predicted by the Nusselt correlation of Mokry et al. [83]. For the case simulated in this section the wall temperature is choosen constant over the complete length of the tube, this was not the case in Section 3.3. The rate of conversion is rather low up to $z = 2$ m, where the fluid temperature passes 700 K, as can be seen in Fig. 3.27. It can be seen in Fig. 3.18 that the reaction rate for methanol decomposition starts to increase rapidly at this temperature.

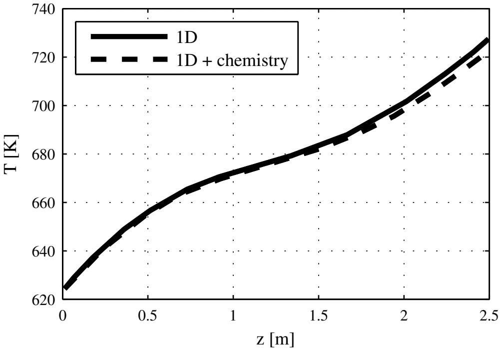

Figure 3.27: *Temperature as function of the pipe height for reacting and non-reacting flow. The results are based on the Nusselt correlation of Mokry et al. [83].*

The effect of the chemical reaction on the temperature field is illustrated in Fig. 3.27. The figure shows only little difference between the temperature results of the reacting and non-reacting flow simulations. As the decomposition reaction is endothermic, a slight decrease in temperature is observed compared to the non-reaction flow.

3.5 Discussion

The large deviation between results based on the correlation of Yamagata et al. and results based on the other two correlations may be explained by considering boiling effects. According to the theory of heat transfer at supercritical pressures (Section 3.1), pseudo-film boiling can highly influence heat transfer at supercritical pressures depending on the flow conditions. A combination of several parameters including tube diameter, pressure, mass flux and heat flux determines which heat transfer regimes will occur inside the tube (i.e. normal, improved or deteriorated heat transfer).

For the cases considered in this study, the heat flux seems to exceed or approach the critical value indicated by Fig. 3.4. Therefore, it can be expected that peaks in the heat flux around the pseudo-critical point are lower, flattened or do not occur at all. In contrast to the other two correlations considered in this study, the correlation of Yamagata et al. was derived from experimental data from which measurements obtained in the region of deteriorated heat transfer were excluded [133]. This is a possible reason why the heat flux predicted by Yamagata et al. is incorrect for the cases considered in this article. In cases where deterioration of heat transfer does not occur, the correlation might show better accuracy.

The influence of buoyancy forces can be estimated by calculating the criterion of Aicher and Martin (Eq. 3.36). In Case 3, the value of this criterion mainly varies between 0.05 and 0.2 over the first half of the tube. According to Fig. 3.5, the flow in this region should hence be classified as aided mixed convective flow, for which the Nusselt number is significantly lower compared to pure forced convection. Here, both buoyancy forces and pseudo-film boiling could have been responsible for the low heat transfer rates. However, heat transfer rates in Case 1 are also much lower than predicted by the Dittus-Boelter equation, whereas this case should be classified as (nearly) pure forced convection over the entire tube length. With values lower than 0.08 for the criterion, buoyancy forces are probably not the cause for the low heat transfer rates in this case. In Case 2, only a small region of mixed convective flow is observed near the inlet, which cannot explain the decreased heat transfer rate over a large part of the tube.

Assuming that boiling effects are the main reason for the large differences between the predictions observed in Section 3.3, it is important to know on beforehand if the critical heat flux will be exceeded when selecting a Nusselt correlation for the 1D-model. An estimation for the critical heat flux can be made using the criteria proposed by Yamagata et al., Eq. 3.34, or by Mokry et al., Eq. 3.35. However, it should be noted that there is still no unique definition for the onset of heat transfer deterioration, because this phenomenon behaves rather smoothly [30].

The sensitivity of the results for other parameters than mass flux has not been studied by the authors. In order to study the influence of boiling effects for this tube geometry in more detail, a two-dimensional model has been developed and will be presented in the next chapter.

3.6 Conclusions

Based on a literature study, it can be concluded that the property variations of water in the vicinity the (pseudo)critical point significantly influence the heat transfer. Depending on the flow conditions, the variations in fluid properties can result in heat transfer enhancement or deterioration. In literature, these effects have been related to boiling phenomena and to acceleration of the fluid due to buoyancy forces. Acceleration of the fluid near the boundary layer is assumed to influence the turbulent diffusivity in the region where turbulence plays an important role in the heat transfer.

In this work, heat transfer to supercritical water has been modeled in a one-dimensional domain by using a plug flow approach. Viscous effects, internal conduction and enthalpy changes due to a pressure gradient have been neglected after evaluation of the governing equations in dimensionless form. Nusselt correlations are required for predicting the heat transfer coefficient in order to close the set of equations.

The results of the simulations for three different cases show that the model is able to accurately predict the bulk temperature based on heat transfer rates provided by a suitable Nusselt correlation. However, the results also give reason to assume that the correlations are very specific for the flow conditions of the experiments from which the Nusselt correlations were derived. Different correlations that are all valid for the selected operating conditions do not necessarily give the same result.

The effect of the chemical reaction on the temperature field is also presented in this chapter. The effect of the chemical reaction on the temperature shows only little difference between the temperature results of the reacting and non-reacting flow simulations. As the decomposition reaction is endothermic, a slight decrease in temperature is observed compared to the non-reacting flow.

The large deviation between the predictive capability of the correlations suggests that it is important to consider boiling effects that occur when a critical heat flux is reached. Although the agreement with a 2D-simulation is yet to be investigated in a subsequent chapter, it can be said that the accuracy of the correlation for the simulated case will be crucial for the quality of the 1D-model.

4

2D heat transfer model of a flow reactor with supercritical water

Heat transfer to water at supercritical pressures has been numerically investigated using a two-dimensional modeling approach. The simulations in a two-dimensional domain have been performed using the low-Reynolds k-ϵ turbulence model, and the IAPWS-IF97 formulation to describe the properties of water at different conditions. The accuracy of the 2D-model is validated using an experimental setup at supercritical conditions. The comparison of the temperature results show a good agreement between the experimental data and the numerical data. Simulation results of the two-dimensional model are compared with several frequently used one-dimensional correlations from literature for heat transfer at supercritical conditions.

The work in this chapter has been published in revised form as:
J.A.M. Withag, J.L.H.P. Sallevelt, D.W.F. Brilman, E.A. Bramer, G. Brem, Heat transfer characteristics of supercritical water in a tube: Application for 2D and an experimental validation, Elsevier **70** *(2012).*[126]

4.1 Introduction

Water is in the supercritical state when both the pressure and the temperature are higher than the critical pressure and critical temperature ($P_{cr} = 22.064$ MPa and $T_{cr} = 373.95$°C). The physical properties of supercritical water strongly differ from liquid water or steam. Supercritical water has much lower values for the dielectric constant, the viscosity, the thermal conductivity and in the vicinity of the critical point a large peak in the specific heat capacity can be detected [59, 80].

Supercritical water is of great interest for several applications such as supercritical water gasification or supercritical water cooled-nuclear reactors. Supercritical water gasification is a challenging thermo-chemical conversion route for wet biomass and waste streams into valuable product gases, rich in either hydrogen or methane. Whereas supercritical water cooled reactors use the thermal properties of supercritical water to increase the thermal efficiency. Both application fields want to use the unique properties of supercritical water in order to optimize the process. For this purpose good prediction methods for the transport phenomena present in the reactor or heat exchanger are of great importance.

To predict the properties of water at different conditions the IAPWS-IF97 formulation [117] is used in this research. The IAPWS-IF97 formulation consists of a set of equations from which thermo-physical properties such as specific volume, enthalpy, thermal conductivity, viscosity and heat capacity can be derived. A detailed description of the IAPWS-I97 formulation can be found in the work of Sallevelt et al. [99] and the work of Wagner et al. [117].

Sallevelt et al. [99] describe a one-dimensional heat transfer model to simulate a supercritical water flow in a tube. With the use of the one-dimensional model various Nusselt correlations found in literature describing the heat transfer are compared. The results for the different Nusselt correlations show large deviations, which indicates that the used correlations have only limited applicability. Therefore in this work a 2D-simulation is developed to investigate the influence of two-dimensional effects on the flow and heat transfer in supercritical water.

In the present study a two-dimensional model has been developed using the low-Reynolds k-ϵ turbulence model and the IAPWS-IF97 formulation. Fur-

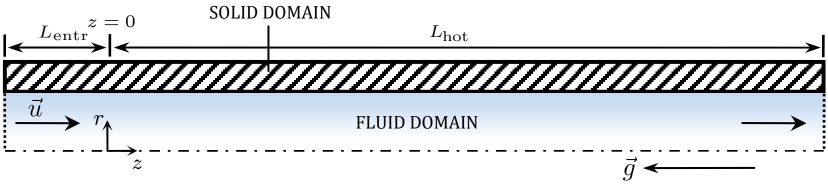

Figure 4.1: *Computational domain for the 2D-model.*

thermore, an experimental setup has been built to measure the heat transfer in supercritical water. Model results have been validated against experimental data for different mass fluxes. Finally, a comparison with the one-dimensional simulation results as obtained by Sallevelt et al. [99] is made to investigate the loss of accuracy due to the numerous sim-plifications made for the one-dimensional model. The calculations under investigation in this research have been performed using the software package COMSOL Multiphysics, which provides an advanced solver that is able to handle the two-dimensional model equations.

4.2 Computational domain

Assuming the problem is axi-symmetric around the centerline of the pipe, the entire pipe flow is covered by choosing half a cross-section as the computational domain. The computational domain includes the pipe wall and is shown in Fig. 4.1, drawn horizontally for a compact view. The heated section of the pipe L_{hot} is preceded by an entrance section L_{entr} with a length of 0.1 m for development of the hydrodynamic boundary layer.

The domains are meshed using second order Lagrange elements. The fluid domain is covered by a structured grid of quadrilateral elements, while triangular elements are used for the solid domain in order to achieve a fast transition to a coarse mesh. A boundary layer mesh consisting of slender quadrilaterals is added to the fluid domain to cope with the high gradients in the boundary layer. A mesh convergence study is carried out to check whether the mesh satisfactorily balances accuracy and computing resources.

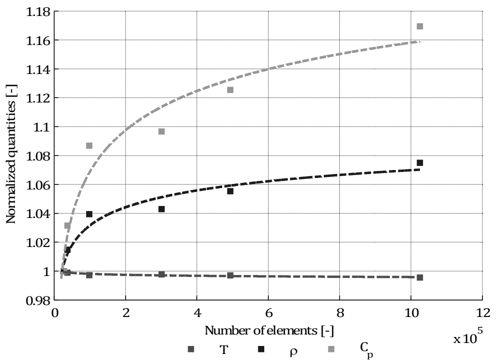

Figure 4.2: *Mesh convergence for the 2D-model on basis of normalized, surface-averaged quantities at the outlet. The data points shown correspond to gridsizes of 0.5, 0.4, 0.2, 0.1, 0.075 and 0.05 mm.*

Data for the convergence analysis has been generated by simulating a case at 240 bar, a wall temperature of 600°C and a mass flux of 20 $kg/m^2 \cdot s$. This is done in a tube with an inner diameter of 10 mm using the gridsizes shown in Table 4.1.

The surface-averaged density, temperature and isobaric heat capacity at the outlet are chosen as indicators for the mesh convergence. The results have been normalized and plotted in Fig. 4.2 together with a quadratic curve fit.

Table 4.1: *Gridsizes and corresponding total number of elements used for the 2D-mesh convergence analysis.*

Gridsize	**Number of elements** [-]
0.5	27,530
0.4	37,660
0.2	98,692
0.1	300,964
0.075	494,038
0.05	1,025,210

Although the convergence analysis calls for one of the finest meshes, a gridsize of 0.2 mm was adopted for the full pipe length of 2.5 m because a finer mesh would require more memory resources than available. Fig. 4.2 shows that the calculated heat capacity at the outlet is still significantly affected by the gridsize at this point. However, more important is the convergence of the density and temperature, which is acceptable for the chosen gridsize. The practical limitation of the number of elements will for this reason not necessarily lead to inaccurate results.

By choosing 0.2 mm as the element size for the structured mesh covering the fluid domain, the complete mesh consists of 700,717 elements (585,000 quadrilateral and 115,717 triangular). To give an impression, this mesh is shown in Fig. 4.3 for a length of 10 mm.

4.3 2D model equations

This section describes the derivation of the model equations for steady, compressible, two-dimensional flow from the governing equations given in Section 3.1.1. For this type of flow, the continuity equation is obtained by neglecting the time-dependent term in Eq. 3.1.1, which results in:

$$\vec{\nabla}\cdot(\rho\vec{u})=0. \tag{4.1}$$

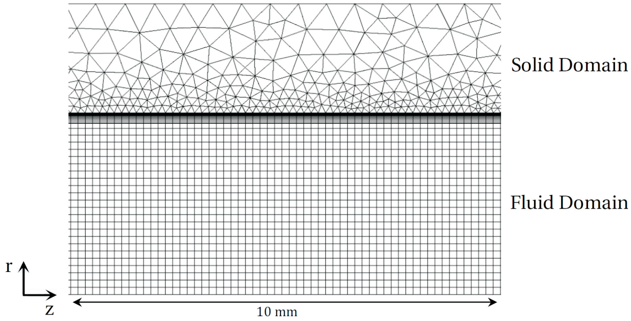

Figure 4.3: *Mesh for a 10 mm section of the 2D computational domain.*

The steady state formulation of the momentum equation given by equation 3.2 reads:

$$\rho\left(\vec{u}\cdot\vec{\nabla}\right)\vec{u}=-\vec{\nabla}p-\vec{\nabla}\cdot\vec{\vec{\tau}}+\rho\vec{f} \tag{4.2}$$

where the viscous stress tensor is prescribed by Newton's law of viscosity:

$$\vec{\vec{\tau}}=-\mu\left(\vec{\nabla}\vec{u}+\left(\vec{\nabla}\vec{u}\right)^{T}\right)+\frac{2}{3}\mu\left(\vec{\nabla}\cdot\vec{u}\right)\vec{\vec{\delta}}. \tag{4.3}$$

The volumetric force vector accounts for the gravity force that acts downward in z-direction:

$$\vec{f}=\left\{\begin{array}{c} f_r \\ f_z \end{array}\right\}=\left\{\begin{array}{c} 0 \\ -g \end{array}\right\}. \tag{4.4}$$

Conservation of energy is described by the equation of change for temperature, Eq. 3.54, without the terms that represent pressure work and viscous heating. These simplifications are considered reasonable since no large pressure gradients will occur inside the reactor, and the heat generated by viscous effects will be negligible compared to the heat that is transferred through the pipe wall. Expanding the material derivatives and disregarding the time-dependent terms in this expression leads to:

$$\rho C_p\left(\vec{u}\cdot\vec{\nabla}\right)T=\dot{Q}-\vec{\nabla}\cdot\vec{q} \tag{4.5}$$

where the heat flux is given by Fourier's law:

$$\vec{q}=-k\vec{\nabla}T.$$

The heat source term $\dot{Q}$ is zero for heat transfer analysis, but will be used to include heat effects due to chemical reactions in Section 4.9.1.

4.4 Turbulence modeling

The time-dependent chaotic behavior in the fluid flow occurs at a wide range of time and length scales. Although turbulence is in principle fully described by the Navier-Stokes equations, Eq. 3.2, a huge number of elements are required to capture the smaller scales in the flow. For this reason, the small scales are modeled using a turbulence model, while the Navier-Stokes equations are solved for the averaged variables.

The turbulence model chosen for the 2D reactor simulations is the low-Reynolds number k-ϵ turbulence model [125]. In comparison to the standard k-ϵ turbulence model, the low-Reynolds formulation provides equations for resolving regions of slow flow (close to walls) far better. Though computationally more expensive, the low-Reynolds model should be used in models where the effects of walls are important. This is certainly the case for the non-isothermal flow in the reactor, where large property variations occur in the boundary layer and the heat flux at solid-liquid interface highly affects the final solution. The superiority over the standard k-ϵ turbulence model has been confirmed in literature [51].

While Reynolds-averaging is applied for incompressible flows, resulting in the well-known Reynolds averaged Navier-Stokes equations (RANS), a more convenient method for compressible flow is Favre averaging. The Favre averaging method is density-based to suppress terms involving density fluctuations. Variables are decomposed into an averaged component, indicated with a tilde ($\tilde{\phi}$), and a fluctuating component, indicated with a double prime (ϕ"):

$$\phi = \tilde{\phi} + \phi" \tag{4.6}$$

where the averaged component is defined by:

$$\tilde{\phi} = \frac{1}{\bar{\rho}} \lim_{t_0 \to \infty} \frac{1}{t_0} \int_{t}^{t+t_0} \rho(\vec{x},\tau)\phi(\vec{x},\tau)d\tau. \tag{4.7}$$

This concept is illustrated in Fig. 4.4, where the velocity component $u(t)$ in "steadily driven turbulent flow" is decomposed into the averaged value $\tilde{u}$ and its fluctuation $u"(t)$.

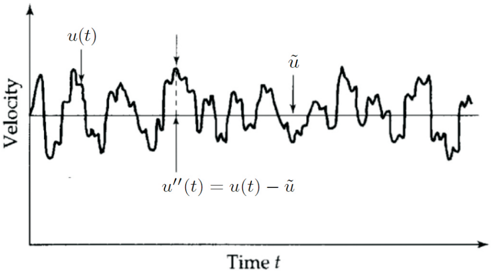

Figure 4.4: *Sketch showing the velocity component u as well as its smoothed value $\tilde{u}$ and its fluctuation u” in turbulent flow for "steadily driven turbulent flow" in which $\tilde{u}$ does not depend on time [21].*

When Favre averaging is applied to the model equations, Eqs. 4.1, 4.2 and 4.5 become:

$$\vec{\nabla}\cdot(\bar{\rho}\,\tilde{\vec{u}})=0 \tag{4.8}$$

$$\bar{\rho}\left(\tilde{\vec{u}}\cdot\vec{\nabla}\right)\tilde{\vec{u}}=-\vec{\nabla}\tilde{p}-\vec{\nabla}\cdot\left(\tilde{\vec{\vec{\tau}}}+\tilde{\vec{\vec{\tau}}}_T\right)+\bar{\rho}\vec{f} \tag{4.9}$$

$$\bar{\rho}C_p\left(\tilde{\vec{u}}\cdot\vec{\nabla}\right)\tilde{T}=\dot{Q}-\vec{\nabla}\cdot\left(\tilde{\vec{q}}+\tilde{\vec{q}}_T\right). \tag{4.10}$$

Here $\tilde{\vec{\vec{\tau}}}$ is the Favre averaged viscous stress tensor:

$$\tilde{\vec{\vec{\tau}}}=-\mu\left(\vec{\nabla}\tilde{\vec{u}}+\left(\vec{\nabla}\tilde{\vec{u}}\right)^T\right)+\frac{2}{3}\mu\left(\vec{\nabla}\cdot\tilde{\vec{u}}\right)\vec{\vec{\delta}} \tag{4.11}$$

and $\tilde{\vec{\vec{\tau}}}_T$ is the Favre-averaged Reynolds stress tensor, which is modeled according to the turbulent viscosity hypothesis:

$$\begin{aligned}\tilde{\vec{\vec{\tau}}}_T &= \overline{\rho\,\vec{u}"\vec{u}"} \\ &= -\mu_T\left(\vec{\nabla}\tilde{\vec{u}}+\left(\vec{\nabla}\tilde{\vec{u}}\right)^T\right)+\frac{2}{3}\left(\mu_T\left(\vec{\nabla}\cdot\tilde{\vec{u}}\right)+\bar{\rho}\,k\right)\vec{\vec{\delta}}.\end{aligned} \tag{4.12}$$

Transport equations for the turbulent kinetic energy, k, and the turbulent energy dissipation rate, ϵ, are as follows:

$$\rho\frac{\partial k}{\partial t}+\rho\,\vec{u}\cdot\vec{\nabla}k=\vec{\nabla}\cdot\left[\left(\mu+\frac{\mu_T}{\sigma_k}\right)\vec{\nabla}k\right]+P_k-\rho\epsilon \tag{4.13}$$

$$\rho\frac{\partial \epsilon}{\partial t}+\rho\,\vec{u}\cdot\vec{\nabla}\epsilon=\vec{\nabla}\cdot\left[\left(\mu+\frac{\mu_T}{\sigma_\epsilon}\right)\vec{\nabla}\epsilon\right]+C_{\epsilon1}\frac{\epsilon}{k}P_k-f_\epsilon C_{\epsilon2}\rho\frac{\epsilon^2}{k} \tag{4.14}$$

with the auxiliary equations:

$$P_k=\mu_T\left[\vec{\nabla}\vec{u}:\left(\vec{\nabla}\vec{u}+\left(\vec{\nabla}\vec{u}\right)^T\right)-\frac{2}{3}\left(\vec{\nabla}\cdot\vec{u}\right)^2\right]-\frac{2}{3}\rho k\left(\vec{\nabla}\cdot\vec{u}\right) \tag{4.15}$$

$$\mu_T=\rho f_\mu C_\mu\frac{k^2}{\epsilon} \tag{4.16}$$

$$f_\mu=\left(1-\exp^{-l^*/14}\right)^2\left(1+\frac{5}{R_t^{3/4}}\exp^{-(R_t/200)^2}\right) \tag{4.17}$$

$$f_\epsilon=\left(1-\exp^{-l^*/3.1}\right)^2\left(1-0.3\exp^{-(R_t/200)^2}\right) \tag{4.18}$$

$$l^*=\frac{\rho\,u_\epsilon l_w}{\mu}\qquad R_t=\frac{\rho\,k^2}{\mu\epsilon}\qquad u_\epsilon=\left(\frac{\mu\epsilon}{\rho}\right)^2 \tag{4.19}$$

and the tuning coefficients are given by:

$$C_{\epsilon1}=1.5\qquad C_{\epsilon2}=1.9\qquad C_\mu=0.09\qquad \sigma_k=1.4\qquad \sigma_\epsilon=1.5. \tag{4.20}$$

The parameter l_w in Eq. 4.19 is the distance to the closest wall, used by the turbulence model for regularization purposes or to approximate the mixing length. It is determined by solving the modified Eikonal equation [41]:

$$\vec{\nabla}\Lambda \cdot \vec{\nabla} + \sigma_w \Lambda \left(\vec{\nabla} \cdot \vec{\nabla}\Lambda\right) = (1+2\sigma_w)\Lambda^4 \tag{4.21}$$

where $\Lambda \equiv 1/l_w$ and σ_w is a small constant by default set to 0.1.

The heat transport turbulence model of Kays-Crawford [56] is used to model the turbulent heat flux in Eq. 4.10. The influence of the turbulent fluctuations on the temperature field is taken into account by adding a turbulent contribution to the thermal conductivity of the fluid:

$$\tilde{\vec{q}} + \tilde{\vec{q}}_T = -(k+k_T)\vec{\nabla} T \tag{4.22}$$

where k is the thermal conductivity of the fluid and k_T is calculated from an expression for the turbulent Prandtl number:

$$\begin{aligned} \mathrm{Pr}_T &= \frac{C_p \mu_T}{k_T} \\ &= \left[\frac{1}{2\mathrm{Pr}_{T\infty}} + \frac{0.3}{\sqrt{\mathrm{Pr}_{T\infty}}}\frac{C_p \eta_T}{k} - \left(0.3\frac{C_p \eta_T}{k}\right)^2 \left(1-\exp^{-k/(0.3 C_p \eta_T \sqrt{\mathrm{Pr}_{T\infty}})}\right)\right]^{-1}. \end{aligned} \tag{4.23}$$

Here the turbulent Prandtl number at infinity $\mathrm{Pr}_{T\infty}$ is experimentally determined to be 0.85 and the turbulent viscosity μ_T is given by equation 4.16. This model has been compared to other models for Pr_T and found to be good for most kind of turbulent wall bounded flows except for liquid metals [56].

4.5 Boundary conditions

The boundary conditions used for the 2D-calculations are indicated in the computational domain in Fig. 4.5. The fluid enters the pipe with a uniform velocity profile, passes an insulated entrance section of 0.1 m and is then heated

Table 4.2: *Boundary conditions for the 2D heat transfer model.*

Boundary	**Condition**	**Symbol**	**Unit**	**Value**
Inlet	mass flux	G	[kg/m^{2}s]	200
Inlet	temperature	$\mathrm{T_{in}}$	[°C]	350
Heated wall ($z>0$)	temperature	$\mathrm{T_W}$	[°C]	600
Oulet	relative pressure	$\mathrm{p_{out}}$	[barg]	0

over a length of 2.5 m using a constant wall temperature. At the outlet, it is assumed that the relative pressure, the normal shear stresses and the normal heat flux are zero. In order to allow for fluid data import into COMSOL, all fluid properties in the 2D-calculations are evaluated at a fixed reference pressure of 300 bar. This simplification introduces only a small error since the pressure inside the pipe is more or less constant and the fluid properties are weak functions of the pressure. The specifications for the mass flux, the pressure and the temperatures shown in Fig. 4.5 are listed in Table 4.2.

The ends of the solid domain and the outer wall of the entrance section are assumed to be perfectly insulated. A no-slip condition is applied to the velocity at the inner wall. The corresponding wall conditions for k and ϵ in the low-Reynolds formulation are:

$$k=0 \tag{4.24}$$

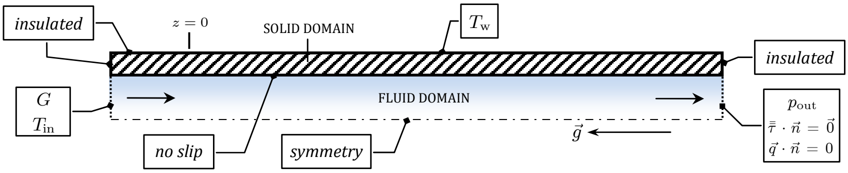

Figure 4.5: *Boundary conditions for the 2D heat transfer model, indicated in the computational domain.*

$$\epsilon = 2\frac{\mu}{\rho}\frac{k}{l_w^2} \tag{4.25}$$

where l_w is the distance to the closest wall, calculated using Eq. 4.21. The symmetry condition at the centerline in Fig. 4.5 prescribes zero flux and vanishing shear stresses.

4.6 Solving the 2D-model equations

The 2D-model equations have been solved on a linux-based computer cluster using the software package COMSOL Multiphysics (v4.1). The solution has been calculated on 1 node for the non-reacting flow and on 4 nodes for the reacting flow. Each node consists of two quadcore Xeon E5620 processors running at 2.40 GHz and 24 GB of memory. The solving process took several hours using a direct solver. Direct solvers use more memory than iterative solvers, but are more robust and suitable for highly non-linear and multiphysics problems. Since the equations governing fluid flow and convective heat transfer are numerically unstable by nature, stabilization techniques have been applied to dampen the effect of oscillations in the solution by means of artificial diffusion. Only consistent stabilization methods have been used, which in contrast to inconsistent methods do not perturb the original transport equation. The convergence criterion for the calculations is a maximum relative error of $1 \cdot 10^{-3}$.

4.7 2D simulation results

This section presents the results of the heat transfer simulations in the 2D computational domain as shown in Section 4.2 for the case specified in Section 4.5. In contrast to the 1D-calculations, the results shown below give detailed information on the flow field and heat transfer over the cross-section of the pipe. The solution gives insight into the effect of the phase transition on the heated water flow, and analysis of the variations in radial direction allows to assess the

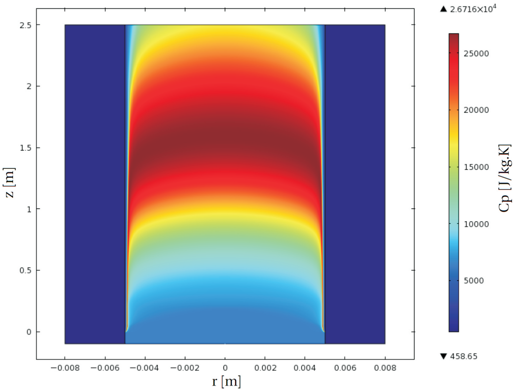

Figure 4.6: *Surface plot of the isobaric heat capacity in J/kg·K for non-reacting flow. The coordinates on the axes are expressed in meters.*

’plug flow’ assumption in the 1D-model. A quantitative comparison with the 1D-results is found in Section 4.10.

Fig. 4.6 shows a surface plot of the isobaric heat capacity, where the solution is projected onto the surface of the computational domain. The domain has been mirrored in the centerline of the pipe to obtain a view on the full cross-section and the geometry has been scaled for convenient visualization. Since the isobaric heat capacity reaches a maximum at the pseudo-critical point, the plot indicates where the phase transition to supercritical water takes place. It can be seen that the pseudo-critical point is reached in a thin layer that sticks close to the wall over a long distance, separating gaseous supercritical water adjacent to the wall from the liquid bulk flow at sub-critical temperatures. This pseudo-critical region slowly moves toward the center until the bulk flow reaches the pseudo-critical temperature around 1.5 m pipe height. The bulk flow has still not completely passed the phase trajectory after the total heated length of 2.5 m, which means the mean outlet temperature will be far from the desired 600°C.

The plot in Fig. 4.7 represents the temperature field with isotherms. The flow is heated from 350°C at the inlet to a mean temperature of 424°C at the outlet by the hot wall of 600°C. From the mutual distance between the isotherms it can be concluded that the temperature increase is fastest near the inlet and is slowest where the bulk flow reaches the pseudo-critical temperature. The pseudo-critical region acts like a heat sink due to the high heat capacity, which causes the temperature to rise more slowly. Furthermore, less heat is transported from the wall through the supercritical region due to the steep decrease in conductivity (Fig. 1.3).

Fig. 4.8 shows the temperature profiles at different pipe heights. The figure gives better insight into the temperature gradient near the wall and the influence of the phase transition on the temperature variations over the radius. In general, the profiles over the diameter are sufficiently uniform to justify the plug flow assumption that was made for deriving the 1D-model equations.

The velocity plot in Fig. 4.9 shows the velocity magnitude, which is defined as:

$$U=\sqrt{u_r^2+u_z^2} \tag{4.26}$$

where u_r and u_z are the velocities in radial and longitudinal direction. It can be noted that the no slip condition at the wall is satisfied. The fluid is accelerated in the pseudo-critical regions due to buoyancy forces and volumetric expansion. The increased velocity near the wall in the lower half of the pipe

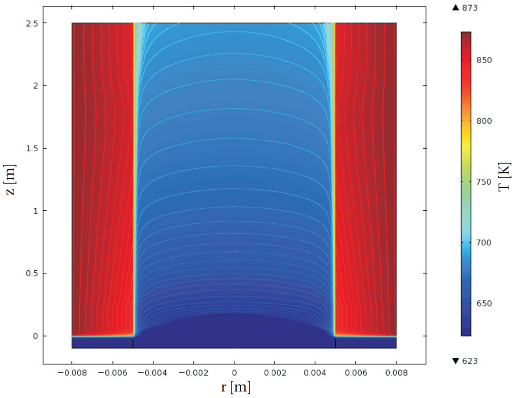

Figure 4.7: *Surface plot of the temperature in K and isotherms for non-reacting flow. The coordinates on the axes are expressed in meters.*

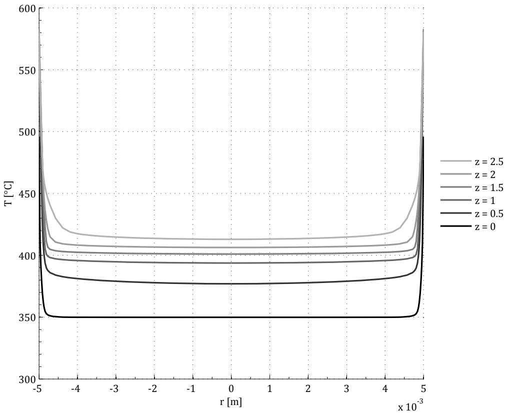

Figure 4.8: *Temperature profiles taken at different pipe heights for non-reacting flow. The temperatures are expressed in °C and the pipe heights are in meters.*

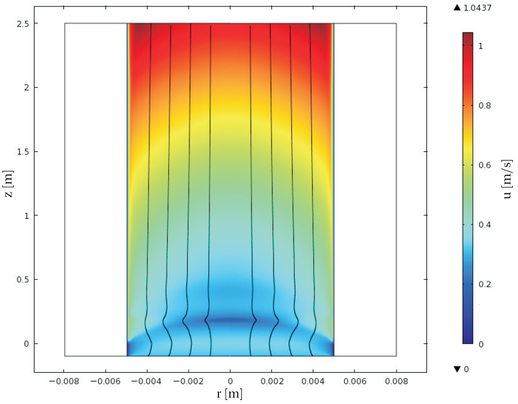

Figure 4.9: *Surface plot of the velocity in m/s for non-reacting flow. The coordinates on the axes are expressed in meters.*

causes suction of fluid from the bulk flow towards the wall, which results in the hump in the streamlines shown in the figure.

The velocity magnitude over the radius at different pipe heights is plotted in

Fig. 4.10. The profiles show that the flow along hot pipe wall does not resemble a plug flow. This finding contradicts the conclusion of the temperature profile analysis above. The plug flow assumption on which the 1D-model is based may be considered inaccurate when it comes to the flow field, but the 1D-model cannot be disqualified on beforehand as the temperature field is probably more important for heat transfer simulations. A comparison with the velocity profiles in Fig. 3.8(a) shows that the flow is turbulent, with high Grashof numbers at the start of the heated pipe section. The velocity profile at $z = 0$ in Fig. 4.10 is not yet influenced by heating effects and therefore resembles profile A for low Grashof numbers in Fig. 3.8(a). As soon as the fluid enters the heated section of the pipe, the velocity profile is quickly transformed to profile F due to strong buoyancy forces. The velocity differences over the radius then decrease toward the outlet because of the accelerating bulk flow. At the outlet, the velocity profile is similar to profile E.

The thin pseudo-critical region near the wall that is observed in Fig. 4.6 leads to very large density differences over the pipe diameter. This can be clearly seen in the density plot in Fig. 4.11. The high gradient in density suggests that the critical heat flux has been exceeded and pseudo-film boiling is taking place at the wall. In Section 3.1.3 it is pointed out that film boiling causes deterioration

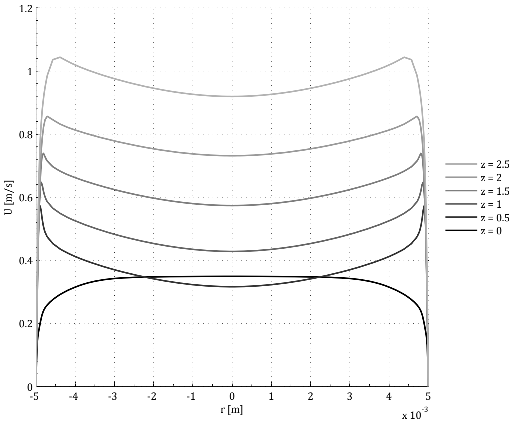

Figure 4.10: *Velocity profiles taken at different pipe heights for non-reacting flow with a mass flux of 200 kg/m*^{2} *s. The pipe heights are given in meters.*

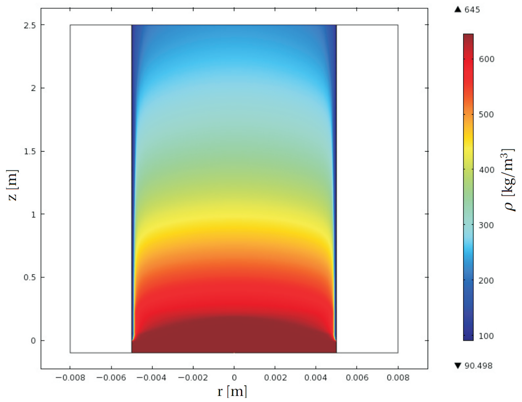

Figure 4.11: *Surface plot of the density in kg/m*^{3} *for non-reacting flow. The coordinates on the axes are expressed in meters.*

of the heat transfer and should therefore be avoided if possible.

In order to verify the presumption that pseudo-film boiling occurs near the pipe wall, the solution has been recalculated with a wall temperature that lin-

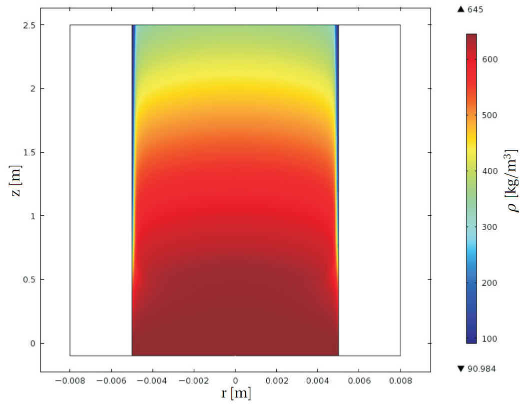

Figure 4.12: *Surface plot of the density in kg/m*^{3} *for non-reacting flow with linearly increasing wall temperature. The coordinates on the axes are expressed in meters.*

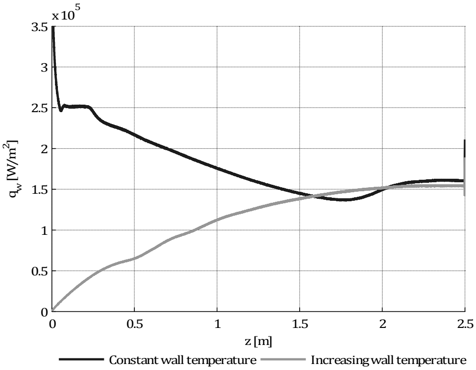

Figure 4.13: *Wall heat flux as function of the pipe height for non-reacting flow using a constant wall temperature and a linearly increasing wall temperature.*

early increases from inlet temperature (350°C) at $z = 0$ to the original wall temperature (600°C) at $z = 2.5$ m to capture the onset of this effect. The wall heat flux at the location where the onset of film boiling is observed can then be compared with the predictions for the critical heat flux given in Fig. 3.4. The simulation using a gradually increasing wall temperature resulted in the den-

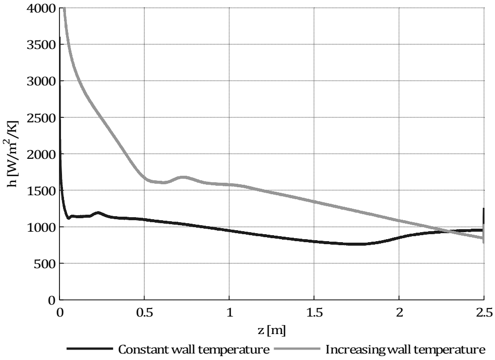

Figure 4.14: *Heat transfer coefficient as function of the pipe height for non-reacting flow using a constant wall temperature and a linearly increasing wall temperature.*

sity plot shown in Fig. 4.12. It can be seen that the onset of pseudo-film boiling is located at approximately $z = 0.75$ m.

Fig. 4.13 shows the wall heat flux as function of the pipe height for both the constant and the linearly increasing wall temperature cases. The line corresponding to the simulation with increasing wall temperature indicates that the wall heat flux at $z = 0.75$ m is about 90 kW/m^2. This value is very close to the critical heat flux for G = 200 kg/m^{2}s as predicted by the correlations of Yamagata et al. [133] and Mokry et al. [83] plotted in Fig. 3.4. The good agreement of the critical heat flux as obtained from the 2D-simulations with the empirical correlations from literature is a confirmation of the occurrence of pseudo-film boiling.

The heat transfer efficiency for both cases can be assessed by comparing the heat transfer coefficients given in Fig. 4.14. The heat transfer coefficient has been calculated using the wall heat flux, wall temperature and temperature at the centerline according the following equation:

$$h = \frac{q_w}{T_w - T_{ax}} \tag{4.27}$$

The shape of the line for constant wall temperature can be recognized in the line for the gradually increasing wall temperature, but is shifted upwards in the pipe because of the later onset of film boiling. By comparing the graphs in Figs. 4.13 and 4.14 it can be concluded that a higher temperature difference generally leads to an increase in heat flux, but at the same time to a less efficient heat transfer regime.

In order to gain more insight into the behavior of the heat transfer coefficient over the pipe length, all parameters involved in Eq. 4.27 are plotted in one figure for each of the heating methods. Fig. 4.15 shows how the heat transfer coefficient, wall temperature, centerline temperature and wall heat flux are related for the case of constant wall temperature. The values of the first three parameters in the list can be read from the left axis, while the wall heat flux is indicated by the right axis.

The small increase of the heat transfer coefficient around $z = 0.2$ m coincides with the location where the centerline temperature starts to rise. Since the heat flux and wall temperature are constant, the result is a smaller tempera-

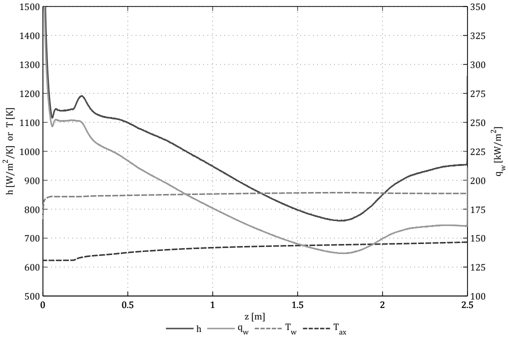

Figure 4.15: *Heat transfer coefficient, wall heat flux, wall temperature and centerline temperature as function of the pipe height for non-reacting flow and constant wall temperature.*

ture difference and thus a higher heat transfer coefficient. This effect is however quickly followed by a decline in heat transfer due to a growing low-density layer near the wall (Fig. 3.8(d)). While both the wall temperature and centerline temperature increase very slowly, deterioration of the heat transfer continues until the bulk flow has passed the pseudo-critical point. From this point,

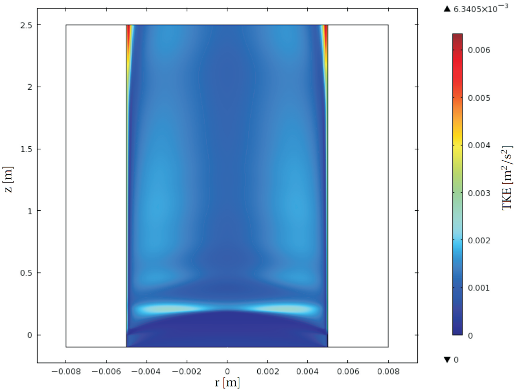

Figure 4.16: *Surface plot of the turbulent kinetic energy in m^2/s^2 for non-reacting flow with constant wall temperature. The coordinates on the axes are expressed in meters.*

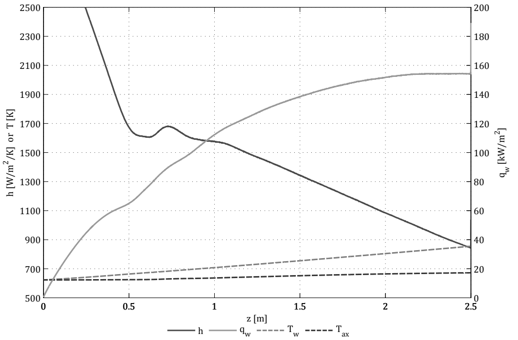

Figure 4.17: *Heat transfer coefficient, wall heat flux, wall temperature and centerline temperature as function of the pipe height for non-reacting flow and increasing wall temperature.*

the heat flux is recovering (Fig. 3.8(e)) and the wall temperature starts to decrease slowly.

The severe impairment of heat transfer at high heat flux and the recovery further downstream where the bulk temperature passes the pseudo-critical temperature have been noted in Jackson and Hall [53] on basis of experimental data. The authors suggest that deterioration of heat transfer may be related to the turbulence near the boundary layer. This explanation has been adopted in other literature, see Section 3.1.3, and may also explain the recovery of heat transfer observed in Fig. 4.15. The turbulent kinetic energy plot in Fig. 4.16 shows high turbulence production in that particular region, which may well be responsible for the increase in heat flux.

Fig. 4.17 shows the parameter values that characterize the heat transfer for the case of gradually increasing wall temperature. The brief increase of the heat transfer coefficient at $z = 0.6$ m occurs at the location where the temperature in the boundary layer equals the pseudo-critical temperature. The local phase change at the wall results in a larger slope of the heat flux over a few centimeters, but then the slope restores due to the gaseous layer that is formed at the wall. From this point, around $z = 0.75$ m, the critical heat flux is reached and heat transfer starts to deteriorate. The heat transfer coefficient does not show the recovery that is observed in Fig. 4.15. In the plot of the turbulent kinetic energy in Fig. 4.18, where the color scale is identical to the scale in Fig. 4.16, it can be seen that there is hardly any turbulence production near the wall. This is in agreement with the assumption that the turbulent diffusivity is causing the recovery in heat transfer for the case of constant wall temperature.

4.8 Experimental setup for temperature measurements in a supercritical water flow

Experimental data on supercritical water flows found in current literature has been generated in view of designing more efficient power plants. As these studies consider water at supercritical pressures as the coolant of the plant, measurements are focused on wall temperatures of the pipe with a constant wall heat flux. Local fluid temperatures are not so easy to obtain, but provide much more useful information for comparison with simulations of the temperature field.

The intention to validate the 2D-simulations using temperature data of the flow therefore has led to the design and construction of an experimental setup. Accurate temperature data at different locations in the pipe has been obtained

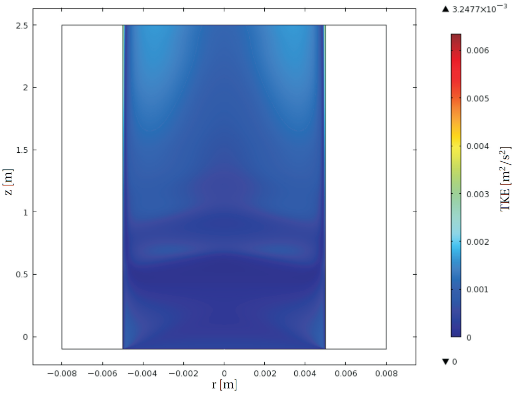

Figure 4.18: *Surface plot of the turbulent kinetic energy in m^2/s^2 for non-reacting flow with increasing wall temperature. The coordinates on the axes are expressed in meters.*

as the setup allows to measure directly into the water flow at supercritical conditions. In this chapter, a detailed description of the setup is followed by a comparison of test results with a 2D-simulation of the lab case.

4.8.1 Description of the experimental setup

The main part of the setup consists of an oven containing a stainless steel pipe with an inner diameter of 10 mm that is mounted into a fluidized sand bed. The oven surrounding the fluidized bed heats the recirculating sand that keeps the pipe wall at constant temperature. The setup is schematically shown in Fig. 4.19, in which the thermocouples and pressure sensors are numbered for convenient referencing.

At the bottom, water is pumped into the pipe under high pressure using a HPLC pump. The water is preheated by an electric heater and trace heating cables until the desired temperature is reached at the bottom of the sand bed. This temperature is measured in the flow using a single thermocouple (TC 0) that is inserted through the bottom end of the pipe. The water is then heated further by the fluidized hot sand, which keeps the pipe wall temperature constant. Three thermocouples in row (thermocouples 1 to 3) measure the temperature profile in the flow. These thermocouples can be shifted in axial direction to measure at different heights. Seven additional thermocouples, coupled to the heated pipe at different heights, are used to measure the outside wall temperature of the pipe during an experiment.

Once the water has passed the oven, it is cooled to a temperature below 70°C by a tube-in-tube heat exchanger, this is the temperature limit for the back-pressure regulator (BPR) controlling the system pressure. Air is supplied in the top section of the pipe to provide cooling for the viton sealing around the thermocouples and carries the gaseous water to the condensation section. The output signals of the thermocouples and pressure sensors are monitored and processed using LabVIEW.

For safety reasons, the system is remotely controlled from a room next to the bunker where the setup is located. Sound alarms have been setup in LabVIEW to warn in case the system pressure is too high or if the temperature near some delicate parts attains critical values (thermocouples 4, 6 and 7). A rupture disc was installed in a cold section of the system containing liquid water to prevent

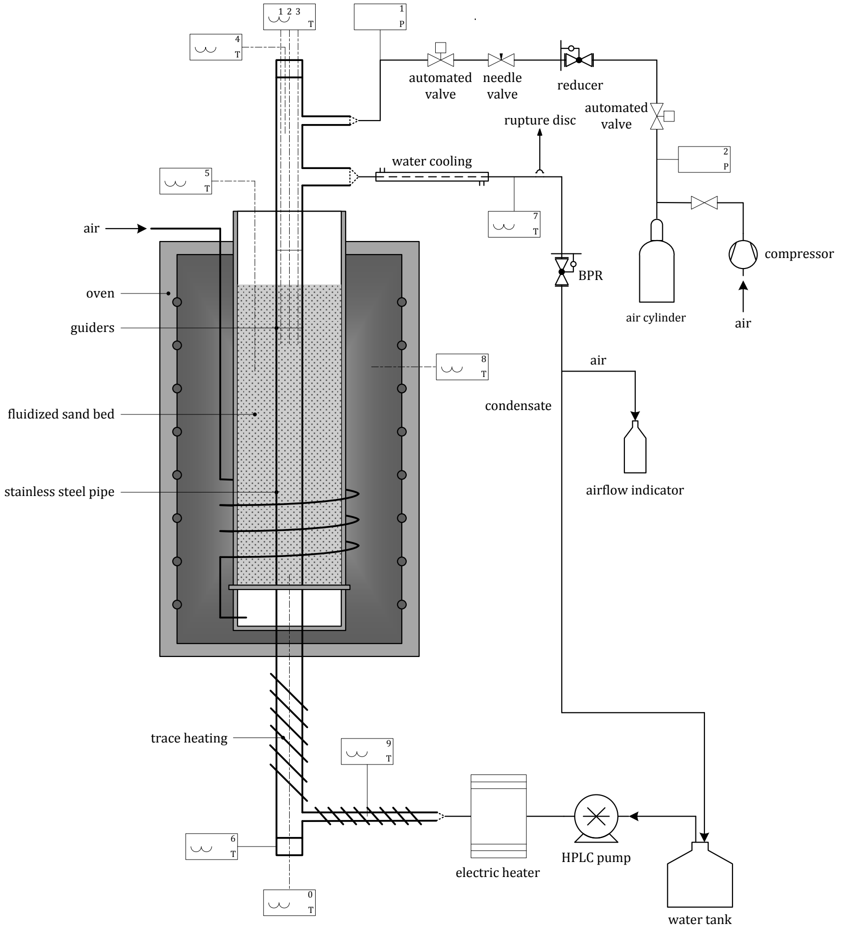

Figure 4.19: *Scheme of the experimental setup.*

failure of the construction at unexpected locations without releasing hot steam into the environment. An emergency button allows to quickly shut down all power, which also cuts off the pressurized air supply as the automated valves are set to normally closed.

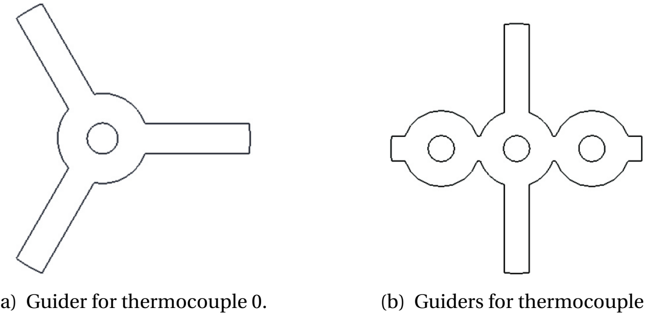
(a) Guider for thermocouple 0.
(b) Guiders for thermocouple 1 to 3.

Figure 4.20: *Thermocouple guiders.*

Thermocouples 0 to 3 are held into position by stainless steel guiders that have been pinched to the thermocouple wires. The guiders, shown in Fig. 4.20, were fabricated using laser cutting to achieve the desired tolerances.

4.8.2 Calibration of the sensors

The two identical pressure sensors have been calibrated using a highly accurate reference manometer in order to determine the relation between output voltage and relative pressure. The measurement points with the linear curve fit are shown in Fig. 4.21. Assuming identical behavior of the other pressure sensor, the output voltages of both sensors are converted to pressures using the expression of the linear curve fit derived from the calibration data.

The four K-type thermocouples that are installed for measurements into the flow (TC 0, 1, 2 and 3) have been calibrated to determine the accuracy. The calibration data has been acquired by placing the bundle of thermocouples into a fluidized bed and logging the temperatures during cool down of the bed. The thermocouple that was to be located inside the flow at the bottom of the sand bed (TC 0) served as a reference. According to the calibration report of the supplier, TC 0 shows an error of +0.75°C at 500°C with an accuracy of 0.6°C. The deviation of the remaining three thermocouples from the reference sensor is plotted in Fig. 4.22.

The mutual deviations have been reduced by using linear curve fits to compensate for the average temperature differences. In Fig. 4.23 it can be seen that a good match with the reference thermocouple is achieved after compensation, with a maximum mutual deviation of 0.75°C at temperatures below 400°C. The maximum deviations from TC 0 in this temperature range are -0.75 and +0.4°C. Together with the calibration data for the reference thermocouple, the temperature measurements have an estimated total error between -0.6 and +1.75°C.

4.8.3 Test conditions and testing procedure

Each measurement starts by shifting thermocouples 1 to 3 in Fig. 4.19 to the desired position in the pipe. After reassembling the setup, a cold test is performed to check for any leakages. Then the trace heating cables, preheater and oven are turned on to preheat the water and heat up the fluidized bed. Air cooling for the viton sealing in the top of the pipe is supplied by opening the valves to the gas cylinder filled with compressed air. An overpressure in the cylinder forces air into the pipe, where the pressure is set to 240 bar using the back-pressure regulator. The temperature controllers are tuned such that the inlet temperature measured by thermocouple 0 is maintained at 300°C. At

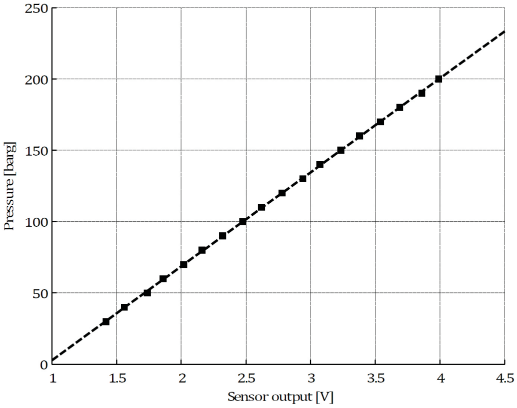

Figure 4.21: *Pressure sensor calibration data with linear curve fit.*

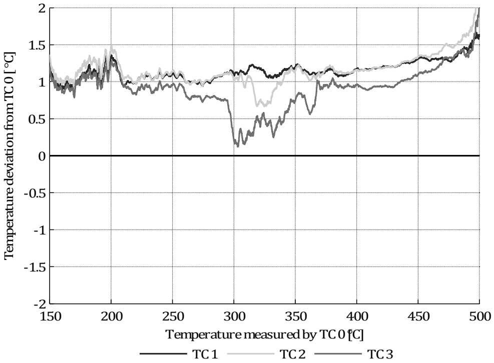

Figure 4.22: *Deviation of thermocouples 1, 2 and 3 from thermocouple 0.*

this point, the temperatures inside the flow measured by thermocouples 0 to 4 are recorded and stored in a datafile. Seven additional thermocouples, coupled to the heated pipe at different heights, are used to measure the outside wall temperature of the pipe during an experiment. The test conditions are summarized in Table 4.3. The procedure described above is repeated to obtain data over the effective test length of 0.45 m with steps of 5 cm.

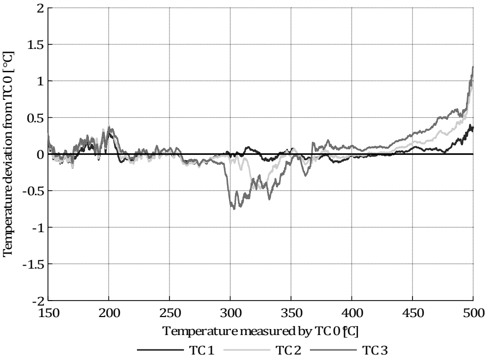

Figure 4.23: *Deviation of thermocouples 1, 2 and 3 from thermocouple 0 after compensation.*

Table 4.3: *Test conditions for the temperature measurements in the lab.*

Parameter	Symbol	Unit	Value
Mass flux	G	[kg/m^{2}s]	6.6, 10
Pressure	p	[bar]	240
Inner diameter	D	[mm]	10
Length of the heated pipe section	L	[mm]	450
Inlet temperature	T_{in}	[°C]	300
Wall temperature	T_W	[°C]	600

4.8.4 Simulation of the supercritical water flow in the laboratory

The 2D-model as described in Section 4.2 has been used to simulate a flow case that corresponds to the test conditions used for the temperature measurements in supercritical water as listed in Table 4.3. The mass flux was decreased in steps of 5 kg/m^2·s from 20 to eventually 6.6 kg/m^2·s, which is similar to the laboratory case. At these low mass fluxes, the 2D-model predicts that the buoy-

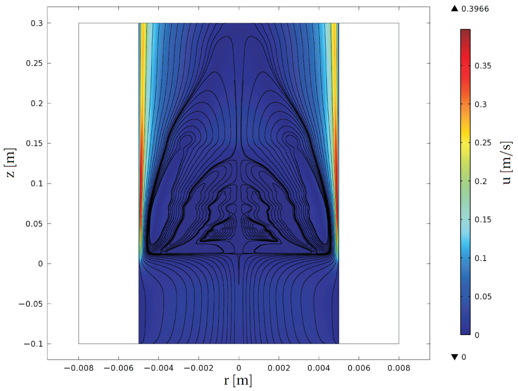

Figure 4.24: *Surface plot of the velocity magnitude with streamlines in m/s for G = 10 kg/m^2·s. The coordinates on the axes are expressed in meters.*

ancy forces are highly dominant and induce recirculation zones near the inlet. Fig. 4.24 shows the velocity magnitude defined in Eq. 4.26 and streamlines for a mass flux of 10 kg/m^2·s, illustrating the effect of the recirculating fluid on the flow field.

As a result of the recirculation observed in Fig. 4.24, the lab case simulations involve high gradients and small length scales that require a grid size of 0.05 mm. This grid is represented by the rightmost data points in Fig. 4.2, showing acceptable convergence for a mass flux of 6.6 kg/m^2·s. The pipe length has been limited to 300 mm, which covers the most interesting part of the flow and allowed the calculation to run at only one computational node. Table 4.4 gives an overview of the specifications for the simulated case to generate data for validation of the 2D-model in Section 4.8.5.

4.8.5 Validation of the 2D-model with the experimental data

In this section, the experimental results are compared to the temperatures as calculated using the 2D-model. Since the data points obtained with thermocouples 1 to 3 are to be compared with results of steady state calculations, they have been time-averaged using:

$$\bar{T} = \frac{1}{3}\sum_{i=1}^{3}\left[\frac{1}{n+1}\sum_{j=0}^{n} T_i(t_0 + n\Delta t)\right] \tag{4.28}$$

Table 4.4: *Specification of the simulated cases for validation of the 2D-model.*

Parameter	Symbol	Unit	Value
Mass flux	G	[kg/m^2s]	6.6, 10, 15, 20
Pressure	p	[bar]	240
Inner diameter	D	[mm]	10
Length of the heated pipe section	L	[mm]	300
Inlet temperature	T_{in}	[°C]	300
Wall temperature	T_W	[°C]	600

where i denotes the thermocouple index, ΔT is 1 s and n are the number of seconds taken from the data set. The time-averaged temperatures measured inside the flow are plotted with the surface-averaged numerical solutions for a mass flux of $G = 6.6$ kg/m^2·s in Fig. 4.25 and a mass flux of $G = 10$ kg/m^2·s in Fig. 4.26. Both figures show that the 2D-model slightly over predict the temperature measured in the setup. It is assumed that the small deviations are mainly caused by the effect of the recirculation zone present in the flow. The recirculation provides mixing of the fluid, thereby enhancing the heat transfer.

The good agreement between the numerical and experimental data as seen above proves that the 2D-model is accurate for low mass fluxes. When the flow fields shown in Fig. 4.24 for G = 10 kg/m^2·s and Fig. 4.10 for G = 200 kg/m^2·s are compared, it is clear that buoyancy forces are far less dominant over the pressure forces in the latter case. For this reason, possible errors due to the recirculation of the fluid will not occur at higher mass fluxes. The accuracy of the 2D-model for these cases is expected to be accurate because the flow is easier to calculate due too smaller buoyancy effects.

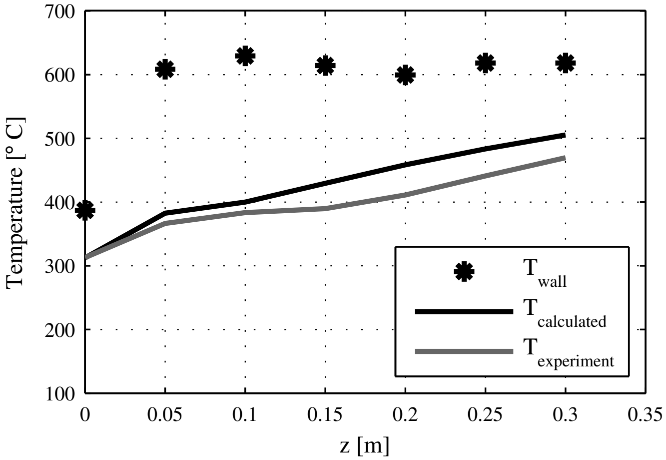

Figure 4.25: *Comparison of the 2D lab case simulation with the experimental data (G = 6.6 kg/m^2·s).*

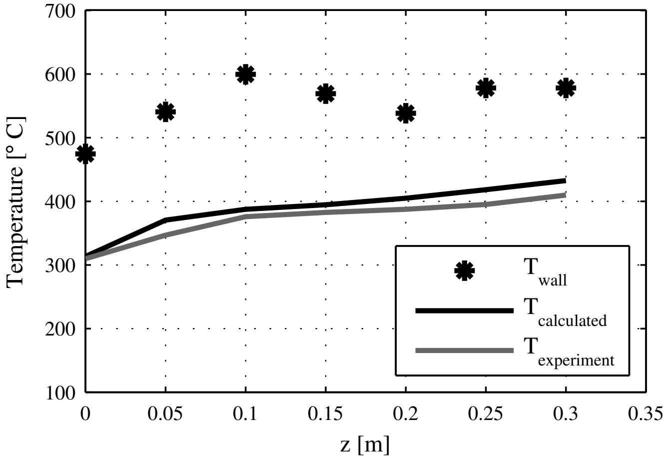

Figure 4.26: *Comparison of the 2D lab case simulation with the experimental data (G = 10 kg/m^2·s).*

4.9 Extension of the 2D-model for chemically reacting flow

Comparable to the extension of the 1D-model in Section 3.4 the 2D-model is also extended with equations describing chemistry and mass transfer. Sections 3.4.3 and 3.4.4 have discussed the estimation of the thermo-physical properties of the reacting mixture and the diffusion coefficients. The extension of the 2D-model and some additional boundary conditions are described in Sections 4.9.1 and 4.9.2. The simulations of reacting flow are conducted with an initial mass fraction of 10 wt% methanol. The results of the reacting flow simulations can be found in Section 4.9.3.

4.9.1 Extension of the 2D-model equations

Extension of the heat equation for the 2D-model given by Eq. 4.5 yields:

$$\rho C_p \left(\vec{u}\cdot\vec{\nabla}\right) T = \Delta H_r r_i + \vec{\nabla}\cdot\left(k\vec{\nabla}T\right) \tag{4.29}$$

The equation describing conservation of the individual chemical species that must be added the 2D-model follows from Eq. 3.6 by disregarding the transient term:

$$\rho\left(\vec{u}\cdot\vec{\nabla}\right) y_i = -\vec{\nabla}\cdot\vec{j}_i + r_i \tag{4.30}$$

Here ρ denotes the mixture density and $\vec{u}$ the mass average velocity of the mixture. The remaining variables are specific for species i, with y_i as the mass fraction, j_i the mass flux relative to the mass average velocity and r_i the reaction rate. The turbulent mass flux is not included in the model, so all variables can be simply replaced by the Favre-averaged variables.

If S species are present in the mixture, $S-1$ of the species equations are independent and solved for using Eq. 4.30. The mass fraction of the last species, chosen to be water in this study, is derived from Eq. 3.7, describing the condition that the sum of all mass fractions equals unity:

$$y_S = 1 - \sum_{i=1}^{S-1} y_i \tag{4.31}$$

In order to facilitate numerical implementation of the mass diffusion model, Eq. 3.8 is written into mixture-averaged form [57]. A new mixture-averaged diffusion coefficient is defined such that the first term on the right-hand side can be replaced with an equivalent Fickian term. In this new formulation, the diffusion process of species i only depends on its own the mole fraction gradient:

$$\vec{j}_i = -\rho\frac{M_i}{M} D_{im}\vec{d}_i - D_i^T\frac{1}{T}\vec{\nabla}T \tag{4.32}$$

where $\vec{d}_i$ are the diffusion driving forces and D_{im} denotes the diffusion coefficient for diffusion of species i into the mixture of the other species. By definition, the mixture-averaged coefficient has to satisfy:

$$D_{im}\vec{d}_i = -\frac{1}{M}\sum_{j\neq i}^{N} M_j D_{ij}\vec{d}_j. \tag{4.33}$$

Alternatively, the mixture-averaged coefficient can be approximated using the more practical expression:

$$D_{im} = \frac{1-y_i}{\sum_{j\neq i}^{N} x_j/\mathsf{D}_{ij}} \tag{4.34}$$

where D_{ij} are the binary diffusion coefficients. This well-known formula introduces an error of about 10% compared to the exact formulation of Eq. 4.33 [120]. Since water will be in great excess, it can moreover be stated that the mass and mole fraction will be almost unity for water. With this simplification Eq. 4.34 becomes:

$$D_{im} = \mathsf{D}_{i1} \tag{4.35}$$

where index 1 denotes water. The binary diffusion coefficients for all species to water, including the self-diffusion coefficient D11 are estimated in Section 3.4.4.

Next, the diffusion driving forces vector given by Eq. 3.9 is simplified by assuming ideal-gas diffusion behaviour in an isobaric system. In absence of any unequal external forces acting on the chemical species, the expression for $\vec{d}_j$ then reduces to:

$$\vec{d}_j = \vec{\nabla} x_j. \tag{4.36}$$

Thermal diffusion, represented by the second term on the right-hand side of Eq. 4.32, may become a substantial effect whenever there are strong temperature gradients and large size or molecular weight variations in the mixture [57]. Although strong temperature gradients are to be expected inside the reactor, thermal diffusion is disregarded because of the relatively small differences in molecular weights and the lack of information on the thermal diffusion coefficient.

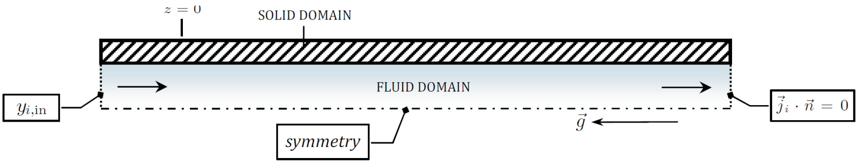

Figure 4.27: *Boundary conditions for the 2D-model for reacting flow, indicated in the computational domain.*

Combining Eqs. 4.32 and 4.36 while neglecting the thermal diffusion term leads to:

$$\vec{j}_i = -\rho y_i D_{im} \frac{\vec{\nabla} x_i}{x_i} \tag{4.37}$$

or, in terms of mass fractions:

$$\vec{j}_i = -\rho D_{im} \left(\vec{\nabla} y_i + y_i \frac{1}{M} \vec{\nabla} M \right) \tag{4.38}$$

where D_{im} is approximated using Eq. 4.35.

4.9.2 Additional boundary conditions

In addition to the boundary conditions for non-reacting flow given in Section 4.5, the conditions shown in Fig. 4.27 have been used to define the chemically reacting flow problem. Both the outlet condition and the symmetry condition prescribe zero normal mass flux. At the inlet, a mass fraction of 10 wt% is specified for methanol and 0 wt% for carbon monoxide and hydrogen.

4.9.3 2D simulation results for reacting flow

The results of the 2D-model for reacting flow show that methanol is mainly converted near the wall, where high fluid temperatures lead to high reaction rates (Fig. 4.28). Due to the strong non-linear relation between reaction rate

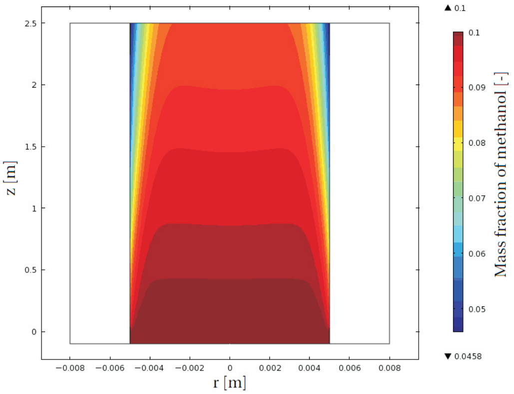

Figure 4.28: *Surface plot of the mass fraction of methanol. The coordinates on the axes are expressed in meters.*

and temperature (Fig. 3.18), it is not expected that the 1D-model is capable of describing the conversion of biomass correctly.

From Fig. 4.29, it can be concluded that the chemistry has a positive effect on the heat transfer. The bulk flow reaches the pseudo-critical temperature

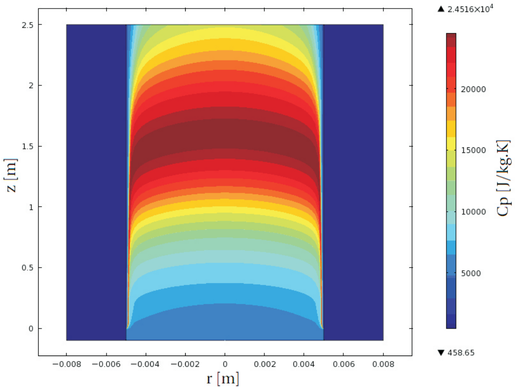

Figure 4.29: *Surface plot of the isobaric heat capacity in J/kg . K for reacting flow. The coordinates on the axes are expressed in meters.*

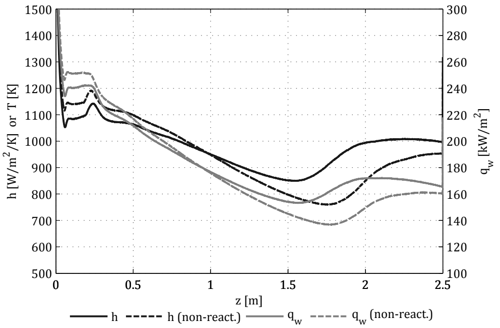

Figure 4.30: *Heat transfer coefficient, wall heat flux, wall temperature and centerline temperature as function of the pipe height for reacting flow. The heat transfer coefficient and heat flux for non-reacting flow are also shown to make a comparison.*

sooner than seen in Fig. 4.6, which is remarkable at first sight since the reaction is endothermic. Apart from the shift in the pseudo-critical region, the results for reacting and non-reacting flow are very similar regarding the isobaric heat capacity.

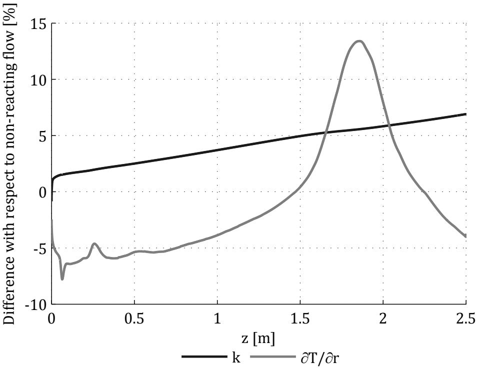

Figure 4.31: *Difference in thermal conductivity and radial temperature gradient near the wall for reacting flow with respect to non-reacting flow. The quantities have been measured at* $r = 4.99$ *mm as function of the pipe height.*

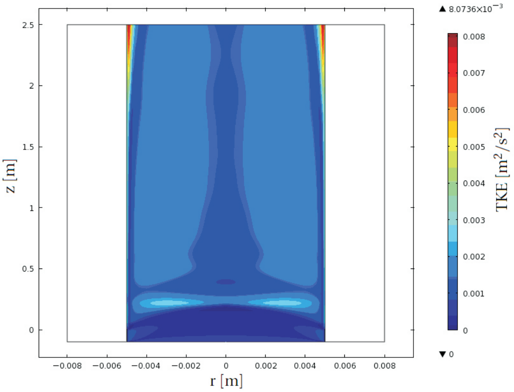

Figure 4.32: *Surface plot of the turbulent kinetic energy in* m^2/s^2 *for reacting flow. The coordinates on the axes are expressed in meters.*

The reason for the improved heat transfer as observed in the previous plot is investigated by comparing the heat flux and heat transfer coefficient. Fig. 4.30 shows the heat transfer coefficient, wall heat flux, wall temperature and centerline temperature as function of the pipe height. The dotted lines represent the heat transfer coefficient and the wall heat flux for the non-reacting flow as shown in Fig. 4.15.

The comparison in Fig. 4.30 makes clear that the deterioration of heat transfer is reduced for reacting flow. The relative increase of the heat flux over this section of the pipe has been examined by plotting the local thermal conductivity of the mixture and the temperature gradient in radial direction very close to the wall, which govern the normal wall heat flux according to Eq. 3.55. Fig. 4.31 shows that the radial temperature gradients are generally lower for reacting flow, probably as a result of the endothermic reaction. It can be seen that the thermal conductivity rises considerably due to the high conductivity of the hydrogen (Fig. 3.21) produced in the hot boundary layer. The increase in conductivity is larger than the decrease in the temperature gradient and therefore causes a net improvement of the heat transfer compared to the non-reacting flow case.

Fig. 4.30 also shows that the onset of the recovery in heat transfer is located more toward the inlet. This effect can be explained by considering the turbu-

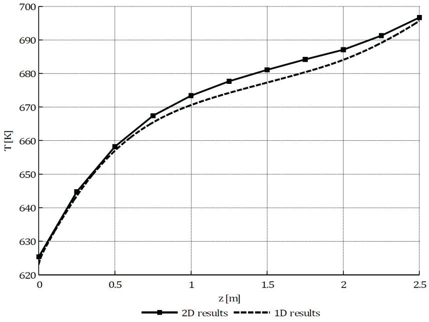

Figure 4.33: *Temperature as function of the pipe height for G = 200 kg/m^{2}s. The 2D results are averaged over the cross-section and the 1D-results are calculated on basis of heat transfer data from the 2D-simulations.*

lent kinetic energy shown in Fig. 4.32. Compared to the graph in Fig. 4.16 with identical color scale, strong turbulent diffusion near the wall is observed lower in the pipe.

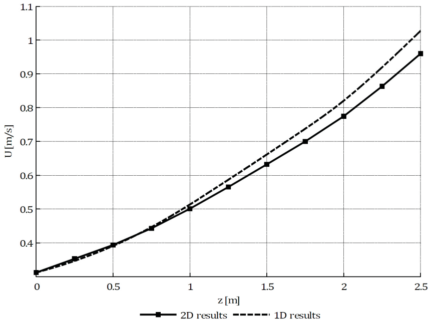

Figure 4.34: *Velocity as function of the pipe height for G= 200 kg/m^{2}s. The 2D results are averaged over the cross-section and the 1D-results are calculated on basis of heat transfer data from the 2D-simulations.*

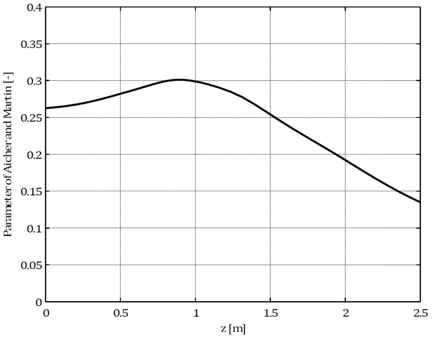

Figure 4.35: *Parameter of Aicher and Martin [5] as function of the pipe height for $G = 200$ kg/m^{2}s. The parameter is calculated using the 1D-model on basis of heat transfer data from the 2D-simulations.*

4.10 Comparison of 1D and 2D-simulation results

The results of the 1D-model have been compared with averaged quantities over the cross-section as obtained with the 2D-model, for the case presented in Table 4.2 and a numerical grid of 700,717 elements. First, the results are compared when the heat transfer coefficient data from the 2D-simulation is

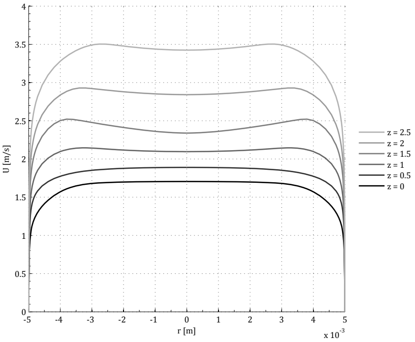

Figure 4.36: *Velocity profiles taken at different pipe heights for non-reacting flow with a mass flux of 1000 kg/m^{2}s.*

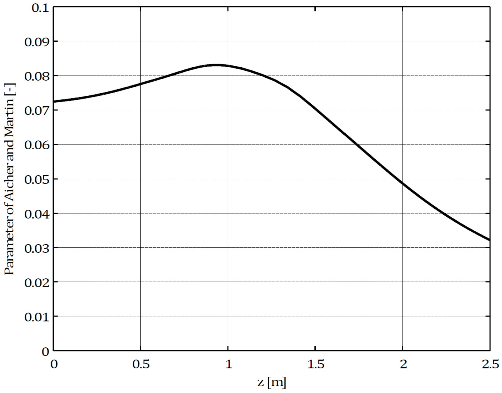

Figure 4.37: *Parameter of Aicher and Martin [5] as function of the pipe height for* $G = 1000\ kg/m^2s$. *The parameter is calculated using the 1D-model on basis of heat transfer data from the 2D-simulations.*

directly used for the 1D-calculations. This way, deviations due to mismatching heat transfer predictions by a Nusselt correlation from literature are excluded. The comparison will hence give a good indication for the loss of accuracy when neglecting 2D-effects in the model equations. Subsequently, the 1D results on basis of the Nusselt correlations from literature are compared to assess which of them is most suitable for the case that is studied. In Section 4.10.2, the 1D results for reacting flow, based on the most suitable Nusselt correlation from literature, are compared to the 2D results and to the non-reacting flow results of both models.

4.10.1 Comparison for non-reacting flow

Fig. 4.33 shows the temperature results for both models in case the Nusselt correlation in the 1D-model is replaced by heat transfer coefficient data from the 2D-solution. Here the heat transfer coefficient as function of the pipe height has been calculated according to Eq. 4.27. In fact, the Nusselt correlation is now ideal for the simulated case. The deviations between the lines seen in Fig. 4.33 are therefore mainly caused by the simplifications applied to the governing equations to arrive at the 1D-model equations described in Section 3.2.2.

With a maximum temperature difference of about 5 K, the loss of accuracy is quite limited.

The velocity plot in Fig. 4.34 shows a very reasonable correspondence between the two models as well. However, the 1D-calculations seem to be unsuitable for very long pipes because the deviation increases with the pipe height.

The coupling of the 1D-model equations with heat transfer data from the 2D results gives the opportunity to investigate the influence of buoyancy forces on the flow according to the 2D-simulations. The contribution of free convection to the heat transfer is characterized by the parameter of Aicher and Martin [5], defined by Eq. 3.36. The value of this parameter as function of the pipe height is shown in Fig. 4.35. When the values are compared with Fig. 3.5(a) for aiding flow, it can be seen that the flow is mainly driven by free convection. The decrease of the parameter value toward the outlet is caused by acceleration of the bulk flow. These observations are in accordance with the velocity profiles shown in Fig. 4.10.

The same analysis has also been performed for a mass flux of 1000 kg/m^{2}s to verify the relation between the velocity profiles and the buoyancy forces according to the parameter of Aicher and Martin [5]. In Fig. 4.36, it can be seen

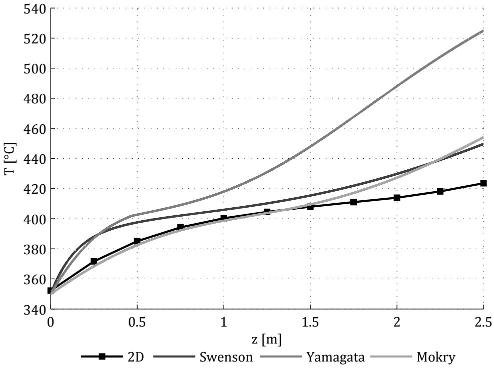

Figure 4.38: *Temperature as function of the pipe height for G = 200 kg/m^{2}s. The 2D results are averaged over the cross-section and the 1D-results are calculated on basis of different Nusselt correlations from literature.*

that the velocity profiles for this mass flux are far less deformed by buoyancy effects than is the case in Fig. 4.10 for $G = 200 \mathrm{kg/m^2s}$.

On basis of the velocity profiles shown in Fig. 4.36, it is expected that the heat transfer is mainly driven by forced convection. This flow classification has been confirmed by the parameter of Aicher and Martin [5] after loading the heat transfer coefficient as calculated by the 2D-model into the 1D-model. Fig. 4.37 shows that the parameter values are below 0.1, which indicates that forced convection is the dominant heat transfer mechanism according to Fig. 3.5(a).

When the Nusselt correlations from literature are used, the results for the two models are given in Fig. 4.38. The plot shows that the correlations that were derived for other pipe diameters than 10 mm (Bishop et al. [139] and Aicher and Martin [5]) lead to temperatures that do not correspond with the 2D results. The temperature of the fluid is much better described if the correlation of Mokry et al. [83] or Swenson et al. [107] is used, which were derived for pipes with similar geometry as used in the simulations. Although the correlation of Yamagata et al. [133] was also obtained from measurements on a 10 mm pipe, the agreement is much worse. This may be explained by the fact that the mea-

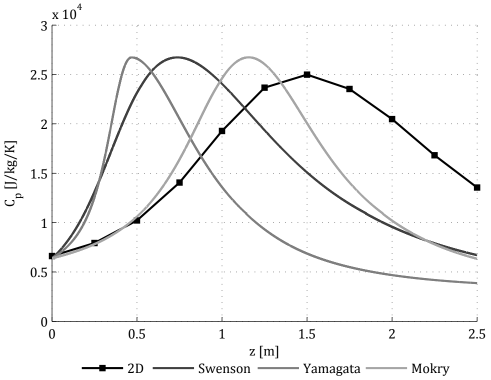

Figure 4.39: *Isobaric heat capacity as function of the pipe height for $G = 200$ kg/m^{2}s. The 2D results are averaged over the cross-section and the 1D results are calculated on basis of different Nusselt correlations from literature.*

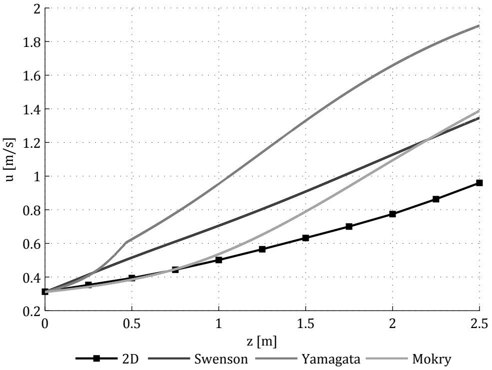

Figure 4.40: *Velocity as function of the pipe height for G = 200 kg/m^{2}s. The 2D results are averaged over the cross-section and the 1D results are calculated on basis of different Nusselt correlations from literature.*

surements showing heat transfer deterioration were excluded from the dataset used to derive the correlation. The line for the Mokry et al. [83] correlation shows a very close match until the bulk flow passes the pseudo-critical point after 1.5 m. The length required for the phase transition of the bulk according to the 1D-model is shorter, which implies that the heat transfer as predicted by the Nusselt correlation is higher.

The lines indicating the isobaric heat capacity in Fig. 4.39 confirm that the predicted heat transfer coefficient by the correlation of Mokry et al. [83] is closest to the results of the 2D-model. The shape of the curve is however best predicted by Swenson et al. [107].

The location of the phase transition is represented by an increase of the fluid velocity shown in Fig. 4.40. All correlations predict the phase transition in the bulk to occur earlier in the pipe and faster. As a consequence, the acceleration of the flow starts earlier and the slope of the lines is higher. Over the second half of the pipe, none of the lines resulting from the 1D calculations matches the 2D results satisfactorily.

From the figures presented in this section, it follows that the correlation of Mokry et al. [83] gives the best results for the first section of the pipe and then

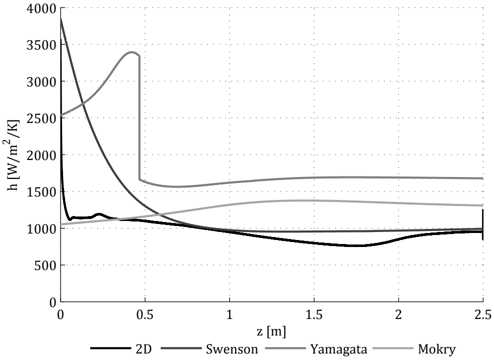

Figure 4.41: *Heat transfer coefficient as function of the pipe height for G = 200 kg/m^{2}s. The 2D results are averaged over the cross-section and the 1D results are calculated on basis of different Nusselt correlations from literature.*

Swenson et al. [107] gives better predictions for the remaining pipe length. In Fig. 4.41 it can be seen that the heat flux of the 2D-model would indeed be best approximated by using a combination of those two Nusselt correlations. However, the incapability of the individual correlations to predict the heat transfer

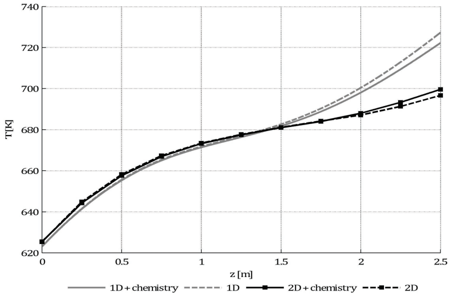

Figure 4.42: *Mean temperature as function of the pipe height for reacting and non-reacting flow using the Nusselt correlation of Mokry et al. [83].*

coefficient accurately over the entire pipe length makes the 1D-model unsuitable as a modeling tool for gasification in supercritical water.

4.10.2 Comparison for reacting flow

In this section, results of the 2D-model are compared with the 1D solution that is based on the Nusselt correlation of Mokry et al. [83]. Starting with the temperature plot in Fig. 4.42, it can be seen that the 1D-model predicts a reduction in temperature due to the chemical reactions, whereas the 2D-model shows a temperature increase. In Section 4.9.3, the improved heat transfer as predicted by the 2D-model is attributed to hydrogen production in the boundary layer and turbulence. These effects are not included in the 1D-model, which explains the contradictory predictions. The good match of the temperature profiles for reacting flow shown in Fig. 4.42 is coincidental, but relevant for interpreting the mass fraction plot in Fig. 4.43.

The mass fraction of methanol as function of the pipe height is compared in Fig. 4.43. The rather large deviation between the two lines is partly caused by the temperature differences seen in Fig. 4.42, but there is also a more fundamental problem. The plug-flow approach is not able to capture the high gradients in the temperature profiles near the wall, while the conversion rate increases exponentially with temperature. As a result, the mean fluid temper-

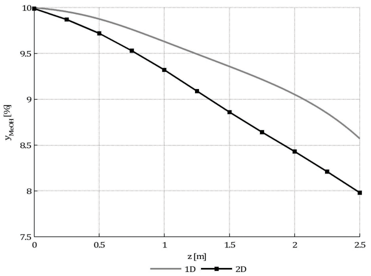

Figure 4.43: *Mean mass fraction as function of the pipe height for reacting and non-reacting flow using the Nusselt correlation of Mokry et al. [83].*

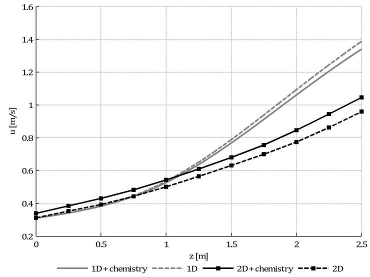

Figure 4.44: *Mean velocity as function of the pipe height for reacting and non-reacting flow using the Nusselt correlation of Mokry et al. [83].*

ature as calculated with the 1D model leads to an underestimation of the conversion rate. For this reason, the 1D-model is not able to describe the chemically reacting flow, even if the heat transfer would be predicted very accurately.

The deviations in temperature and conversion rate are summed up in the velocity plot in Fig. 4.44. Higher temperatures due to improved heat transfer and higher reaction rates both lead to acceleration of the flow. The graph shows that the difference between reacting and non-reacting flow is indeed much larger according to the 2D-model.

4.11 Conclusions

The simulations in a two-dimensional domain have been performed using the low-Reynolds k-ϵ model and the IAPWS-IF97 formulation. Using the simulation results it is clearly visible at which position the phase transition to supercritical water takes place in the geometry, since the isobaric heat capacity reaches a maximum at the pseudo-critical point. An interesting feature of the phase transition is that the pseudo-critical point is reached in a thin layer that sticks close to the wall over a long distance, separating gaseous supercritical water adjacent to the wall from the liquid bulk flow at sub-critical temperatures. The pseudo-critical region acts like a heat sink due to the high heat capacity, which causes the temperature to rise slowly. Furthermore, less heat is transported from the wall through the supercritical region to the bulk flow due to the steep decrease in conductivity in the proximity of the critical point. The fluid is accelerated in the pseudo-critical regions due to buoyancy forces and volumetric expansion. The increased velocity near the wall in the lower half of the pipe causes suction of fluid from the bulk flow toward the wall. This results in non-uniform velocity profiles over the radius.

A comparison of the critical heat flux from the 2D-simulations with empirical correlations from literature show that pseudo-flm boiling occurs for the $G = 200$ kg/m^{2}s case. Pseudo-film boiling could be a cause of deterioration of the heat transfer, and should therefore be avoided if possible. The good agreement of the critical heat flux as obtained from the 2D-simulations with the empirical correlations from literature is a confirmation that the 2D-model is able to predict the occurrence of pseudo-film boiling.

The occurrence of pseudo-film boiling results in the effect that a higher temperature difference between the wall and the bulk temperature leads to an increase in heat flux, but at the same time leads to a less efficient heat transfer regime. The results of the heat transfer calculations for the chosen flow conditions point out that pseudo-film boiling occur when the critical heat flux is exceeded. The critical heat flux for the onset of this effect is well described by the correlations of Yamagata et al. [133] and Mokry et al. [83]. Heat transfer deterioration is observed over a large part of the heated pipe section, which can be associated with the localized peak in heat capacity and growing low-density layer. Pseudo-film boiling can be suppressed by increasing the turbulence near the boundary layer or by limiting the temperature difference between the wall and the fluid. The heat transfer partly recovers once the bulk flow has passed the pseudo-critical point. According to the numerical results, the recovery is caused by increased turbulence production near the wall. These findings are in agreement with the phenomena described in literature.

The 2D-model results have been compared with results from a 1D-model using several Nusselt correlations from literature. It is clear that the results do not correspond well when a Nusselt correlation is used which is derived for a pipe flow in a different pipe diameter. Nusselt correlations derived for a pipe flow with the same pipe diameter show a better comparison. However, each individual Nusselt correlation from literature shows an incapability to predict the heat transfer coefficient accurately over the entire pipe length. Therefore it can be concluded that 1D-models should not be used to simulate the heat transfer to supercritical water in long or complex pipe configurations.

On basis of the 2D-model results, heat transfer to the reacting flow has been found to be more effective than to the non-reacting flow. The considerable improvement of heat transfer is mainly due to the production of hydrogen in the hot boundary layer, which has a positive effect on the local thermal conductivity. The chemistry of biomass conversion should however be included in more detail for a more realistic simulation of the reacting flow.

5

High troughput screening reactor for wet biomass

Supercritical water gasification is a promising process for the conversion of wet biomass into a combustible gas that is rich in hydrogen and methane. A novel experimental method is developed to investigate supercritical gasification in a fast and efficient manner for different process conditions and different types of biomass. An Inconel 625 autoclave reactor is extended with a high-pressure biomass injection system. The high-pressure injection system allows a wet biomass slurry to be injected into the autoclave reactor once the reactor is at supercritical temperature. The wet biomass slurry is heated up rapidly and the evaporation of the water present in the slurry results in a supercritical pressure. This will prevent the occurrence of sub-critical reactions taking place during the heating period of the mixture in the autoclave reactor. In this way, the reactor is very well suited for the research on gasification of wet biomass. Results of measurements for methanol and micro-algae have shown that the technique is suitable for screening purposes, including trend analysis.

5.1 Introduction

Towards an entirely new national energy system based on renewable sources, the Dutch government currently aims at 16% renewable energy in 2020. The goal for 2050 is a Dutch energy system completely based on renewable energy sources. Biomass will play an important role in this transition. Wet biomass is a renewable resource that currently is difficult to use in an efficient way. The high water content in feedstocks such as food waste, sewage sludge, rice husk or algae prevents the use of thermo-chemical conversion processes such as pyrolysis or thermal gasification. The required energy to evaporate the water before converting the organics into useful products makes the process uneconomic. Above the critical pressure (221 bar) at a temperature larger than 374°C, the biomass slurry changes from the liquid phase directly to the supercritical phase. An advantage of using supercritical conditions is that organic material is completely miscible with supercritical water, resulting in a homogeneous reaction phase. The high-pressure product gas allows for a more efficient heat transfer, so a large part of the heat of the product gas can be used to preheat the biomass slurry. The properties of supercritical water, such as density, viscosity, dielectric constant, and hydrogen bonding are different from liquid water or steam. In the process of supercritical gasification of biomass, the supercritical water fulfills every possible role it is able to fulfill: it is solvent, catalyst and reactant [59]. Because of the special properties of supercritical water, the expensive conventional drying step for wet biomass is not required. To prevent the costly drying step it is essential that the water does not leave the system as steam, the heat contained in the water can than be recovered in a later stadium.

Several bench-scale reactors are already in use to evaluate the process of supercritical gasification of wet biomass [12, 132]. The first proof of principle for biomass gasification in supercritical water was given by the work of Modell et al. [81]. In a later stage of SCWG research, many biomass compounds were tested in supercritical water to investigate the reactions taking place [8, 10, 11, 13, 28, 82, 86, 87, 95, 113, 130, 131, 138]. A useful overview of the developments in the field of supercritical gasification of biomass can be found in Matsumura et al. [80] and Kruse [59]. From these articles it can be concluded that SCWG is a very promising process, but as the SCWG process at

600°C is still determined by chemical kinetics a lot of work remains to be done to understand the conversion process completely [59].

For a reliable reactor design, data on reaction kinetics obtained for well-defined conditions are needed. To improve the understanding of biomass gasification in supercritical water and to identify the optimal process conditions and possible process bottlenecks, an efficient experimental method is necessary to screen the operating window of SCWG. In order to do this a high throughput screening technique has been developed.

In this chapter, we describe the development and the first experimental work done on a new screening reactor concept for conversion rate measurements of SCWG. For this purpose an Inconel 625 autoclave reactor is extended with a high pressure biomass injection system. The high pressure injection system allows both liquid and solid biomass particles to be injected into the autoclave reactor when water inside the autoclave reactor is at supercritical conditions. This will prevent the occurrence of sub-critical reactions taking place during the heating period of the mixture inside the autoclave reactor.

5.2 Previous Work

Due to the severe operating conditions of supercritical gasification, the amount of experimental data available is scarce, and the range of conditions explored is narrow. On a laboratory scale, most of the reactors used are tubular flow reactors. The design of the majority of these flow reactors is based on the reactor designed by Antal et al. [9]. These flow reactors consist of a heating zone, a tube reactor and, sometimes a fixed catalytic bed [46, 48, 61, 68, 132, 138]. During the experiments a temperature profile occurs over the length of the system. Also, due to the strong temperature dependency of the properties of water in the vicinity of the critical point, it is difficult to estimate the residence time in each reactor zone. Hence, the data obtained in the flow reactors are extremely difficult to interpret.

A continuous stirred tank reactor was used for the investigation of biomass conversion in supercritical water by Kruse et al. [64, 65, 103]. Cold feedstock was supplied continuously into the reactor by the screw press, and rapidly heated, by mixing with the hot content of the reactor [85]. Parameters such as the total organic carbon content and the composition of the formed gas phase were used to describe the biomass degradation.

Several groups use a batch autoclave approach to examine the product yield and distribution for various feedstock materials, process conditions and catalyst formulations [61, 65, 81, 94]. The advantages of a batch reactor system are that the structure is simple, and it can be used for almost all biomass feedstocks.

For meaningful interpretation of gasification experiments, it is essential that the experimental conditions are constant with respect to space and time during each experimental run. This cannot be achieved in conventional autoclaves, because the heating time is large compared to the reaction time [85]. For biomass gasification in supercritical water, there are many reactions occurring during the sub-critical heat-up stage of an experiment in the batch reactor. Feedstock transformation appears to become significant before reaching 250°C although little gas formation occurs at these lower temperatures. Gas formation becomes significant above 300°C and, in the case of cellulose, can be essentially completed on reaching 380°C. This makes interpretation of the results difficult, if not impossible [46].

This research introduces a novel technique which overcomes the problem of a high heating time and the problem of determining the temperature, the pressure and the residence time. An autoclave batch reactor is extended with a high-pressure injection system. In this way it is possible to inject reactants once the reactor is at supercritical temperature. This accelerates the heating-up period and prevents the occurrence of sub-critical reactions. In-situ temperature and pressure measurements allow for a recording of the process conditions in the reactor during the gasification process.

5.3 Experimental Section

5.3.1 Reactants

Methanol as a model compound

Methanol is chosen as a model compound for preliminary tests in the reactor. Methanol is a well-known reactant under supercritical conditions. The overall gasification reactions for biomass are described below [28]:

- Steam reforming:

$$C_xH_yO_x+(2x-z)H_2O \Rightarrow xCO_2+(y/2+2x-z)H_2 \qquad (5.1)$$

- Water gas shift reaction:

$$CO+H_2O \Leftrightarrow CO_2+H_2 \qquad (5.2)$$

- Methanation of CO:

$$CO+3H_2 \Rightarrow CH_4+H_2O \qquad (5.3)$$

Gasification of methanol is tested at several temperatures from 450 to 700°C, and the results are presented in Section 5.4.1.

Chlorella Vulgaris micro-algae

Algae represent a promising feedstock for supercritical gasification, and the feasibility of the use of this fuel is tested by performing a series of exploratory experiments. The same standard reaction conditions are used as for the methanol gasification described in the previous section. After injecting the algae and water, the pressure in the reactor is 260 bar and the temperature 600°C. The reaction time is longer than for the methanol experiments because of the slower conversion of the algae, and the tests were done for 60 minutes. The gasification of a real biomass compound is much more complicated than, for example, for methanol.

The actual reactions are not known for this complex feedstock, but based on the results with methanol it is unlikely that CH_4 is formed by CO methanation at 600°C. The chemical composition and other properties of the micro algae used are listed in Table 5.1. The results are presented in the following sections.

Table 5.1: *Analysis of the microalgae "Chlorella Vulgaris" (from supplier).*

Properties	
moisture content (wt%)	92.7
dry solid content (wt%)	7.3
Chemical composition (wt%)^{a,b}	
crude protein	50
crude fat	13
crude fiber	15
ash	7
Elemental composition of organic (wt%)	
C	45.8
H	7.9
N	7.5
O^{c}	38.7
Mineral content (g/kg)^{a,b}	
Ca	43
P	12.9
Na	1.1
K	7.1
Mg	6.1
Total amino acids (mg/kg)^{a}	246.2

[a] As given by supplier. [b] On a solid basis.
[c] Calculated by difference.

5.3.2 Experimental setup

A schematic diagram of the batch reactor used for gasification is shown in Fig. 5.1. The experimental setup consists of a 19.6 mm Inconel 625 reactor. The reactor is heated in a temperature-controlled fluidized bed oven. The upper

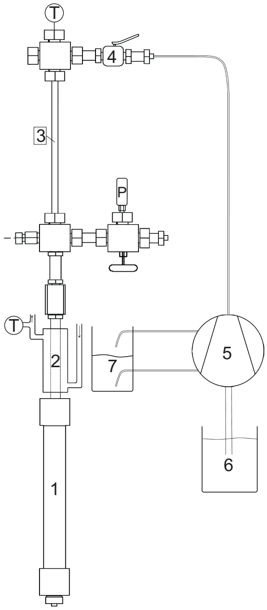

Figure 5.1: *Schematic overview of the experimental setup. 1-reactor; 2-actively cooled nipple; 3-sample volume; 4-ball valve; 5-HPLC pump; 6-water; 7-self flush; T-thermocouple; P-pressure inducer.*

part of the reactor is actively cooled using water at ambient temperature. The upper part is used for connecting the thermocouple and pressure transducer to the hot reactor volume. This part also acts as a sample volume in which the reactants are stored before the test. After the reactor is heated up to process temperature, a high-performance liquid chromatography (HPLC) pump is used to inject the reactants into the heated reactor.

5.3.3 Methodology

The reactor is heated up in a fluidized sand bed, located in a temperature controlled oven. The temperature inside the oven and the fluidized bed are measured using thermocouples which are monitored using Windmill software. Af-

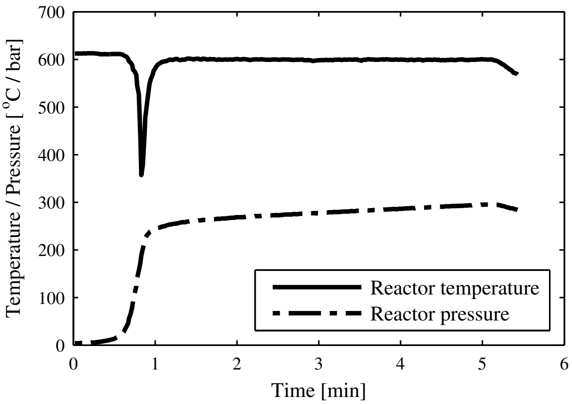

Figure 5.2: *Temperature and pressure during an experiment.*

ter the reactor is heated up to process temperature, the HPLC pump is started to inject the reactants into the reactor. After injection, the reactants will vaporize immediately and start reacting, as can be seen in Fig. 5.2. The oven is controlled and monitored using a Eurotherm control system. Once the reactions have taken place, the reactor is quenched using a combination of a fluidized sand bed and a water bath both at ambient conditions; this is done to make sure that no further reactions take place. After the quenching, the gases are collected in a gas sample bag and analyzed using a C2V-200 micro gas chromatograph (GC).

5.3.4 Analysis

The dry matter content of the algae slurry received was determined by drying at 105°C in an oven, and was found to be 7.3 wt%. The ultimate analysis of the dry and wet algae slurry was carried out using an Elemental Analyzer (EA 1108, CHNS-O, Fisons instruments) [28].

Gas analysis was carried out using two parallel C2V-200 gas chromatographs using TCD cells. One gas chromatograph (GC) is operated with a molecular sieve column and argon as a carrier gas for its good hydrogen sensitivity.

The other GC uses a plot U column with helium as the carrier gas. The chromatograms were obtained and interpreted using C2V 4.6 software.

5.3.5 Data interpretation

The degree of conversion of carbon in biomass to permanent gases (carbon efficiency, X_c) is chosen here as the main process parameter for evaluating the SCWG process, because it indicates the distribution of carbon over the desired products (permanent gases) and the undesirable product (liquids and polymers). X_c is defined by:

$$X_c = \frac{N_{c,\text{product gas}}}{N_{c,\text{feed}}} \tag{5.4}$$

The number of moles produced in the batch reactor are calculated from the known volume of the reactor and the measured temperature and pressure insitu of the reactor. Elemental analysis is used to determine the moles in the feed stream of the algae experiments.

5.4 Experimental Results

5.4.1 Methanol Results

To investigate the influence of the gasification temperature on the product gas yield and the gasification efficiency for the supercritical gasification of methanol, a series of gasification experiments were conducted at various temperatures between 460 and 700°C, a residence time of 15 minutes and a pressure of 260 bar after injection.

As can be seen in Figs. 5.3 and 5.4 , temperature has a significant influence on the gas yield and on the methanol conversion. The conversion increases from 9% at 460°C to 82% at a temperature of 700°C. Fig. 5.4 also shows the influence of the temperature on the yield of the product gases. The hydrogen yield increases from 0.25 moles per mole of methanol at low temperature to approximately 1.7 moles per mole of methanol at 700°C. When we assume that the gaseous hydrogen is solely produced from hydrogen in methanol, the

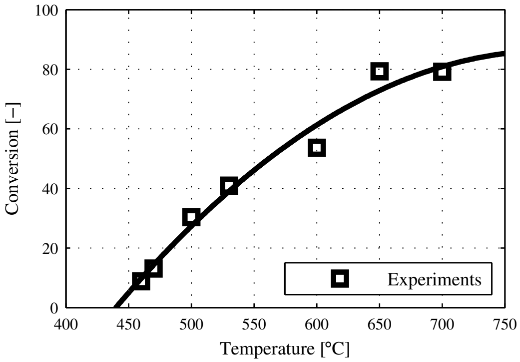

Figure 5.3: *Methanol conversion at different reactor temperatures. Using 10 wt% of methanol in water, at 260 bar and 15 minutes of reaction time.*

maximum theoretical hydrogen yield would be 2 moles per mole of methanol. However, in the case of this experiment, some of the hydrogen molecules are converted to methane. In reality, there is also hydrogen produced from water. It can be seen that the CO production is low for all reaction temperatures, since most of the carbon molecules are converted to CO_2. The methane production rate is at a maximum at 650°C but still quite low when compared to both CO_2

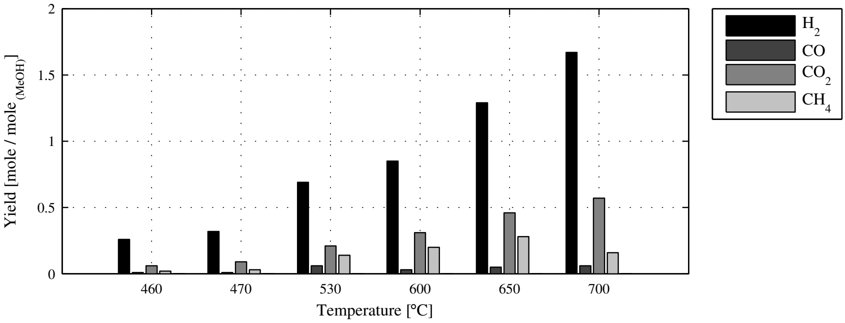

Figure 5.4: *Product yield at different reactor temperatures. Using 10 wt% of methanol in water, starting at 260 bar and 15 minutes of reaction time.*

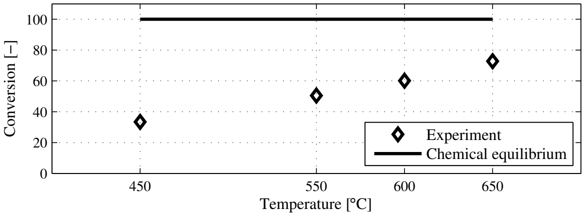

Figure 5.5: *Algae conversion at different reactor temperatures. Using 7.3 wt% of algae, at 240 bar and 1 hour of reaction time.*

and H_2.

5.4.2 Algae Results

The experiments with algae as a feed are performed at temperatures ranging from 450 to 650°C. The residence time was set at 60 minutes and the experiment started at 240 bar pressure after injection of the algae. With increasing temperature, the conversion rises from 33% at 450°C to 73% at 650°C, as can be seen in Fig. 5.5. In comparison with the methanol results, it can be seen that the product composition for the algae experiments contain some C2-C3

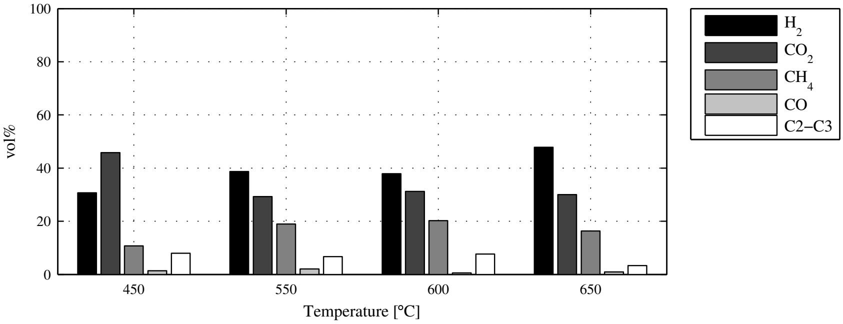

Figure 5.6: *Product gas composition at different reactor temperatures. Using 7.3 wt% of algae, at 240 bar and 1 hour of residence time.*

product gases. Ethane is prominent, together with small amounts of propane and ethylene.

From the results at different temperatures, it can be concluded that there is an increase both in hydrogen and methane production at higher temperatures. This is an unexpected result as chemical equilibrium calculations found in literature predict different behavior for product composition versus temperature [59]. In the case of chemical equilibrium, less methane is predicted to be produced at higher temperature. It can be seen in Fig. 5.6 that the CO production is low; there is a large amount of CO_2 produced and many different higher hydrocarbons. More experiments need to be conducted and the conversion rates of all experiments need to be investigated for a better understanding of the reaction mechanism for algae conversion.

5.5 Discussion

The reactor offers good temperature control and stable operation during experiments. The high-pressure injection of reactants allows for a drastically reduced heat-up time, while the use of a cold fluidized sand bed for cooling resulted in cooling the reactor from 600 to 100°C in less than a minute. Advantages of the technique include the feasibility of applying high temperatures and pressures, high corrosion resistance, rapid heating and cooling, and the in-situ continuous measurement of the process conditions.

As mentioned in the previous sections the problem of a high heating time is tackled in this research by extending an autoclave bath reactor with a high pressure injection system. The influence of the effect of the heating rate is investigated in detail by several other research groups. A summary of these studies can be found in Matsamura et al. [79]. The main problem of a high heating time is the occurrence of sub-critical reactions. Under sub-critical conditions, products with higher molecular weight are being formed via polymerization. These intermediate products are less reactive than the original feedstock at supercritical temperatures [59, 79]. In the present set-up, the addition of the high pressure injection system resulted in a reduction of the heating up time from 10 minutes to 20 seconds. In other words a large decrease in heating up time compared to the reaction time.

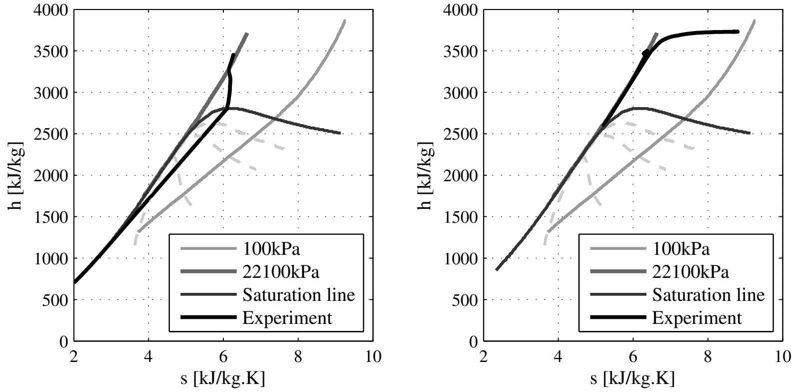

(a) Heating up path in the situation without an injection system, using water.

(b) Heating up path in the situation with an injection system, using water.

Figure 5.7: *Enthalpy entropy diagram.*

Another effect of the injection system apart from the reduction of residence time in the sub-critical region can be seen in Fig. 5.7. This figure shows the heating up trajectory of pure water without and with an injection system (Figs. 5.7(a) and 5.7(b) respectively). In the situation without an injection system the reactants are at atmospheric temperature and pressure when the experiment starts. Within ten minutes supercritical conditions are reached, hereby the reactants change from the liquid phase through the wet steam phase to a

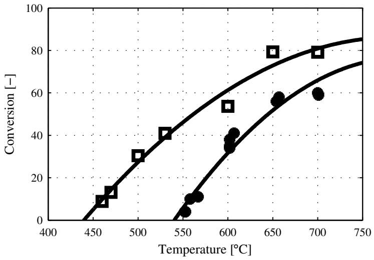

Figure 5.8: *Comparison of conversion with and without injection system.*

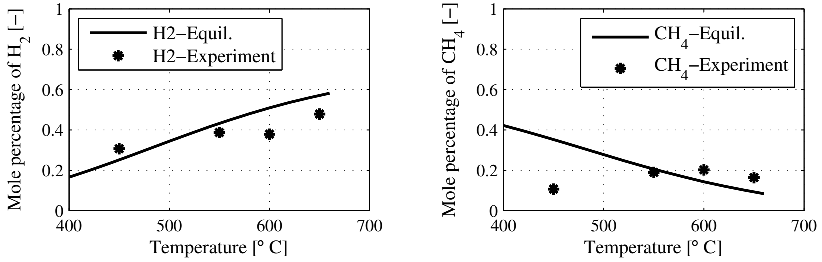

(a) H_2.

(b) CH_4.

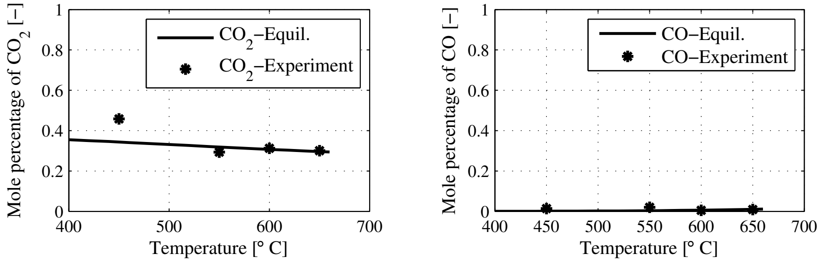

(c) CO_2.

(d) CO.

Figure 5.9: *Comparison of the product gas volumes as predicted by chemical equilibrium with the experimental values at different temperatures for algae gasification.*

superheated steam and eventually to the supercritical regime.

Fig. 5.7(b) shows the case where the reactants are injected in a reactor at supercritical temperature, in this case the reactants change from a superheated steam directly to the supercritical regime within a timespan of twenty seconds. Therefore the injection system drastically reduces the possibility of sub-critical reactions.

The strong reduction of the possibility of sub-critical reactions due to a short heating up trajectory should result in an improved conversion for the reactants in the supercritical reformer [59, 79]. Fig. 5.8 shows that indeed an improved conversion after the addition of the high pressure injection system can be noticed. It can be seen in Fig. 5.8 that even at high temperatures no complete conversion is reached for both cases. This can be explained by the stability of the methanol molecule as described by Di Leo and Savage [33].

As was done in Chapter 2 for methanol, equilibrium calculations for algae were performed according to the Gibbs free energy method. Fig. 5.9 shows the comparison of gas production obtained experimentally with the predicted equilibrium values. Looking at the production of CH_4, CO_2 and CO (Figs. 5.9(b), 5.9(c) and 5.9(d) respectively) the comparison looks reasonably well, especially at temperatures above 550°C. When compared to the other three product gases the production of H_2 does not compare well to the chemical equilibrium prediction at 600°C, but the comparison is acceptable for the temperatures of 450, 550 and 650°C as can be seen in Fig. 5.9(c). From the comparison between the numerical model predictions and the experimental results it can be concluded that the model fits the experimental data quite well, although it is noted that the conversion for the experiments increases from 33% at 450°C to 73% at 650°C, as can be seen in Fig. 5.5. While complete gasification is obtained for all chemical equilibrium calculations presented in Fig. 5.9.

5.6 Conclusions

A novel high-throughput batch reactor is developed and tested for the gasification of methanol and algae in supercritical water. An increase in both hydrogen yield and conversion degree is observed when the process temperature increases.

For the methanol case the temperature has a significant influence on both the gas yield and the methanol conversion. The conversion increases from 9% at 460°C to 82% at a temperature of 700°C. The hydrogen yield increases from 0.25 moles per mole of methanol at low temperature to approximately 1.7 moles per mole of methanol at 700°C. When a slurry of water and 7.3 wt% of micro-algae is used as a feedstock for supercritical gasification the conversion rises from 33% at 450°C to 73% at 650°C.

In the present study an autoclave reactor is extended with a high pressure injection system which allows the injection of both liquid and solid particles into the reactor under supercritical conditions. Due to the newly developed injection system the time of the heating up trajectory has decreased from ten minutes to twenty seconds, this results in an increase of the conversion over the complete temperature range. Due to a smaller possibility of sub-critical reactions the formation of less reactive intermediates is reduced.

6

Sorption enhanced reforming in supercritical water

In this chapter the possibility of in-situ CO_2*-capture in the gasification process is investigated. The so called 'sorption enhanced supercritical water gasification' (SE-SCWG) of wet biomass is evaluated and compared to conventional supercritical reforming. CaO, NaOH and hydrotalcite are tested as possible sorbents for sorption enhanced supercritical gasification. The evaluation is performed by both equilibrium calculations and experimental research.*

6.1 Introduction

Hydrogen is expected to play an important role as an energy carrier in the future. The amount of energy produced during hydrogen combustion is higher than released by any other fuel on a mass basis. In 2007 the annual production of H_2 worldwide was about 0.1 Gtonnes, of which 98% comes from reforming of fossil fuels [55, 78]. Green hydrogen could be made from biomass.

The goal of this project is to develop a process to produce hydrogen from wet biomass. The hydrogen could for example be used for electric power generation by fuel cells or as a feed for refineries. The advantage of biomass gasification in supercritical water is that the water is used as a reactant during the process. This prevents the energy consuming and costly drying step.

This chapter considers the process of sorption enhanced reforming of both methanol and micro-algae in supercritical water. Conventional reforming of methanol can be described by five overall reactions [23]:

$$CH_3OH \leftrightharpoons CO + 2H_2 \quad +91.7[\mathrm{kJ/mol}] \tag{6.1}$$

$$CO + H_2O \leftrightharpoons CO_2 + H_2 \quad -41[\mathrm{kJ/mol}] \tag{6.2}$$

$$CH_3OH + H_2O \leftrightharpoons CO_2 + 3H_2 \quad +50.7[\mathrm{kJ/mol}] \tag{6.3}$$

$$CO + 3H_2 \leftrightharpoons CH_4 + H_2O \quad -211[\mathrm{kJ/mol}] \tag{6.4}$$

$$CO_2 + 4H_2 \leftrightharpoons CH_4 + 2H_2O \quad -223[\mathrm{kJ/mol}] \tag{6.5}$$

Methanol steam reforming (Eq. 6.3) is the sum of the methanol decomposition reaction (Eq. 6.1) and the water-gas shift reaction (Eq. 6.2). The water-gas shift reaction is slightly exothermic, but reactions Eq. 6.1 and Eq. 6.3 are endothermic. The methanation reaction of CO (Eq. 6.4) and of CO_2 (Eq. 6.5) are both exothermic.

The thermodynamic equilibrium of Eq. 6.2 can be shifted to give more favorable H_2 yields by removing CO2. The concept is based on Le Chatelier's principle that (a) the conversion of reactants to products and (b) the rate of forward reaction in an equilibrium controlled reaction can be increased by selectively removing some of the reaction products from the reaction zone. When CO_2 is captured in-situ in the reactor the water-gas shift reaction is strongly influenced. The partial pressure of CO_2 on the right hand side of Eq. 6.2 decreases and the equilibrium moves to the right side, which results in a higher H_2 production. Several sorbents can be used to capture CO_2 during SCWG.

In this chapter conventional supercritical reforming is compared to sorbent enhanced reforming. CaO, NaOH and hydrotalcite are tested as possible sorbents for sorption enhanced SCWG. The comparison is performed by both equilibrium calculations and experimental tests.

6.2 Previous work

Since the early 1950s the equilibria and kinetics of CO_2 adsorption have been studied [34]. Most of these studies where done with CO_2 as the only adsorbate, at low temperature and at low pressure. Due to recent interest in CO_2 capture from flue gases and sorption enhanced steam methane reforming many studies on CO_2 sorbents have been carried out.

Previous work demonstrates the use of calcium based CO_2 sorbents for sorption enhanced steam methane reforming (SESMR) [16, 26, 45, 54, 91, 102]. SESMR is a method which combines steam methane reforming, the most widely used process for hydrogen production in industry, with CO_2 capture [129]. The most commonly used sorbent for SESMR is CaO. For example, Balasubramanian et al. [16] added CaO, formed by calcination of high purity $CaCO_3$, as a CO_2 acceptor to a commercial steam reforming catalyst producing $>95\%$ H_2 in a laboratory-scale fixed bed reactor.

When calcium oxide is used as a sorbent, the non catalytic highly exothermic carbonation reaction is included to the system of reactions:

$$CaO + CO_2 \longrightarrow CaCO_3 \quad \Delta H_{298K} = -178[\text{kJ/mol}] \tag{6.6}$$

$CaCO_3$ is cheap and readily available in nature [3] but it was reported that rapid sintering occurs with repeated carbonation-calcination cycles [2, 6]. Because of the high heat transfer rate combined with the relative low temperature of SE-SCWG compared to the process of SESMR the problem of sintering is expected to be less severe for SE-SCWG.

Alkali-salts are also interesting for the process of SE-SCWG because they can fulfill the role of both sorbent for CO_2 and they can act a as catalyst for the WGS reaction. Kruse at al. [66] have shown that alkali salts like potassium hydroxide (KOH) and potassium carbonate (K_2CO_3) promote the gasification of pyrocatechol in supercritical water even at a low temperature of 773 K. Watanabe et al. [121] show that NaOH is an effective sorbent for the gasification of both glucose and cellulose at a low temperature of supercritical water (i.e. 673 K). The H_2 yield of gasification of lignin in supercritical water proved to be almost 4 times higher in the presence of sodium hydroxide than when gasified without a sorbent [122]. Alkali salts are effective catalysts for the water-gas shift reaction [39, 62, 63]. In the presence of such salts, high hydrogen yields at reasonable reaction times are possible. A possible reaction path for CO_2 capture using NaOH could be:

$$2NaOH + CO_2 \longrightarrow Na_2CO_3 + H_2O \tag{6.7}$$

The use of hydrotalcite-based sorbents for CO_2 capture at high temperatures can be found in several studies [18, 35, 42, 69, 70, 90, 96]. Hydrotalcite belongs to the class of anionic clay minerals consisting of positively charged layers of metal oxide (or metal hydroxide) with inter-layers of anions, such as carbonate [34]. Exchange of the anionic layer can lead a wide range of catalytic and adsorptive properties, with particular stability under wet gas and high temperature conditions [20, 34, 49]. A detailed study on the mechanism of CO_2 sorption of hydrotalcite can be found in the work of Walspurger and co-workers [119]. These studies showed that hydrotalcite like compounds are one of the most promising adsorbents for sorption enhanced hydrogen production.

As can be found in literature CaO, NaOH and hydrotalcite are three of the most interesting sorbents available for SE-SCWG. In the following sections both numerical calculations and experimental tests are used to perform an evaluation of these sorbents.

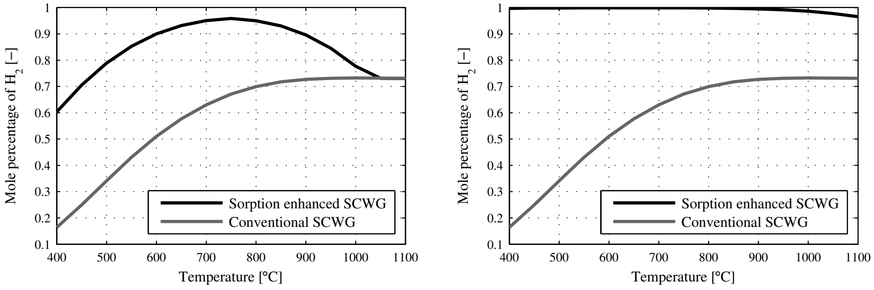

(a) CaO.

(b) NaOH.

Figure 6.1: *Equilibrium H_2 molar fraction (dry basis) in the product gas with and without a stoichiometric amount of sorbent. Results are plotted as a function of temperature at fixed pressure and steam to carbon ratio.*

6.3 Chemical equilibrium calculations

Supercritical water gasification (SCWG) of methanol is modeled using a chemical equilibrium calculation. Equilibrium calculations were performed using the Gibbs free energy method [67], combined with the Modified Soave Redlich Kwong equation of state [105]. Equilibrium H_2 molar fraction in the product gas on a dry basis is plotted in Fig. 6.1. This is done with and without CaO and NaOH as a CO_2 acceptor as a function of temperature at both fixed pressure (300 bar) and Steam to Carbon ratio (S/C = 16).

Fig. 6.1 shows that at a fixed pressure in the case of conventional SCWG of methanol the H_2 concentration increases at the temperature increment and reaches a maximum of 0.73 at 950°C.

In the case of sorption enhanced (SE) SCWG of methanol using CaO as a sorbent, the maximum volume percentage of H_2 is reached at 750°C (Fig. 6.1(a)). Above 850°C the calcination reaction (Eq. 6.8) starts which is the reverse reaction of the carbonation reaction (Eq. 6.6).

$$CaCO_3 \longrightarrow CaO + CO_2 \quad \Delta H_{298K} = +178[\text{kJ.mol}] \tag{6.8}$$

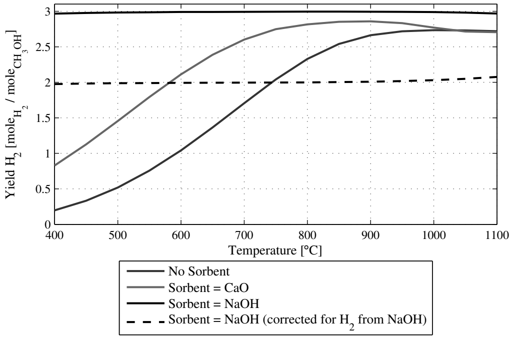

Figure 6.2: *H_2 yield per mole of CH_3OH at different temperatures.*

The $CaCO_3$ releases the CO_2 and therefore the volume percentage of H_2 in the dry product gas decreases. Similar results were obtained by Balasubramanian et al. [16] and Barelli et al. [17].

When NaOH is used as a CO_2 acceptor, the difference in H_2 production between SE-SCWG and conventional SCWG of methanol is even bigger. At temperatures below 950°C the mole percentage of H_2 is above 99%.

To give better insight in the amount of H_2 produced from methanol, the H_2 yield is plotted in Fig. 6.2. This figure depicts the H_2 yield per mole of CH_3OH for the cases with and without sorbent. For the case where NaOH is used as a sorbent also a corrected case for the H_2 formed by the H present in the NaOH is presented in the figure. The corrected case shows that for the temperature range presented the hydrogen yield is close to the theoretical maximum for CH_3OH reforming, this will be explained in more detail later on. Fig. 6.3 presents the yield of both CO_2 and H_2O.

It can be seen in Fig. 6.2 that when CaO is used as a sorbent the WGS reaction (Eq. 6.2) is strongly influenced by the presence of CaO. Because of the CO_2 capture the reaction is shifted in the direction of H_2, this results in a larger H_2-production and hence a larger H_2O consumption (Fig. 6.3(b)). As mentioned before the $CaCO_3$ releases CO_2 at temperatures above 850°C, this is shown in Fig. 6.3(a). This results in an extra H_2O reduction due to the formation of $Ca(OH)_2$ (Eq. 6.9):

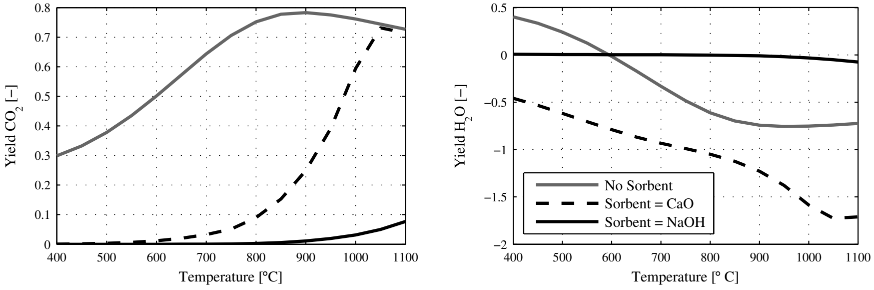

(a) CO_2 yield.

(b) H_2O yield.

Figure 6.3: *Yield of product gases per mole of CH_3OH at different temperatures*

$$CaO + H_2O \longrightarrow Ca(OH)_2 \quad \Delta H_{298K} = -109[\text{kJ.mol}] \tag{6.9}$$

Compared to the case with CaO as sorbent and the case without sorbent Fig. 6.3 shows that there is nearly no H_2O production or consumption when NaOH is used as a CO_2-acceptor. This can be explained by looking at Eq. 6.7, for every mole of CO_2 captured by the NaOH one mole of H_2O is formed. So even

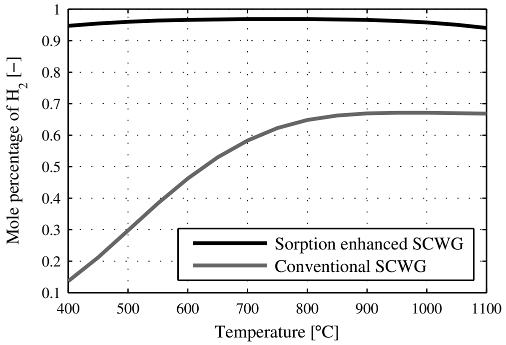

Figure 6.4: *H_2 mole percentage of dry product gas for the supercritical gasification of algae ($C_{3.81}H_{7.84}N_{0.54}O_{2.42}$) at different temperatures. NaOH is used for the sorbent case.*

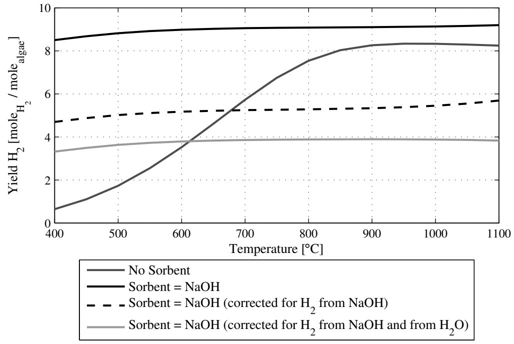

Figure 6.5: *H_2 yield per mole of algae $C_{3.81}H_{7.84}N_{0.54}O_{2.42}$) at different temperatures.*

though the WGS reaction (Eq. 6.2) is strongly shifted in the direction of H_2 and CO_2 this is not visible in the consumption of H_2O. When H_2O does not play a role in the reactions the theoretical yield of H_2 from the SCWG of CH_3OH is 2 moles of H_2 per mole of CH_3OH. As can be seen in Fig. 6.2 the theoretical yield is reached even at temperatures close to the critical temperature. When NaOH is added to the reactants almost all the gas present in the dry product gas is H_2, all the C molecules from the CH_3OH are captured in the form of Na_2CO_3.

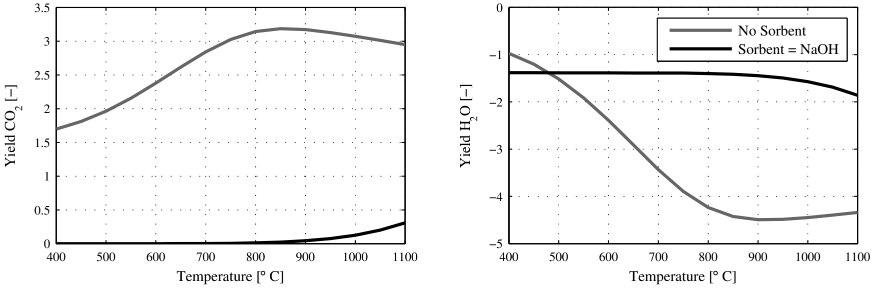

(a) CO_2 yield.

(b) H_2O yield.

Figure 6.6: *Yield of product gases per mole of algae ($C_{3.81}H_{7.84}N_{0.54}O_{2.42}$) at different temperatures.*

Fig. 6.4 shows the chemical equilibrium calculation results for the SCWG of a 7.3 wt% algae slurry with a composition as given in table 5.1. For the H_2 concentrations the results look very similar to the results as obtained for CH_3OH (Fig. 6.1(b)).

The H_2 yield from algae (Fig. 6.5) predicted by the model is quite different to the H_2 yield from CH_3OH (Fig. 6.2). This is due to the difference in ratio of C and H molecules of algae and methanol. Because of the higher carbon content of an algae molecule more moles of NaOH are necessary for a stoichiometric reaction, hence more H_2 is produced by the NaOH per molecule of algae, as can be seen in Fig. 6.5. When the H_2 yield is corrected for H_2 produced from NaOH and from H_2O, the H_2 yield is close to the theoretical limit of H_2 production per mole of algae.

When no sorbent is used for the SCWG of algae, the theoretical H_2-yield is exceeded for temperatures above 600°C, this is due to a high H_2O consumption as can be seen in Fig. 6.6(b). At temperatures close to the critical point the H_2O consumption and hence the H_2 production are low. When NaOH is used as a sorbent the thermodynamic model predicts a H_2 mole percentage of more than 99% even at temperatures slightly above the critical temperature.

From the equilibrium calculations it can be concluded that a large increase in H_2-production can be seen for both CaO or NaOH as CO_2-acceptor. The calculations show that the WGS reaction is strongly shifted in the direction of H_2 in the product gases for the case of SE-SCWG of methanol and algae.

6.4 Experimental results

The sorption enhanced gasification of biomass in supercritical water is tested in the autoclave batch reactor as described in Section 5.3.2. Testing was done using methanol as a model compound for biomass and micro-algae as a real biomass. Both hydrotalcite and NaOH are used as a sorbent and compared to the case when no sorbent is used. The experimental procedure is very similar to the procedure described in Section 5.3.3, with the main difference that the sorbents used for the experiment are added to the reactor before the reactor is heated up to process temperature.

Figs. 6.7, 6.8 and 6.9 show the yield of product gases for the supercritical gasification of methanol with and without sorbents. The gasification experiments were conducted at a pressure of 260 bar and at temperatures of 450°C, 500°C and 550°C respectively. Similar trends for the H_2 yield in the dry product gases are shown in the three figures, where the yield increases from 1 mole of H_2 per mole of methanol when no sorbent is used to 3 moles of H_2 when NaOH is used as a sorbent. For hydrotalcite also an increase in H_2 production can be seen, but not as strong as for NaOH. From these results it can be concluded that the influence of NaOH on the WGS-reaction is larger than that of hydrotalcite.

Figs. 6.7, 6.8 and 6.9 show that for hydrotalcite the production of CO_2 and H_2O is for all three temperatures lower than without sorbents. For NaOH as sorbent no production of CO2 and CH_4 can be noted. This could mean that all C molecules present in the methanol are captured in the form of Na_2CO_3 during the process.

Another interesting parameter for the process of sorption enhanced gasification of biomass in supercritical water is the conversion time. Fig. 6.10 shows that both sorbents have a very large influence on the conversion time. For hydrotalcite the conversion time decreases with 70% and for NaOH the conversion time decreases with 80%.

As mentioned in Chapter 2, biomass itself is a complicated mixture of organic

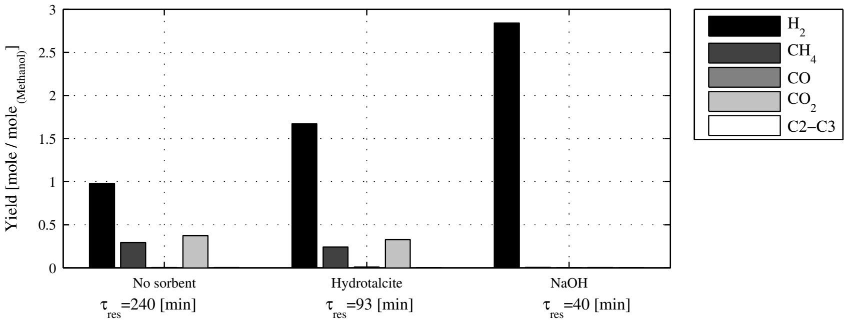

Figure 6.7: *Gas products yield of supercritical gasification of methanol with and without sorbents. Experiments done with 5wt% of methanol at a temperature of 450° C starting at a pressure of 260 bar.*

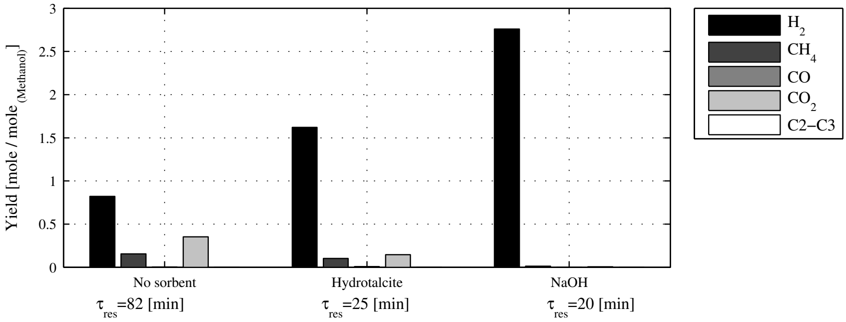

Figure 6.8: *Gas products yield of supercritical gasification of methanol with and without sorbents. Experiments done with 5wt% of methanol at a temperature of 500° C starting at a pressure of 260 bar.*

and inorganic components. In the results discussed so far only experiments with methanol as a biomass model compound have been shown. The next step is sorption enhanced gasification with a real biomass. In this research micro-algae were selected for investigation. Chlorella Vulgaris is chosen as the type of microalgae, the experimental results for micro-algae are presented in

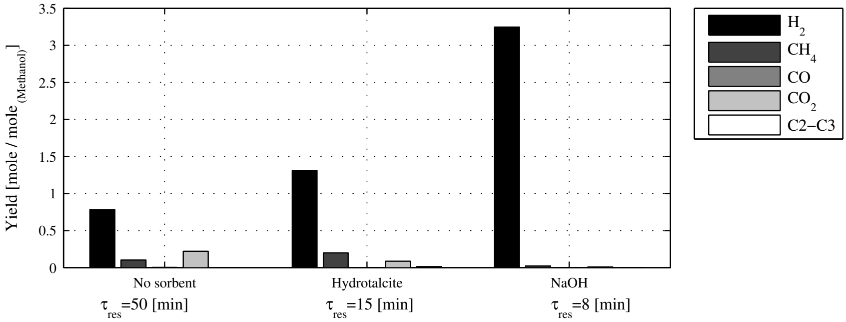

Figure 6.9: *Gas products yield of supercritical gasification of methanol with and without sorbents. Experiments done with 5wt% of methanol at a temperature of 550° C starting at a pressure of 260 bar.*

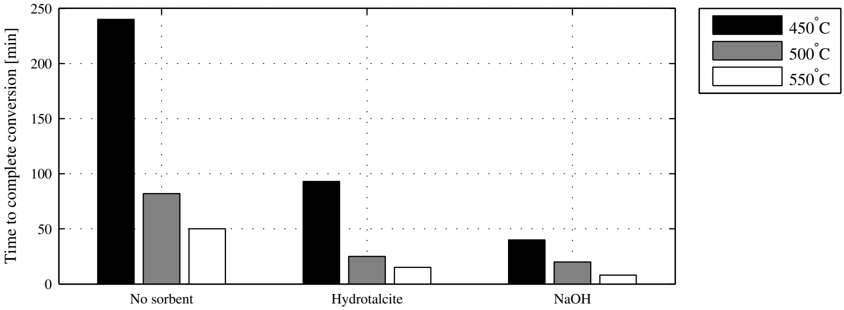

Figure 6.10: *Time till conversion for supercritical gasification of methanol with and without catalysts. Experiments done with 5wt% of methanol at three different temperatures starting at a pressure of 260 bar.*

Figs 6.11, 6.12 and 6.13. NaOH was chosen as the most effective type of sorbent based on the methanol results shown earlier. Similar trends can be seen for micro-algae. For all three temperatures (450, 500, and 550°C) a large increase in H_2 production in the dry product gases can be noted compared to the case without sorbents. The production of CH_4, CO_2 and C_2H_6 is reduced significantly when NaOH is added to the process.

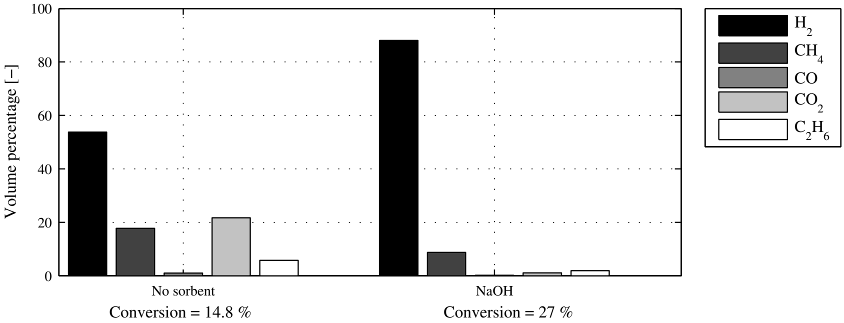

Figure 6.11: *Gas product concentration of supercritical gasification of algae with and without sorbents. Experiments done at a temperature of 500° C, a starting pressure of 260 bar and a residence time of 2 hours.*

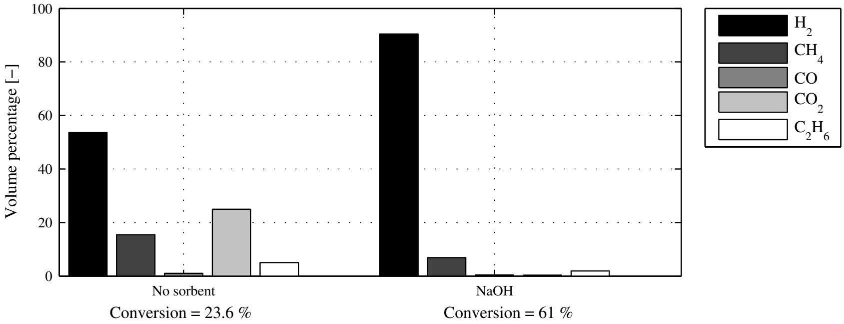

Figure 6.12: *Gas product concentration of supercritical gasification of algae with and without sorbents. Experiments done at a temperature of 550° C, a starting pressure of 260 bar and a residence time of 2 hours.*

It is noted that the conversion of algae during the supercritical gasification experiments presented in this section is much lower than the conversion for the experiments presented in Section 5.4.2. The experimental series for the results shown in Chapter 6 were conducted under the assumption that the algae had the same composition as the algae used in Section 5.3.1. When the re-

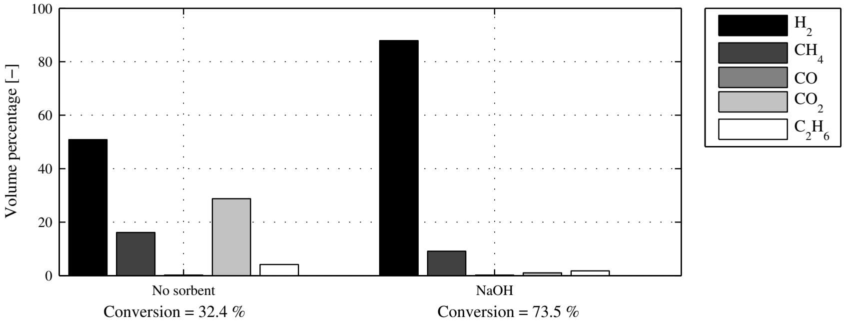

Figure 6.13: *Gas product concentration of supercritical gasification of algae with and without sorbents. Experiments done at a temperature of 600° C, a starting pressure of 260 bar and a residence time of 2 hours.*

sults presented here are compared to the results presented in Chapter 5 it may be clear that this was not the case. It is expected that the algae used in this chapter contain a higher amount of organics in the feed than the algae used in Chapter 5. Unfortunately no moisture data of the present data are available to verify this assumption. The conversions shown in Figs. 6.11, 6.12 and 6.13 were calculated under the assumption that the algae contained 7.3wt% of organics in the feed, which is similar to the algae used in Chapter 5. In order to obtain more detailed information it is recommended that the experiments are repeated. Nevertheless, the present series of experiments can be used to get more insight in the effects of CO_2 sorbents on the SCWG process.

When NaOH is added to the reactor a large improvement in the conversion degree can be seen. At all three process temperatures the gas efficiency more than doubles. The conversion plotted in Figs 6.11, 6.12 and 6.13 is based on the H-balance and is corrected for H_2 produced from NaOH and H_2O.

6.5 Discussion

When a CO_2 acceptor is added to the reactor, carbon dioxide is converted immediately to a solid carbonate, causing a shift in the reforming and WGS reactions beyond their conventional thermodynamic limits. From the perspective of hydrogen production both the numerical and the experimental results show that sorption enhanced gasification in supercritical water enables lower reaction temperatures, which may results in a reduction of sorbent sintering, while enabling the use of less expensive reactor wall materials. Most of the heat required by the endothermic reforming reactions will be supplied by the heat release of the exothermic carbonation reactions. But it must be considered that the largest challenge in terms of heat transfer and reactor construction will be caused by the heat required for the energy intensive calcination reaction which is essential for sorbent regeneration. Regeneration of the sorbent can be used for the release of pure CO_2 suitable for sequestration.

Research done for CaO sorption enhanced methane reforming showed that additional energy is needed to reverse the CO_2 capturing reaction [47]. Due to a lower process temperature a reduction of 20% to 25% in the overall energy requirement is estimated to be possible when compared to the standard reforming process [26, 91]. Ca-based sorbents show a decay in adsorption capacity as a function of the number of calcination-carbonation cycles [54]. For hydrotalcite and NaOH these numbers are not known, but a similar trend is expected. Abanades et al. [3] shows that synthetic sorbents (for example Li_2ZrO_3) have a better multi-cycle stability, but to compete with natural sorbents their cost would require them to sustain >10.000 cycles [54]. More information on the adsorption capacity and the chemical stability during carbonation/calcination cycles is needed for the used sorbents to qualify the optimal sorbent for sorption enhanced gasification of biomass in supercritical water.

The sorption enhanced gasification of methanol experiments result in a very low gas production of hydrocarbons and CO_2. It is expected that nearly all C-molecules present in the methanol are captured in the form of Na_2CO_3, hence maximum CO_2 capture is achieved. When algae are used as a biomass compound, the experimental results show a large reduction in CO_2 product gases when compared to the case when no sorbent is used. This combined with the increase in algae conversion leads to the conclusion that NaOH is an interesting additive for SCWG of biomass.

6.6 Conclusions

Thermodynamic calculations were done to model the process of sorption enhanced gasification in supercritical water. A large increase in H_2 production can be seen for both CaO or NaOH as CO_2-acceptor. The model predicts a H_2 mole percentage of more than 99% when NaOH is used as a sorbent, even at temperatures slightly above the critical temperature. The calculations show that the WGS reaction is strongly shifted in the direction of H_2 in the product gases for the case of SE-SCWG of methanol. For CaO as a sorbent additional H_2O consumption is noted, while for NaOH in no additional H_2O production or consumption can be seen.

Due to the difference in C/H ratio of algae and methanol, the yields predicted by the chemical equilibrium model for the sorption enhanced supercritical water gasification of algae and methanol differ. Due to the higher carbon content of algae more moles of NaOH per mole of algae are required for a stoichiometric reaction. Hence more H_2 is produced by the NaOH per mole of algae.

When the H_2 yield in the predicted product gases is corrected for the H_2 produced from the NaOH, the H_2 yield is very close to the theoretical limit of H_2 production from algae.

Sorption enhanced gasification of both methanol and micro-algae in supercritical water are experimentally tested in a high-throughput batch reactor. Hydrotalcite and NaOH were tested with methanol as a biomass model compound and micro-algae as a real biomass source. Especially the results for NaOH were promising with high production of H_2 and a large reduction in both conversion time and CO_2 in the dry product gases. For the algae case a large reduction in CO_2 production is shown in the experimental results. Even though algae are a difficult compound to convert completely to dry product gases, the conversion was more than doubled when NaOH was added to the process.

7

Conclusions and recommendations

The results from the present research have led to new insights and tools for a better design of supercritical gasification of wet biomass. The first section of this concluding chapter presents the answers to the research questions posed in Chapter 1. Finally in Section 7.2 various recommendations for both improving the results obtained and suggestions for follow up research are discussed.

7.1 Conclusions

Can gasification of wet biomass in supercritical water be designed as a thermally efficient process?
The gasification of biomass in supercritical water can be designed as a thermal efficient conversion process. A thermodynamic system model has been developed and calculations have been carried out with methanol/water solutions. The results obtained with the model show that the composition of the product gases can be tailored to a desired product composition by changing the key process parameters such as the reactor temperature, pressure or the concentration of organic material in the feed. High temperature, low pressure and a low methanol concentration result in a product gas consisting mainly of hydrogen. On the other side a concentrated methanol feed at high pressure and low temperature is converted mainly to methane. The higher the concentration of organics in the stream the higher the thermal efficiency, until it stabilizes at concentrations above 40 wt%.

The efficiency of the heat exchanger has a strong effect on the thermal efficiency of the system. This can be explained by the high heat capacity of water and the high water content of the feed stream. In this research it is shown that a small increase in the heat exchanger effectiveness has a strong impact on the overall thermal efficiency. A feed with 10 wt% of methanol shows an increase in thermal efficiency of 25% when the heat exchanger effectiveness is improved with 10%. Therefore an optimum design of the heat exchanger is required.

From the comparison between the process optimized for hydrogen production and the process optimized for methane production it can be concluded that from an energy perspective it is better to optimize the process for methane. The thermal efficiency for a feed with 10 wt% of methanol 48.5% and 40% for respectively a methane and a hydrogen system. For a feed with 30 wt% of 30 methanol the thermal efficiencies for methane and hydrogen are 87% and 84%, respectively. The difference is mainly caused by the fact that the methane optimized case has a much lower temperature than the hydrogen case, respectively 400 and 600°C. It is noted that the process optimized for methane at 600°C needs a catalyst for a good carbon efficiency.

The supercritical gasification process has the possibility of in-situ capturing CO_2 in the water phase. For a case of 10 wt% of methanol in water at 600°C and 300 bar, 40% of the CO_2 present in the product gases can be captured using the water present in the system. The process water can be recycled to absorb more CO_2, but this comes at the expense of the thermal efficiency. A feed with 5 wt% of methanol shows a decrease of 20% in thermal efficiency when the CO_2 capture efficiency is improved with 20%, this is due to an increase in dissolved H_2 and CH_4.

What is the influence of the large property variations of water, in the transition from sub- to supercritical water, on the heat transfer in the SCWG process?
The property variations of water in the vicinity of the (pseudo-)critical point significantly influence the heat transfer. Depending on the flow conditions, the variations in fluid properties can result in heat transfer enhancement or deterioration.

For the design of efficient heat exchangers more knowledge is required on heat transfer in supercritical water. In the present study, heat transfer from the wall to supercritical water has been modeled in a one-dimensional domain by use of a plug flow approach. Nusselt correlations are required for prediction of the heat transfer coefficient in order to close the set of equations. The experimental validation for three different cases show that the model is able to accurately predict the bulk temperature based on heat transfer rates provided by a suitable Nusselt correlation.

However, the results also give reason to assume that the Nusselt correlations are very specific for the flow conditions of the experiments from which the Nusselt correlations were derived. Nusselt correlations that are valid for similar operating conditions, and have to be chosen a priori to close the 1D-model equations, do not necessarily give similar results. The large deviations between the predictive capability of the Nusselt correlations leads to the conclusion that it is important to consider boiling effects that occur when a critical heat flux is reached. The right choice of the Nusselt correlation for the simulated case is crucial for the quality of the 1D-model.

Simulations in a two-dimensional domain have been performed using the low-Reynolds k-ϵ model and the IAPWS-IF97 formulation. The simulation results clearly show at which position the phase transition to supercritical water takes place. An interesting feature of the phase transition for the case under investigation is that the critical point is reached in a thin layer that sticks close to the wall. The phase transition separates the gaseous supercritical water adjacent to the wall from the liquid bulk flow at sub-critical temperatures. This causes the temperature to rise slowly due to the high heat capacity and a steep decrease in conductivity of water in the proximity of the critical point.

The critical heat flux is a good indicator for the occurrence of pseudo-film boiling. When the critical heat flux obtained by the 2D-model is compared to the critical heat flux calculated with empirical correlations from literature, it can be concluded that the 2D-model is capable of predicting the occurrence of pseudo-film boiling. This is an important feature of the model as pseudo-film boiling is a cause for the detoriation of the heat transfer.

In order to validate the 2D-simulations, fluid temperatures of a supercritical water flow during heat up have been successfully measured using a new experimental setup. The comparison of the temperature results show a good agreement between the experimental data and the numerical predictions. When the temperature error is calculated on a °C basis, the maximum error between the experimental and numerical data for the $G = 6.6$ kg/m^2·s case is 11%, and for the $G = 10$ kg/m^2·s case the maximum error is 7%.

The 2D-model results have been compared with results from the 1D-model using several Nusselt correlations from literature. Each individual Nusselt correlation shows an incapability to predict the heat transfer coefficient accurately over the entire pipe length. Therefore it can be concluded that 1D-models should not be used to simulate the heat transfer to supercritical water in long or complex pipe configurations.

For both the 1D-model and the 2D-model the effect of the methanol decomposition reaction on the heat transfer has been investigated. Due to the plug flow assumption of the 1D-model, the model is not capable of capturing the high temperature gradients in radial direction, which leads to an underestimation of the conversion rate. The 2D-model is more suitable for predicting chemically reacting flow. From the 2D-model results the heat transfer to a reacting flow is larger than heat transfer to a non-reacting flow. The improvement of the heat transfer is caused by the production of hydrogen in the hot boundary layer, and hydrogen has a positive effect on the local thermal conductivity. Another contributing effect to the heat transfer is the increase in the turbulent kinetic energy near the wall for the case of reacting flow.

Is it possible to gasify wet biomass such as algae in supercritical water?
It is possible to gasify wet biomass such as algae in supercritical water. A novel high-throughput batch reactor is developed and tested for the gasification of methanol and algae in supercritical water. An increase in both hydrogen yield and conversion degree is observed when the process temperature increases.

For the methanol case the temperature has a significant influence on both the gas yield and the methanol conversion. The conversion increases from 9% at 460°C to 82% at a temperature of 700°C. The hydrogen yield increases from 0.25 moles per mole of methanol at low temperature to approximately 1.7 moles per mole of methanol at 700°C. When a slurry of water and 7.3 wt% of micro-algae is used as a feedstock for supercritical gasification the conversion rises from 33% at 450°C to 73% at 650°C.

In the present study an autoclave reactor is extended with a high pressure injection system which allows the injection of both liquid and solid particles into the reactor under supercritical conditions. Due to the newly developed injection system the time of the heating up trajectory has decreased from ten minutes to twenty seconds, this results in an increase of the conversion over the complete temperature range. Due to a smaller possibility of sub-critical reactions the formation of less reactive intermediates is reduced.

Does the SCWG process allow for in-situ capturing of CO_2 during the process?
The supercritical gasification process has the possibility of in-situ capturing CO_2. This can be achieved either by the capturing of CO_2 in the water phase or by using a CO_2-sorbent.

Thermodynamic calculations were done to model the process of sorption enhanced gasification in supercritical water. A large increase in H_2 production can be seen for both CaO or NaOH as a CO_2-acceptor. The model predicts a H_2 mole percentage of more than 99% when NaOH is used as a sorbent, even at temperatures slightly above the critical temperature. The calculations show that the WGS reaction is strongly shifted in the direction of H_2 in the product gases for the case of SE-SCWG of methanol.

Due to the higher carbon content of algae more moles of NaOH per mole of algae are required for a stoichiometric reaction. Hence more H_2 is produced by the NaOH per mole of algae. When the H_2 yield in the predicted product gases is corrected for the H_2 produced from the NaOH, the H_2 yield is 4 moles of H_2 per mole of algae. This is approximately the theoretical limit of H_2 production for the sorbent enhanced gasification of a slurry with 7.3wt% of algae.

Sorption enhanced gasification of both methanol and micro-algae in supercritical water are experimentally tested in the high-throughput batch reactor. Especially the results with NaOH as a sorbent are promising with high production of H_2 and a large reduction in both conversion time and CO_2 in the dry product gases. For the algae case a large reduction in CO_2 production is shown in the experimental results. Even though algae are a difficult compound to convert completely to dry product gases, the conversion doubles when NaOH is added to the process.

7.2 Recommendations

The thermodynamic system model shows that use of the heat present in the combustion flue gases is a good opportunity for further improvement of the thermal efficiency. Availability of the heat present in the combustion flue gases for preheating the water present in the feedstream should be investigated more thoroughly.

In order to design an economically feasible SCWG process a high efficient heat exchanger needs to be developed.

Each individual Nusselt correlation from literature shows an incapability to predict the heat transfer coefficient accurately over the entire pipe length. Therefore it is recommended to use a two dimensional or a three dimensional modeling approach to simulate the heat transfer to supercritical water in long or complex pipe configurations.

On basis of the two dimensional model results, heat transfer to the reacting flow has been found to be more effective than to the non-reacting flow. The considerable improvement of heat transfer is mainly due to the production of hydrogen in the hot boundary layer, which has a positive effect on the local thermal conductivity. The chemistry of biomass conversion should however be included in more detail for a more realistic simulation of the reacting flow.

The chemistry of supercritical gasification of both methanol and micro-algae remain poorly understood and need to be studied in more detail in the future. The high-throughput reactor developed in this research can be used as a fast screening tool for the understanding of each separate reaction step in the conversion of wet biomass within a supercritical gasifier.

Several sorbents are investigated for the process of sorbent enhanced supercritical gasification of wet biomass. For hydrotalcite and NaOH a decay in adsorption capacity as a function of the number of calcination-carbonation cycles is expected, similar to the decay in adsorption capacity of CaO. More research on the adsorption capacity and the chemical stability during carbonation/calcination cycles is needed for the used sorbents to qualify the optimal sorbent for sorption enhanced gasification of biomass in supercritical water.

Bibliography

[1] Aspen Plus 12.1 Manual.

[2] J.C. Abanades. The maximum capture efficiency of CO2 using a carbonation/ calcination cycle of CaO/CaCO3. *Chemical Engineering Journal*, 90(3):303–306, 2002.

[3] J.C. Abanades, E.S. Rubin, and E.J. Anthony. Sorbent cost and performance in CO2 capture systems. *Industrial & Engineering Chemistry Research*, 43(13):3462–3466, 2004.

[4] I.M. Abdulagatov, N.G. Polikhronidi, A. Abdurashidova, S.B. Kiselev, and J.F. Ely. Thermodynamic properties of methanol in the critical and supercritical regions. *International Journal of Thermophysics*, 26(5):1327–1368, 2005.

[5] T. Aicher and H. Martin. New correlations for mixed turbulent natural and forced convection heat transfer in vertical tubes. *International Journal of Heat and Mass Transfer*, 40(15):3617–3626, 1997.

[6] D. Alvarez and J.C. Abanades. Pore-size and shape effects on the recarbonation performance of calcium oxide submitted to repeated calcination/recarbonation cycles. *Energy & Fuels*, 19(1):270–278, 2005.

[7] M.J. Antal. Synthesis gas production from organic wastes by pyrolysis/steam reforming. *Energy from Biomass and Wastes*, pages 14–18, 1978.

[8] M.J. Antal, T. Leesomboon, W.S. Mok, and G.N. Richards. Mechanism of formation of 2-furaldehyde from D-xylose. *Carbohydrate Research*, 217:71–85, 1991.

[9] M.J. Antal, S. Manarungson, and W.S. Mok. Hydrogen Production by Steam Reforming Glucose in Supercritical Water. *A.V. Bridgwater. Advances in Thermochemical Biomass Conversion, London: Blackie Academic and Professional*, 1367, 1993.

[10] M.J. Antal, W.S.L. Mok, and G.N. Richards. Four-carbon model compounds for the reactions of sugars in water of high temperature. *Carbohydrate Research*, 199(1):111–115, 1990.

[11] M.J. Antal, W.S.L. Mok, and G.N. Richards. Kinetic studies of the reactions of ketoses and aldoses in water at high temperature. 1. Mechanism of formation of 5-(hydroxymethyl)-2-furaldehyde from d-fructose and sucrose. *Carbohydrate Research*, 199:91–109, 1990.

[12] M.J. Antal Jr, S.G. Allen, D. Schulman, X. Xu, and R.J. Divilio. Biomass gasification in supercritical water. *Industrial & Engineering Chemistry Research*, 39(11):4040–4053, 2000.

[13] M.J. Antal Jr, W.S.L. Mok, J.C. Roy, A.T. Raissi, and D.G.M. Anderson. Pyrolytic sources of hydrocarbons from biomass. *Journal of Analytical and Applied Pyrolysis*, 8:291–303, 1985.

[14] P. Atkins and J. De Paula. Atkins physical chemistry. *Chemistry*, 2006.

[15] A. Austegard, E. Solbraa, G. de Koeijer, and M. J. Molnvik. Thermodynamic models for calculating mutual solubilities in H2O-CO2-CH4 mixtures. *Chemical Engineering Research and Design*, 84:781–794, 2006.

[16] B. Balasubramanian, A. Lopez Ortiz, S. Kaytakoglu, and D.P. Harrison. Hydrogen from methane in a single-step process. *Chemical Engineering Science*, 54(15-16):3543–3552, 1999.

[17] L. Barelli, G. Bidini, F. Gallorini, and S. Servili. Hydrogen production through sorption-enhanced steam methane reforming and membrane technology: a review. *Energy*, 33(4):554–570, 2008.

[18] M.G. Beaver, H.S. Caram, and S. Sircar. Selection of CO2 chemisorbent for fuel-cell grade H2 production by sorption-enhanced water gas shift reaction. *International Journal of Hydrogen Energy*, 34(7):2972–2978, 2009.

[19] A. Belmiloudi. Heat Transfer - Theoretical Analysis, Experimental Investigations and Industrial Systems. 2011.

[20] A. Bhattacharyya, V.W. Chang, and D.J. Schumacher. CO2 reforming of methane to syngas I: evaluation of hydrotalcite clay-derived catalysts. *Applied Clay Science*, 13(5-6):317–328, 1998.

[21] R.B. Bird, W.E. Stewart, and E.N. Lightfoot. Transport Phenomena John Wiley & Sons. *New York*, 1960.

[22] N. Boukis, V. Diem, U. Galla, and E. Dinjus. Methanol reforming in supercritical water for hydrogen production. *Combustion Science and Technology*, 178(1):467–485, 2006.

[23] N. Boukis, V. Diem, W. Habicht, and E. Dinjus. Methanol Reforming in Supercritical Water. *Industrial & Engineering Chemistry Research*, 42(4):728–735, 2003.

[24] N. Boukis, U. Galla, H. Müller, and E. Dinjus. Biomass gasification in supercritical water. experimental progress achieved with the VERENA pilot plant. In *15th European Biomass Conference & Exhibition, Berlin*, 2007.

[25] S. Bretsznajder and J. Bandrowski. *Prediction of Transport and other physical properties of fluids.* Pergamon Press London, 1971.

[26] A.R. Brun-Tsekhovoi, A.N. Zadorin, Y.R. Katsobashvili, and S.S. Kourdyumov. The process of catalytic steam-reforming of hydrocarbons in the presence of carbon dioxide acceptor. In *Hydrocarbon Energy Progress VII, Proceedings of the 7th World Hydrogen Energy Conference Moscow, Sept. 1988*, volume 2, page 885. Pergamon Press: New York, 1988.

[27] G.P. Celata, F. Dannibale, A. Chiaradia, and M. Cumo. Upflow turbulent mixed convection heat transfer in vertical pipes. *International Journal of Heat and Mass Transfer*, 41(24):4037–4054, 1998.

[28] A.G. Chakinala, D.W.F. Brilman, W.P.M. van Swaaij, and S.R.A. Kersten. Catalytic and non-catalytic supercritical water gasification of microalgae and glycerol. *Industrial & Engineering Chemistry Research*, 49(3):1113–1122, 2009.

[29] X. Cheng, B. Kuang, and Y.H. Yang. Numerical analysis of heat transfer in supercritical water cooled flow channels. *Nuclear Engineering and Design*, 237(3):240–252, 2007.

[30] X. Cheng and T. Schulenberg. *Heat Transfer at Supercritical Pressures: Literature Review and Application to an HPLWR.* FZKA, 2001.

[31] S. Dahl, A. Dunalewicz, A. Fredenslund, and P. Rasmussen. The MHV2 model: Prediction of phase equilibria at sub-and supercritical conditions. *The Journal of Supercritical Fluids*, 5(1):42–47, 1992.

[32] V.K. Dhir. Boiling heat transfer. *Annual review of fluid mechanics*, 30(1):365–401, 1998.

[33] G.J. DiLeo and P.E. Savage. Catalysis during methanol gasification in supercritical water. *The Journal of Supercritical Fluids*, 39(2):228–232, 2006.

[34] Y. Ding and E. Alpay. Equilibria and kinetics of CO2 adsorption on hydrotalcite adsorbent. *Chemical Engineering Science*, 55(17):3461–3474, 2000.

[35] Y. Ding and E. Alpay. High temperature recovery of CO2 from flue gases using hydrotalcite adsorbent. *Process Safety and Environmental Protection*, 79(1):45–51, 2001.

[36] F.W. Dittus and L.M.K. Boelter. Heat transfer in automobile radiators of the tubular type. *International Communications in Heat and Mass Transfer*, 12(1):3–22, 1985.

[37] D.C. Elliott, G.G. Neuenschwander, T.R. Hart, R.S. Butner, W.P.M. Van Swaaij, et al. Low-temperature catalytic gasification of wet biomass residues. Technical report, Pacific Northwest National Laboratory (PNNL), Richland, WA (US), Environmental Molecular Sciences Laboratory (EMSL), 2004.

[38] D.C. Elliott, L.J.J. Sealock, and E.G. Baker. Chemical Processing in high-pressure aqueous environments. 3. Batch reactor process development experiments for organics destruction. *Industrial & Engineering Chemistry Research*, 33(3):558–565, 1994.

[39] D.C. Elliott and L.J. Sealock Jr. Aqueous catalyst systems for the water-gas shift reaction. 1. comparative catalyst studies. *Industrial & Engineering Chemistry Product Research and Development*, 22(3):426–431, 1983.

[40] D.C. Elliott, L.J. Sealock Jr, and E.G. Baker. Chemical processing in high-pressure aqueous environments. 2. development of catalysts for gasification. *Industrial & Engineering Chemistry Research*, 32(8):1542–1548, 1993.

[41] E. Fares and W. Schroder. A differential equation for approximate wall distance. *International Journal for Numerical Methods in Fluids*, 39(8):743–762, 2002.

[42] B. Ficicilar and T. Dogu. Breakthrough analysis for CO2 removal by activated hydrotalcite and soda ash. *Catalysis Today*, 115(1-4):274–278, 2006.

[43] I. Formulation. Revised release on the IAPS formulation 1985 for the thermal conductivity of ordinary water substance, september 1998. *The International Association for the Properties of Water and Steam, London, England*, 1998.

[44] W. Hack, D.A. Masten, and S.J. Buelow. Methanol and ethanol decomposition in supercritical water. *Zeitschrift fur Physikalische Chemie/International journal of research in physical chemistry and chemical physics*, 219(3/2005):367–378, 2005.

[45] C. Han and D.P. Harrison. Simultaneous shift reaction and carbon dioxide separation for the direct production of hydrogen. *Chemical Engineering Science*, 49(24):5875–5883, 1994.

[46] X.H. Hao, L.J. Guo, X. Mao, X.M. Zhang, and X.J. Chen. Hydrogen production from glucose used as a model compound of biomass gasified in supercritical water. *International Journal of Hydrogen Energy*, 28(1):55–64, 2003.

[47] D.P. Harrison and Z. Peng. Low-carbon monoxide hydrogen by sorption-enhanced reaction. *International Journal of Chemical Reactor Engineering*, 1(1):37, 2003.

[48] H.R. Holgate, J.C. Meyer, and J.W. Tester. Glucose hydrolysis and oxidation in supercritical water. *AIChE Journal*, 41(3):637–648, 1995.

[49] J.R. Hufton, S. Mayorga, and S. Sircar. Sorption-enhanced reaction process for hydrogen production. *AIChE Journal*, 45(2):248–256, 1999.

[50] F.P. Incropera and D.P. De Witt. *Fundamentals of heat and mass transfer*. John Wiley and Sons Inc., New York, NY, 1985.

[51] J.D. Jackson, M.A. Cotton, and B.P. Axcell. Studies of mixed convection in vertical tubes. *International journal of heat and fluid flow*, 10(1):2–15, 1989.

[52] J.D. Jackson and W.B. Hall. Forced convection heat transfer to fluids at supercritical pressure. *Turbulent forced convection in channels and bundles*, 2:563–612, 1979.

[53] J.D. Jackson and W.B. Hall. Influences of buoyancy on heat transfer to fluids flowing in vertical tubes under turbulent conditions. *Turbulent forced convection in channels and bundles*, 2:613–640, 1979.

[54] K. Johnsen, H.J. Ryu, J.R. Grace, and C.J. Lim. Sorption-enhanced steam reforming of methane in a fluidized bed reactor with dolomite as CO2-acceptor. *Chemical engineering science*, 61(4):1195–1202, 2006.

[55] Y. Kalinci, A. Hepbasli, and I. Dincer. Biomass-based hydrogen production: a review and analysis. *International Journal of Hydrogen Energy*, 34(21):8799–8817, 2009.

[56] W.M. Kays. Turbulent prandtl number. where are we? *ASME Transactions Journal of Heat Transfer*, 116:284–295, 1994.

[57] R.J. Kee, M.E. Coltrin, and P. Glarborg. *Chemically reacting flow: theory and practice*. Wiley-Interscience, 2003.

[58] S.R.A. Kersten, B. Potic, W. Prins, and W.P.M. Van Swaaij. Gasification of model compounds and wood in hot compressed water. *Industrial & Engineering Chemistry Research*, 45(12):4169–4177, 2006.

[59] A. Kruse. Supercritical water gasification. *Biofuels, Bioproducts and Biorefining*, 2(5):415–437, 2008.

[60] A. Kruse. Hydrothermal biomass gasification. *The Journal of Supercritical Fluids*, 47(3):391–399, 2009.

[61] A. Kruse, J. Abeln, E. Dinjus, M. Kluth, G. Petrich, M. Schacht, H. Sadri, and H. Schmieder. Gasification of biomass and model compounds in hot compressed water. In *International Meeting of the GVC-Fachausschuß " Hochdruckverfahrenstechnik", Karlsruhe, Germany*, 1999.

[62] A. Kruse and E. Dinjus. Influence of salts during hydrothermal biomass gasification: The role of the catalysed water-gas shift reaction. *Zeitschrift für Physikalische Chemie/International journal of research in physical chemistry and chemical physics*, 219(3/2005):341–366, 2005.

[63] A. Kruse, D. Forchheim, M. Gloede, F. Ottinger, and J. Zimmermann. Brines in supercritical biomass gasification: 1. salt extraction by salts and the influence on glucose conversion. *The Journal of Supercritical Fluids*, 53(1-3):64–71, 2010.

[64] A. Kruse and A. Gawlik. Biomass Conversion in Water at 330- 410 degC and 30- 50 MPa. Identification of Key Compounds for Indicating Different Chemical Reaction Pathways. *Industrial & Engineering Chemistry Research*, 42(2):267–279, 2003.

[65] A. Kruse, T. Henningsen, A. Sinag, and J. Pfeiffer. Biomass gasification in supercritical water: Influence of the dry matter content and the formation of phenols. *Industrial & Engineering Chemistry Research*, 42(16):3711–3717, 2003.

[66] A. Kruse, D. Meier, P. Rimbrecht, and M. Schacht. Gasification of Pyrocatechol in Supercritical Water in the Presence of Potassium Hydroxide. *Industrial & Engineering Chemistry Research*, 39(12):4842–4848, 2000.

[67] B.G. Kyle. *Chemical and process thermodynamics*. Prentice-Hall, Inc., Englewood Cliffs, NJ, 1984.

[68] I.G. Lee, M.S. Kim, and S.K. Ihm. Gasification of glucose in supercritical water. *Industrial & Engineering Chemistry Research*, 41(5):1182–1188, 2002.

[69] K.B. Lee, M.G. Beaver, H.S. Caram, and S. Sircar. Production of fuel-cell grade hydrogen by thermal swing sorption enhanced reaction concept. *International Journal of Hydrogen Energy*, 33(2):781–790, 2008.

[70] K.B. Lee, A. Verdooren, H.S. Caram, and S. Sircar. Chemisorption of carbon dioxide on potassium-carbonate-promoted hydrotalcite. *Journal of Colloid and Interface Science*, 308(1):30–39, 2007.

[71] J. Li, I. Vanderbeken, S. Ye, H. Carrier, and P. Xans. Prediction of the solubility and gas-liquid equilibria for gas-water and light hydrocarbon-water systems at high temperatures and pressures with a group contribution equation of state. *Fluid Phase Equilibria*, 131(1):107–118, 1997.

[72] J. Licht, M. Anderson, and M. Corradini. Heat transfer to water at supercritical pressures in a circular and square annular flow geometry. *International Journal of Heat and Fluid Flow*, 29(1):156–166, 2008.

[73] D.R. Lide and H.P.R. Frederikse. *CRC Handbook of Chemistry and Physics*. CRC Press Inc., 76th edition, 1995. NIST Chemistry WebBook.

[74] P.J. Linstrom and W.G. Mallard. *NIST Chemistry WebBook*. National Institute of Standards and Technology Gaithersburg, MD, 1997.

[75] Y. Lu, L. Guo, X. Zhang, and Q. Yan. Thermodynamic modeling and analysis of biomass gasification for hydrogen production in supercritical water. *Chemical Engineering Journal*, 131(1):233–244, 2007.

[76] Y. Lu, L. Guo, X. Zhang, and Q. Yan. Thermodynamic modeling and analysis of biomass gasification for hydrogen production in supercritical water. *Chemical Engineering Journal*, 131(1-3):233–244, 2007.

[77] A.E. Lutz, R.W. Bradshaw, J.O. Keller, and D.E. Witmer. Thermodynamic analysis of hydrogen production by steam reforming. *International Journal of Hydrogen Energy*, 28(2):159–167, 2003.

[78] G. Marban and T. Valdés-Solís. Towards the hydrogen economy? *International Journal of Hydrogen Energy*, 32(12):1625–1637, 2007.

[79] Y. Matsumura, M. Harada, K. Nagata, and Y. Kikuchi. Effect of heating rate of biomass feedstock on carbon gasification efficiency in supercritical water gasification. *Chemical Engineering Communications*, 193(5):649–659, 2006.

[80] Y. Matsumura, T. Minowa, B. Potic, S.R.A. Kersten, W. Prins, W.P.M. van Swaaij, B. van de Beld, D.C. Elliott, G.G. Neuenschwander, A. Kruse, et al. Biomass

gasification in near-and super-critical water: status and prospects. *Biomass and Bioenergy*, 29(4):269–292, 2005.

[81] M. Modell. Gasification and liquefaction of forest products in supercritical water. *Fundamentals of Thermochemical Biomass Conversion*, pages 95–119, 1985.

[82] W.S.L. Mok, M.J. Antal Jr, and M. Jones Jr. Formation of acrylic acid from lactic acid in supercritical water. *The Journal of Organic Chemistry*, 54(19):4596–4602, 1989.

[83] S. Mokry, I. Pioro, A. Farah, K. King, S. Gupta, W. Peiman, and P. Kirillov. Development of supercritical water heat-transfer correlation for vertical bare tubes. *Nuclear Engineering and Design*, 2010.

[84] S. Mokry, I. Pioro, A. Farah, K. King, S. Gupta, W. Peiman, and P. Kirillov. Development of supercritical water heat-transfer correlation for vertical bare tubes. *Nuclear Engineering and Design*, 241(4):1126–1136, 2011.

[85] M. Mozaffarian, R.W.R. Zwart, H. Boerrigter, E.P. Deurwaarder, and S.R.A. Kersten. Green gas as sng (synthetic natural gas); a renewable fuel with conventional quality. In *Science in Thermal and Chemical Biomass Conversion, 6th International Conference, Vancouver Island, Canada*, volume 30, 2004.

[86] R. Narayan and M.J. Antal. Kinetic elucidation of the acid-catalyzed mechanism of 1-propanol dehydration in supercritical water. In *ACS Symposium Series*, volume 406, pages 226–241. ACS Publications, 1989.

[87] R. Narayan and M.J. Antal Jr. Influence of pressure on the acid-catalyzed rate constant for 1-propanol dehydration in supercritical water. *Journal of the American Chemical Society*, 112(5):1927–1931, 1990.

[88] E. Neau, O. Hernández-Garduza, J. Escandell, C. Nicolas, and I. Raspo. The Soave, Twu and Boston-Mathias alpha functions in cubic equations of state: Part I. Theoretical analysis of their variations according to temperature. *Fluid Phase Equilibria*, 276(2):87–93, 2009.

[89] H. Ogata and S. Sato. Measurements of forced convection heat transfer to supercritical helium. In *Fourth International Cryogenic Engineering Conference, Eindhoven, Netherlands*, 1972.

[90] E.L.G. Oliveira, C.A. Grande, and A.E. Rodrigues. CO2 sorption on hydrotalcite and alkali-modified (K and Cs) hydrotalcites at high temperatures. *Separation and Purification Technology*, 62(1):137–147, 2008.

[91] A.L. Ortiz and D.P. Harrison. Hydrogen production using sorption-enhanced reaction. *Industrial & Engineering Chemistry Research*, 40(23):5102–5109, 2001.

[92] D.Y. Peng and D.B. Robinson. A new two-constant equation of state. *Industrial & Engineering Chemistry Fundamentals*, 15(1):59–64, 1976.

[93] B.S. Petukhov, V.A. Kurganov, and V.B. Ankudinov. Heat transfer and flow resistance in the turbulent pipe flow of a fluid with near-critical state parameters. *Teplofizika Vysokikh Temperatur*, 21:92–100, 1983.

[94] B. Potic. *Gasification of biomass in supercritical water*. PhD thesis, University of Twente, 2006.

[95] S. Ramayya, A. Brittain, C. DeAlmeida, W. Mok, and M.J. Antal Jr. Acid-catalysed dehydration of alcohols in supercritical water. *Fuel*, 66(10):1364–1371, 1987.

[96] M.K.R. Reddy, Z.P. Xu, G.Q. Lu, , and J.C.D. Da Costa. Influence of water on high-temperature CO2 capture using layered double hydroxide derivatives. *Industrial & Engineering Chemistry Research*, 47(8):2630–2635, 2008.

[97] O. Redlich and J.N.S. Kwong. On the Thermodynamics of Solutions. V. An Equation of State. Fugacities of Gaseous Solutions. *Chemical Reviews*, 44(1):233–244, 1949.

[98] R.C. Reid, J.M. Prausnitz, and B.E. Poling. *The properties of gases and liquids*. McGraw Hill Book Co., New York, NY, 1987.

[99] J.L.H.P. Sallevelt, J.A.M. Withag, E.A. Bramer, D.W.F. Brilman, and G. Brem. One-dimensional model for heat transfer to a supercritical water flow in a tube. *The Journal of Supercritical Fluids*, 68:1–12, 2012.

[100] H. Schmieder, J. Abeln, N. Boukis, E. Dinjus, A. Kruse, M. Kluth, G. Petrich, E. Sadri, and M. Schacht. Hydrothermal gasification of biomass and organic wastes. *The Journal of Supercritical Fluids*, 17(2):145–153, 2000.

[101] I. Secretariat and B. Dooley. Revised release on the IAPS formulation 1985 for the thermal conductivity of ordinary water substance. 1997.

[102] A. Silaban and D.P. Harrison. High temperature capture of carbon dioxide: characteristics of the reversible reaction between CaO (s) and CO2 (g). *Chemical Engineering Communications*, 137(1):177–190, 1995.

[103] A. Sinag, A. Kruse, and V. Schwarzkopf. Key compounds of the hydropyrolysis of glucose in supercritical water in the presence of K2CO3. *Industrial & Engineering Chemistry Research*, 42(15):3516–3521, 2003.

[104] R.K. Sinnott and G. Towler. *Chemical Engineering Design: SI edition*, volume 3. Butterworth-Heinemann, 2009.

[105] G. Soave, M. Barolo, and A. Bertucco. Estimation of high-pressure fugacity coefficients of pure gaseous fluids by a modified SRK equation of state. *Fluid Phase Equilibria*, 91(1):87–100, 1993.

[106] R.F. Susanti, L.W. Dianningrum, T. Yum, Y. Kim, B.G. Lee, and J. Kim. High-yield hydrogen production from glucose by supercritical water gasification without added catalyst. *International Journal of Hydrogen Energy*, 2012.

[107] H.S. Swenson, J.R. Carver, and C.R. Kakarala. Heat transfer to supercritical water in smooth-bore tubes. *Journal of Heat Transfer*, 87(4):477–484, 1965.

[108] H. Tanaka, S. Hatano, and S. Maruyama. Combined forced and natural convection heat transfer for upward flow in a uniformly heated vertical pipe: Series b: Fluids engineering, heat transfer, combustion, power, thermophysical properties. *JSME international journal: bulletin of the JSME*, 30(266):1348, 1987.

[109] H. Tang and K. Kitagawa. Supercritical water gasification of biomass: thermodynamic analysis with direct Gibbs free energy minimization. *Chemical Engineering Journal*, 106(3):261–267, 2005.

[110] J.D. Taylor, C.M. Herdman, B.C. Wu, K. Wally, and S.F. Rice. Hydrogen production in a compact supercritical water reformer. *International Journal of Hydrogen Energy*, 28(11):1171–1178, 2003.

[111] J.O. Valderrama. The state of the cubic equations of state. *Industrial & Engineering Chemistry Research*, 42(8):1603–1618, 2003.

[112] L. Van de Beld, B.M. Wagenaar, D. Assink, B. Potic, S.R.A. Kersten, W. Prins, W.P.M. van Swaaij, and J.M.L. Penninger. Biomass and waste conversion in supercritical water for the production of renewable hydrogen. In *1st European Hydrogen Energy Conference, Grenoble, France*, 2003.

[113] G. Varhegyi, P. Szabo, W.S.L. Mok, and M.J. Antal. Kinetics of the thermal decomposition of cellulose in sealed vessels at elevated pressures. effects of the presence of water on the reaction mechanism. *Journal of Analytical and Applied Pyrolysis*, 26(3):159–174, 1993.

[114] D.S. Viswanath. *Viscosity of liquids: theory, estimation, experiment, and data.* Springer Verlag, 2007.

[115] W. Wagner, J.R. Cooper, A. Dittmann, J. Kijima, H.J. Kretzschmar, A. Kruse, R. Mareš, K. Oguchi, H. Sato, I. Stocker, et al. The IAPWS industrial formulation

1997 for the thermodynamic properties of water and steam. *Journal of Engineering for Gas Turbines and Power*, 122:150, 2000.

[116] W. Wagner and H.J. Kretzschmar. *International steam tables: properties of water and steam based on the industrial formulation IAPWS-IF97: tables, algorithms, diagrams, and CD-ROM electronic steam tables: all of the equations of IAPWS-IF97 including a complete set of supplementary backward equations for fast calculations of heat cycles, boilers, and steam turbines.* Springer Verlag, 2008.

[117] W. Wagner and A. Kruse. *Properties of Water and Steam: The Industrial Standard IAPWS-IF97 for the Thermodynamic Properties and Supplementary Equations for Other Properties: Tables Based on These Equations.* Springer Verlag, 1998.

[118] W. Wagner and A. Pruss. The IAPWS formulation 1995 for the thermodynamic properties of ordinary water substance for general and scientific use. *Journal of Physical and Chemical Reference Data*, 31(2):387, 1999.

[119] S. Walspurger, L. Boels, P.D. Cobden, G.D. Elzinga, W.G. Haije, and R.W. Van Den Brink. The crucial role of the K+–aluminium oxide interaction in K+-promoted alumina-and hydrotalcite-based materials for CO2 sorption at high temperatures. *ChemSusChem*, 1(7):643–650, 2008.

[120] J. Warnatz, U. Maas, and R.W. Dibble. *Verbrennung.* Springer Berlin, 2001.

[121] M. Watanabe, H. Inomata, and K. Arai. Catalytic hydrogen generation from biomass (glucose and cellulose) with ZrO2 in supercritical water. *Biomass and Bioenergy*, 22(5):405–410, 2002.

[122] M. Watanabe, H. Inomata, M. Osada, T. Sato, T. Adschiri, and K. Arai. Catalytic effects of NaOH and ZrO2 for partial oxidative gasification of n-hexadecane and lignin in supercritical water. *Fuel*, 82(5):545–552, 2003.

[123] M. Watanabe, T. Sato, H. Inomata, R.L.J. Smith, K. Arai, A. Kruse, and E. Dinjus. Chemical reactions of C1 compounds in near-critical and supercritical water. *Chemical Reviews*, 104:5803–5821, 2004.

[124] H. Weingärtner and E.U. Franck. Supercritical water as a solvent. *Angewandte Chemie International Edition*, 44(18):2672–2692, 2005.

[125] D.C. Wilcox. *Turbulence modeling for CFD.* 1993.

[126] J.A.M. Withag, J.L.H.P. Sallevelt, D.W.F. Brilman, E.A. Bramer, and G. Brem. Heat transfer characteristics of supercritical water in a tube. application for 2D and an experimental validation. *The Journal of Supercritical Fluids*, 70:156–170, 2012.

[127] J.A.M. Withag, J.R. Smeets, E.A. Bramer, and G. Brem. System model for gasification of biomass model compounds in supercritical water-a thermodynamic analysis. *The Journal of Supercritical Fluids*, 61:157–166, 2012.

[128] H.W. Xiang, A. Laesecke, and M.L. Huber. A new reference correlation for the viscosity of methanol. *Journal of Physical and Chemical Reference Data*, 35(4):1597–1620, 2006.

[129] M. Xie, Z. Zhou, Y. Qi, Z. Cheng, and W. Yuan. Sorption-enhanced steam methane reforming by in situ CO2 capture on a CaO-Ca9Al6O18 sorbent. *Chemical Engineering Journal*, 2012.

[130] X. Xu and M.J. Antal Jr. Kinetics and mechanism of isobutene formation from T-butanol in hot liquid water. *AIChE Journal*, 40(9):1524–1534, 1994.

[131] X. Xu, C.P. De Almeida, and M.J. Antal Jr. Mechanism and kinetics of the acid-catalyzed formation of ethene and diethyl ether from ethanol in supercritical water. *Industrial & Engineering Chemistry Research*, 30(7):1478–1485, 1991.

[132] X. Xu, Y. Matsumura, J. Stenberg, and M.J. Antal Jr. Carbon-catalyzed gasification of organic feedstocks in supercritical water. *Industrial & Engineering Chemistry Research*, 35(8):2522, 1996.

[133] K. Yamagata, K. Nishikawa, S. Hasegawa, T. Fujii, and S. Yoshida. Forced convective heat transfer to supercritical water flowing in tubes. *International Journal of Heat and Mass Transfer*, 15(12):2575–2593, 1972.

[134] Q. Yan, L. Guo, and Y. Lu. Thermodynamic analysis of hydrogen production from biomass gasification in supercritical water. *Energy Conversion and Management*, 47(11-12):1515–1528, 2006.

[135] T.W. Yergovich, G.W. Swift, and F. Kurata. Density and viscosity of aqueous solutions of methanol and acetone from the freezing point to 10 degC. *Journal of Chemical & Engineering Data*, 16(2):222–226, 1971.

[136] T. Yoshida and Y. Matsumura. Gasification of cellulose, xylan, and lignin mixtures in supercritical water. *Industrial & Engineering Chemistry Research*, 40(23):5469–5474, 2001.

[137] T. Yoshida, Y. Oshima, and Y. Matsumura. Gasification of biomass model compounds and real biomass in supercritical water. *Biomass and Bioenergy*, 26(1):71–78, 2004.

[138] D. Yu, M. Aihara, and M.J. Antal Jr. Hydrogen production by steam reforming glucose in supercritical water. *Energy & Fuels*, 7(5):574–577, 1993.

[139] J. Yu, B. Jia, D. Wu, and D. Wang. Optimization of heat transfer coefficient correlation at supercritical pressure using genetic algorithms. *Heat and mass transfer*, 45(6):757–766, 2009.

Nomenclature

Roman

a_{ij}	Molar number of element i in compound j [-]
b_i^0	Initial number of element i in the initial reactant [-]
C_p	Specific isobaric heat capacity [J/kgK]
$C_{\epsilon 1}$	Constant, $C_{\epsilon 1} = 1.5$, in the Low Reynolds $k - \epsilon$ model [-]
$C_{\epsilon 2}$	Constant, $C_{\epsilon 2} = 1.9$, in the Low Reynolds $k - \epsilon$ model [-]
C_μ	Constant, $C_\mu = 0.09$, in the Low Reynolds $k - \epsilon$ model [-]
D	Tube diameter [m]
D_{im}	Diffusion coefficient for diffusion of species i into a mixture of other species [m^2/s]
$\vec{d_i}$	Diffusion driving forces [1/m]
E	Total energy [m^2/s^2]
E_a	Activation energy [kJ/mol]
$\vec{f}$	Volume forces [m/s^2]
f_i	Partial fugacity of component i [bar]
G	Mass velocity [kg/m^2s]
$\Delta_r G$	Gibbs energy of reaction [J]
g	Acceleration due to gravity [m/s^2]
H	Enthalpy [J]
ΔH_r	Heat of reaction at constant pressure [J]

h	Heat transfer coefficient [W/m^{2}K]
h	Specific enthalpy [J/kg]
$\vec{j}_i$	Diffusive mass flux vector [kg/m^{2}s]
K_w	Ionic dissociation constant [(mol/kg)^2]
L	Tube length [m]
k	Thermal conductivity [W/mK]
k	Turbulence kinetic energy [m^2/s^2]
k_H	Henry's coefficient [mole/kg $\cdot$ bar]
k_H^0	Henry's coefficient at atmospheric temperature [mole/kg $\cdot$ bar]
k_n	Homogeneous reaction velocity constant, for nth order: [m$^{3(n-1)}$/kmol^{n-1} $\cdot$ s]
$k_{b,j}$	Backward reaction rate constant for reaction j [mol/s]
$k_{f,j}$	Forward reaction rate constant for reaction j [mol/s]
l_w	Distance closest to the wall [m]
M_i	Molecular weight of species i [kg/mol]
N	Number of moles
n_j	Molar number of component j [-]
P_c	Critical pressure [bar]
p	Pressure [bar]
$\dot{Q}$	Volumetric heat source [W]
$\vec{q}$	Heat flux vector [W/m^2]
R	Specific gas constant of mixture [J/kg $\cdot$ K]
r_i	Chemical source term [kg/m^{3}s]
T	Temperature [K]
T_c	Critical temperature [K]
t	Time [s]
$\vec{u}$	Velocity vector [m/s]
x_i	Mole fraction of species i [-]

X_c	Specific gas constant of mixture [J/kgK]
y_i	Mass fraction of species i [-]
z	Axial coordinate [m]

Greek

α	Thermal diffusivity [$\mathrm{m^2/s}$]
β	Coefficient of volume expansion [1/K]
$\vec{\vec{\delta}}$	Unity vector [-]
ϵ	Dielectric constant [-]
ϵ	Rate of dissipation of k [$\mathrm{m^2/s^3}$]
η_{th}	Thermal efficiency [-]
κ	Dilatational viscosity [kg/m·s]
Λ	Wall distance parameter [1/m]
μ	Dynamic viscosity [kg/ms]
μ_j	chemical potential of component j [J/mol]
ν	Kinematic viscosity [$\mathrm{m^2/s}$]
ν'_{ij}	Stoichiometric coefficient of forward reaction [-]
ν''_{ij}	Stoichiometric coefficient of backward reaction [-]
ξ	Extent of reaction [-]
ξ	Friction factor [-]
ρ	Density [$\mathrm{kg/m^3}$]
σ_ϵ	Constant, $\sigma_\epsilon = 1.5$, in the Low Reynolds $k - \epsilon$ model [-]
σ_k	Constant, $\sigma_k = 1.4$, in the Low Reynolds $k - \epsilon$ model [-]
$\vec{\vec{\tau}}$	Viscous stress tensor [$\mathrm{kg/m \cdot s^2}$]

Mathematical

$\bar{x}$	Reynolds average of a quantity x
$\cdot$	Inner product
$\frac{\partial}{\partial t}$	Partial derivative

$\sum$	Summation
$\tilde{x}$	Favre average of a quantity x
$\vec{\nabla}$	Gradient operator
$\vec{\vec{A}}^T$	Transpose of vector or matrix $\vec{\vec{A}}$
x''	Fluctuation corresponding to Favre average of x

Subscripts

0	Refers to inlet conditions
∞	Refers to the fully developed condition
GC	Gas chromatograph
HPLC	High pressure liquid chromatography
aid	aiding
b	Refers to fluid bulk conditions
for	forced
lam	laminar
mix	mixed
nat	natural
opp	opposing
tur	turbulent
w	Refers to conditions at the tube wall

Dimensionless groups

Bo	Buoyancy parameter
Br	Brinkman number
Fr	Froude number
Gr	Grashof number based on temperature
Gr_q	Grashof number based on heat flux
Gz	Graetz number
Nu	Nusselt number

Pe	Peclet number
Pr	Prandtl number
Ra	Rayleigh number
Re	Reynolds number
St	Stanton number

Abbreviations

BM	Boston Mathias α function
BPR	Back pressure regulator
BSL	Baseline
CFD	Computational fluid dynamics
EOS	Equation of state
IAPWS	International association for the properties of water and steam
LHV	Lower heating value
MHV2	Modified Huron Vidal mixing rule
PFR	Plug flow reactor
RANS	Reynolds averaged navier stokes
SCWG	Supercritical water gasification
SST	Shear stress transport
WS	Wong Sandler mixing rule

List of publications

J.A.M. Withag, J.L.H.P. Sallevelt, D.W.F. Brilman, E.A. Bramer and G. Brem, Heat transfer characteristics of supercritical water in a tube: Application for 2D and an experimental validation, Elsevier **70** *(2012)*.

J.L.H.P. Sallevelt, J.A.M. Withag, E.A. Bramer, D.W.F. Brilman and G. Brem, One-dimensional model for heat transfer to a supercritical water flow in a tube, The Journal of Supercritical Fluids, Elsevier **68** *(2012)*.

J.A.M. Withag, J.R. Smeets, E.A. Bramer and G. Brem, System model for gasification of biomass model compounds in supercritical water - A thermodynamic analysis, The Journal of Supercritical Fluids, Elsevier **61** *(2012)*.

L. Xu, D.W.F. Brilman, J.A.M. Withag, G. Brem and S. Kersten, Assessment of a dry and a wet route for the production of biofuels from microalgae: Energy balance analysis, Bioresource technology, Elsevier **102** *(2011)*.

J.A.M. Withag, N.M. Vollenbroek, E.A. Bramer and G. Brem, Novel kinetic measurement technique for supercritical gasification of algae, Proceedings of the Bioten Conference on Biomass Bioenergy and Biofuels 2010 Edited by A V Bridgwater CPL Press, isbn nr: 978-1-872691-54-1, pp.759-766, October 2011.

J.A.M. Withag, E.A. Bramer and G. Brem, Novel Kinetic Measurement Technique for Supercritical Gasification of Solid Biomass, 17th European Biomass Conference 2009, Hamburg.

J.A.M. Withag, J.B.W. Kok, K. Syed, Transient Combustion Modeling of an oscillating lean premixed methane/air flame, GT2008-51125, ASME turbo expo 2008, Berlin.